

UC Irvine

UC Irvine Electronic Theses and Dissertations

Title

Understanding the Nucleation and Growth of ZIF-8 Polymorphs

Permalink

<https://escholarship.org/uc/item/980547jm>

Author

Talosig, Angelica Rain

Publication Date

2024

Peer reviewed|Thesis/dissertation

UNIVERSITY OF CALIFORNIA,
IRVINE

Understanding the Nucleation and Growth of ZIF-8 Polymorphs

DISSERTATION

Submitted in partial satisfaction of the requirements
for the degree of

DOCTOR OF PHILOSOPHY

in Chemistry

by

A. Rain Talosig

Dissertation Committee:
Assistant Professor Joseph Patterson, Chair
Assistant Professor Maxx Arguilla
Professor Andy S. Borovik

2024

Chapter 1 © 2021 American Chemical Society
Chapter 1 © 2023 Royal Society of Chemistry
Chapter 2 © 2024 American Chemical Society
Chapter 5 © 2022 Royal Society of Chemistry
All other materials © A. Rain Talosig

DEDICATION

This dissertation is dedicated to my parents, Reenah, Joe, and George
and to my siblings Isa, Gavin, Keoki, and Kalina

Thank you for all your love and support.

I couldn't have dreamed of this without your sacrifices.

I love you to Pluto and back.

Mahal Kita.

TABLE OF CONTENTS

	Page
List of Figures	vi
List of Tables	x
Acknowledgments	xi
Curriculum Vitae	xiii
Abstract of the Dissertation	xviii
Chapter 1: Introduction	1
1.1 Introduction.....	2
1.2 Nucleation and Growth Theories and Models.....	3
1.3 Polymorphism in MOFs.....	8
1.4 Controlling MOF Nucleation and Growth.....	10
1.5 Monitoring Nucleation and Growth.....	15
1.6 Dissertation Overview.....	18
1.7 References.....	20
Chapter 2: Polymorph Control in Metal-Organic Frameworks	26
2.1 Introduction.....	27
2.2 Results.....	29
2.3 Discussion.....	38
2.4 Conclusion.....	38
2.5 Methods.....	39
2.6 Acknowledgements.....	42
2.7 References.....	42
Appendix A: Supplementary Information for Chapter 2	45
A.1 ESI-MS Analysis.....	46
A.2 WAXS analysis of ZIF-8.....	47

A.3 ESI-MS Cluster Analysis.....	49
A.4 Crystal Size Analysis.....	51
A.5 References.....	51
Chapter 3: Confinement Effects on the Nucleation and Growth of ZIF-8.....	53
3.1 Introduction.....	54
3.2 Results and Discussion.....	56
3.3 Conclusion.....	61
3.4 Methods.....	62
3.5 Acknowledgements.....	64
3.6 References.....	64
Appendix B: Supplementary Information for Chapter 3.....	66
B.1 WAXS Analysis.....	67
B.2 Crystal Size Analysis.....	69
Chapter 4: Supramolecular Modification	70
4.1 Introduction.....	71
4.2 Results.....	74
4.3 Discussion.....	77
4.4 Conclusion.....	78
4.5 Methods.....	79
4.6 Acknowledgements.....	81
4.7 References.....	81
Chapter 5: Cyclodextrin Metal-Organic Framework-Based Protein Biocomposites.....	84
5.1 Introduction.....	85
5.2 Results and Discussion	86
5.3 Conclusion.....	91
5.4 Methods.....	92
5.5 Acknowledgements.....	96
5.6 References.....	96

Appendix C: Supplementary Information for Chapter 5	101
C.1 Encapsulation Efficiency.....	102
C.2 Structural Characterization.....	102
Chapter 6: Risk Assessment in Chemical Laboratories	104
6.1 Introduction.....	105
6.2 RAMP	106
6.3 Mental Health and Lab Safety	112
6.4 Safety Accessibility.....	118
6.5 Conclusions.....	118
Chapter 7: Conclusions	120
7.1 Outlook and Future Directions.....	121

LIST OF FIGURES

- Figure 1.1** Metal-organic framework general reaction scheme.
- Figure 1.2** Free energy diagram comparing monomer addition (classical nucleation theory) and nucleation through metastable phase (nonclassical nucleation theory) mechanisms.
- Figure 1.3** Summary of experiential and computational techniques used to study nucleation and growth of MOFs and of the phase regime that they are useful for probing.
- Figure 1.4** Summary of experiential and computational techniques used to study nucleation and growth of MOFs and of the phase regime that they are useful for probing.
- Figure 2.1** SEM of ZIF-8 (a) 4:1 (b) 17.5:1 (c) 35:1 (all scale bars are 2 μm) and (d) PXRD of ZIF-8 at HmIm:Zn ratios of 4:1, 17.5:1, 35:1 and simulated patterns for SOD and dia
- Figure 2.2** (a) Plot of the normalized area under 2θ 7-7.5 versus time produced by the integrated intensity of the (211) reflections collected by time-resolved in situ XRD. Time-resolved wide-angle x-ray scattering patterns of ZIF-8 (b) 4:1 and (c) 35:1 for the first 250 min. Background subtraction was performed for c) using an in-house MATLAB script, see SI for details.
- Figure 2.3** (a) ESI source where a dilute solution of ZIF-8 is injected, electrosprayed, and projected toward the MS inlet, yielding relative abundance versus mass/charge. Automated peak analysis shows the intensity of n Zn oligomers with size $n = 1-4$ (b) Zn fragmentation patterns of n Zn oligomers with size $n = 1-4$.
- Figure 2.4** Stacked ESI-MS plots of ZIF-8 at times 1min, 1H, 4H, 8H, 12H at Zn: HmIm ratio of (a) 4:1 (b) 17.5:1 (c)35:1. Sum of peaks of Zn oligomer size for Zn:HmIm ratios of (d) 4:1 (e) 17.5:1 (f)35:1.
- Figure 2.5** Representative Cryo-TEM images of nucleation and growth at 1 h of ZIF-8 in water. Scale bars are 100 nm. ZIF-8 with precursor ratios of (a) 4:1 (b) 17.5:1
- Figure A1** Simulated data for Zn isotope patterns for 1-4Zn species. Isotope patterns were used with in-house MATLAB script to determine the presence of Zn species.
- Figure A2** WAXS of 4:1 ZIF-8 collected after 12 hours in solution
- Figure A3** WAXS of 35:1 ZIF-8 collected after 12 hours in solution.
- Figure A4** Background subtraction performed on time resolved WAXS data of ZIF-8 35:1 (Figure 4c). a) Raw data. b) Background estimation was performed by applying 2

sequential, orthogonal 1D Gaussian blurs to the 2D raw data. The first 1D Gaussian filter was applied to the q domain, with a first standard deviation of 5 datapoints (0.012 1/\AA). The second 1D Gaussian filter was applied to the time domain, with a first standard deviation of 0.5 datapoints (2.5 seconds). The resulting 2D background is displayed above. c) Background subtraction was performed by dividing the raw data by the background estimation.

- Figure A5** PXRD of ZIF-8 at HmIm:Zn ratios of 10:1, 12:1, 15:1, 20:1 and simulated patterns for SOD and dia
- Figure A6** Crystal structures of ZIF-8 as (a) secondary building unit of one Zn tetrahedrally coordinated to four HmIm linkers (b) porous ZIF-8 SOD structure and (c) ZIF-8 dia. (d) Structures of 1-4 Zn clusters for SOD and dia. Crystal Structures of ZIF-8 SOD and dia were obtained from previously solved structures¹ and atoms were removed until appropriate sizes of the molecular clusters were reached based on the amount of Zn present.
- Figure A7** SEM image (scale bar $10 \mu\text{m}$) of ZIF-8 at 35:1 (HmIm:Zn) at $t = 24\text{h}$. Numbered yellow lines indicate the diameter of the crystal measured using Fiji, ImageJ.
- Figure 3.1** Summary of reaction volumes and container sizes with surface area to volume calculations.
- Figure 3.2** WAXS of ZIF-8 35:1. (a) Integration under the first crystalline peaks ($q = 0.5\text{-}0.53 \text{ 1/\AA}$) after 4 hours of reaction in a 1mm glass capillary and 15mm vial. SEM was collected after 4 hours of reaction in (b) 1mm glass capillary and (c) 15mm vial.
- Figure 3.3** Integration under the first 3 crystalline peaks ($q = 0.49\text{-}0.55$ and $0.68\text{-}0.80 \text{ 1/\AA}$) of ZIF-8 with Hmim:Zn ratios of (a) 17.5:1 and (b) 35:1 in special glass capillaries of 1mm and 2mm. WAXS was collected with a scan time of 10 min over 30 min intervals.
- Figure 3.4** SEM ZIF-8 with Hmim:Zn ratio of 17.5 with reaction in (a-c) 1mm capillaries and (d-f) 2mm capillaries at reaction times of 1,3 and 4 hours. SEM of 35:1 (g-i) 1mm capillaries and (j-l) 2mm capillaries at reaction times of 1,2 and 3 hours.
- Figure B1** Time-resolved WAXS of 35:1 ZIF-8 over 310 min with scans every 30 min.
- Figure B2** WAXS analysis (a) time-resolved WAXS of 35:1 ZIF-8 over 310 min with scans every 30 min (b) normalized WAXS 35:1 ZIF-8 (c) normalized area of peak with $q = 0.27\text{-}0.29 \text{ 1/\AA}$ (d) peak analysis table showing the scaling and the peak area and normalized peak area (e) sum of normalized peak area.

- Figure B3** SEM image (scale bar 10 μm) of ZIF-8 at 35:1 (HmIm:Zn) after 3 hours of reaction in 1 mm capillary. Numbered yellow lines indicate the diameter of the crystal measured using Fiji, ImageJ.
- Figure 4.1** Fluorescence intensity and zeta potential of CD:BSA complex with final BSA concentration of 2.5 mg/mL (blue), and CD BSA molar ratios of 1:1 (red), 2:1 (green), 3:1 (purple), and 4:1 (orange). Triplicate measurements were made for all fluorescence and zeta potential measurements and averaged. Error bars denote the standard deviation for averaged experiments.
- Figure 4.2** Encapsulation efficiency (EE%) of CD-BSA-ZIF-8 with final protein concentration 2.5 mg/mL and CD:BSA ratio of 0:1 (blue), 1:1 (orange), 2:1 (gray) 3:1 (yellow), 4:1 (green). Triplicate measurements were made for each system and averaged. Error bars denote the standard deviation of the averaged experiments.
- Figure 4.3** SEM of CD:BSA-ZIF-8 4:1 (a-d) and 70:1 (e-h) at final BSA concentration of 2.5 mg/mL at the following CD:BSA ratios: 1:1 (a,e), 2:1 (b,f), 3:1 (c,g), and 4:1 (d,h). The scale bar in each SEM image is 1 μm .
- Figure 5.1** Encapsulation efficiency of BSA, catalase, myoglobin, and interleukin-2 for γ -CD-MOFs (blue) and β -CD-MOFs (brown). Error determined by triplicates.
- Figure 5.2** (a) PXRD of γ -CD-MOFs and SEM of (b) γ -CD-MOFs (c) BSA@ γ -CD-MOFs (d) catalase@ γ -CD-MOFs (e) myoglobin@ γ -CD-MOFs (f) interleukin-2@ γ -CD-MOFs. Scale bar: 2 μm . (g) Pellet of protein@ γ -CD-MOFs. Scale bar: 1 cm.
- Figure 5.3** (a) PXRD of β -CD-MOFs and SEMs of (b) β -CD-MOFs (c) BSA@ β -CD-MOFs (d) catalase@ β -CD-MOF (e) myoglobin@ β -CD-MOFs (f) interleukin-2@ β -CD-MOFs. Scale bar: 2 μm (g) pellet of protein@ β -CD-MOFs. Scale Bar: 1 cm.
- Figure 5.4** Release profiles of BSA encapsulated in β -CD-MOFs (blue), γ - β -CD-MOFs (brown), and γ -CD-MOFs (orange).
- Figure 5.5** Catalytic assay of free catalase (orange), catalase encapsulated into β -CD-MOF (brown), catalase encapsulated into γ -CD-MOF (blue), and no catalase (gray). Stirring at 300 rpm was used in all solutions during the experiment.
- Figure 6.1** Consequence Value Chart is used to determine a hazard's impact on different aspects of an experiment, such as personal safety, resources, work performance, property damage, and reputation.
- Figure 6.2** Hierarchy of Controls used to minimize risk in experimental procedures. Image from NIOSH.

- Figure 6.3** RAMP presentation on Schlenk line safety by Nehal Idris.
- Figure 6.4** RAMP presentation on nontraditional safety issues of cyber security and fishing by Redford Hudson.
- Figure 6.5** RAMP presentation on glove box safety with 3 different CV calculations based on possible hazards by Paul Hurst.
- Figure 6.6** RAMP presentation on glove box safety with 3 different CV calculations based on possible hazards by Elisa Olivas.
- Figure 6.7** Poster advertising Stress Management and Self-Care sponsored by the UCI GST
- Figure 6.8** Stall wall poster detailing the information needed to access mental health resources for graduate and undergraduate researchers by UCI GST.

LIST OF TABLES

- Table 2.1** Summary of crystal sizes of ZIF-8 at three different HmIm ratios (35:1, 17.5:1, 4:1).
- Table 3.1** Summary of crystal sizes (nm) for ZIF-8 at two different HmIm/Zn Ratios (17.5:1, 35:1) with capillary sizes of 1 and 2mm.
- Table C.1** Encapsulation Efficiency of BSA, Catalase, Myoglobin, and Interleukin-2 in γ -CD-MOFs and β -CD-MOFs.
- Table C.2** d-spacing of γ -CD-MOF and β -CD-MOF, obtained from the PXRD analysis.

ACKNOWLEDGEMENTS

I cannot fully express my gratitude to my advisor, Joe Patterson, who believed in my potential before I did and led me to become the scientist that I am today. Joe has helped me figure out where I fit in the scientific field by allowing me to experiment with many roles and has never turned down a chance for me to learn something new. He has been patient with me in times when I was struggling and always gave me the tools that I needed to make the next steps. Thank you for all your support and trust.

Thank you to Dr. Brooke Carpenter, who was only one year above me when I started in the lab but was a wealth of science and life knowledge. Brooke has been there for me every step of the way, from editing papers late to wine nights and a safe place to share the good and the bad of grad school. I am so thankful for her patience and mentorship.

I am thankful for the members of my dissertation committee, Dr. Maxx Arguilla and Dr. Andy Borovik. Both have been instrumental in my success in this program. I have a special thank you to give to Maxx as the first Filipino professor I have had, and I am so thankful for the safe space and community that he and his wife have provided to the Filipino researchers on this campus. He has allowed me to see myself reflected in higher education and I will be forever grateful for this. Salamat po.

Thank you to my undergraduate advisor, Dr. Anna Larsen, and one of my favorite professors, Dr. Mike Haaf. Anna's mentorship and trust in me allowed me to blossom as a scientist and take charge of my research far before I knew what I was doing and allowed me to learn by doing. Mike has been one of my biggest inspirations in my teaching journey as a graduate student and I still quote his Star Wars puns while teaching organic chemistry. Thank you for showing me the value of truly loving what you do.

Thank you to my friends who have stood by my side through this time and supported me along this journey: Leah, Cindy, and Kito. Leah, I am so appreciative of your unconditional friendship, sage wisdom, and the knowledge that I always have a friend to lean on. Thank you to Kito for deciding to continue our journey as scientists and continue your work and our friendship from Ithaca to UCI; just about 9 years of doing science together and there's no one I'd rather have by my side.

I am incredibly grateful to my friends whom I have met through my time here at UCI: Jen, Nick, Aoon, Cynthia, Mariana, Alissa, Amanda, Nat, Zach, Hannah, Elisa, Riya, Raj, Nina and Ben. Thank you for showing me the humanity of grad school and being around for the good, the bad, trivia night wins, and mimosa tree memories. A special thank you to Nina for your willingness to learn and be mentored by me throughout your undergraduate studies, I wish you all the best in graduate school. You all have made this a once in a lifetime opportunity and I am so honored to be surrounded by such brilliant people.

My loving appreciation goes out to my family, who has been an instrumental part of the support I have felt throughout my academic journey, even when it was hard to explain exactly why I needed to be in college for 5 more years. I am so thankful to have such a large and supportive

family and I wouldn't be here without all of you. Thank you to Tiana for braving graduate school in southern California with me, it was an honor to go through this journey together and pave the way to higher education with you.

I would like to thank my loving partner Shawn, without whom I don't know how I would have survived these past few years. You have been my rock, my silly goose, and most importantly, my best friend. You have challenged me and pushed me to become a better person and I am forever thankful for your support.

My heartfelt appreciation goes out to my parents, Reenah, Joe, and George, without whom I could have never dreamed of this success for myself. Everything that I do, I do to make them proud and honor the choices that they have made to allow all their children to thrive. I will never be able to thank you enough, but I hope that this is a start.

Some of the text of this dissertation is a reprint of material as it appears in *Chemical Reviews*, *Crystal Growth and Design*, *Chemical Society Reviews*, and *Biomaterials Science*. It is fairly used with permission according to the guidelines. All co-authors are mentioned at the beginning of the chapter.

VITA

A. Rain Talosig

Education

- **Ph.D. in Chemistry**, *University of California, Irvine* Aug 2019-Jun 2024
Advisor: Joseph Patterson
- **M.S. in Chemistry**, *University of California, Irvine* Aug 2019-Jan 2021
Advisor: Joseph Patterson
- **BS in Chemistry**, *Ithaca College* Sept 2015-May 2019
Advisor: Anna Larsen

Publications

8. **A. Rain Talosig**, Brooke P. Carpenter, Justin Mulvey, Youli Li, Phillip Kohl, Joseph P. Patterson “Confinement Effects on the Nucleation and Growth of ZIF-8” *Manuscript in Preparation*
7. **A. Rain Talosig**, Fangni Wang, Justin Mulvey, Brooke P. Carpenter, Ben Katz, Chenhui Zhu Joseph P. Patterson “Understanding Polymorph Control in ZIF-8 Nucleation and Growth” *Cryst. Growth Des.*, 2024, **24**, 10, 4136–4142
6. Brooke P. Carpenter, Ben Rose, Elisa M. Olivas, Mariana X. Navarro, **A. Rain Talosig**, Paul J. Hurst, Giuseppe Di Palma, Li Xing, Rweetuparna Guha, Stacy M. Copp, Joseph P. Patterson “The role of protein folding in prenucleation clusters on the activity of Enzyme@Metal-Organic Frameworks” *J. Mater. Chem. A*, 2024, **12**, 813-823
5. Brooke P. Carpenter, **A. Rain Talosig**, Giuseppe Di Palma, Ben Rose, Joseph P. Patterson. “Understanding and Controlling the nucleation and growth of metal-organic frameworks” *Chem. Soc. Rev.*, 2023, **52**, 6918-6937
4. Giuseppe Di Palma, Shannon Geels, Brooke Carpenter, **A. Rain Talosig**, Charles Chen, Francesco Marangoni, Joseph Patterson. “Cyclodextrin metal-organic framework-based protein biocomposites” *Biomater. Sci.*, 2022, **10**, 6749-6754
3. Brooke Carpenter, **A. Rain Talosig**, Jamie Esquivel, Alana Ogata, Dmitry Fishman, Joseph Patterson. “Molecular Modifications of Proteins Affects Crystal Size, Morphology, and Encapsulation Efficiency in Protein-Metal-Organic Frameworks.” *Chem. Mater.* 2022, **34**, 18, 8336–8344

2. A. Rain Talosig, Mario Cosio, Alex Kosanovich, Christopher Pell, Chun Li, Nattamai Bhuvanesh, Jai Zhou, Anna Larsen, Oleg Ozerov. “Distinct Modes of Si-H Binding to Rh in Complexes of a Phosphine-Diarylamido-Silane (SiNP) Pincer Ligand” *Dalton Trans.* 2022, **51**, 14150-14155

1. Aoon Rizvi, Justin Mulvey, **A. Rain Talosig**, Brooke Carpenter, Jovany Merham, Joseph Patterson. “A Closer Look at Molecular Self-Assembly.”. *Chem. Rev.* 2021, **121**, 22, 14232–14280

Conference Presentations

7. University of California Chemical Symposium, Lake Arrowhead, CA **2024**
“Combined In Situ X-ray and Mass Spectroscopy studies of Metal-Organic Framework Nucleation and Growth ” Rain Talosig, Fangni Wang, Brooke Carpenter, Justin Mulvey, Elisa Olivas, Chenhui Zhu, Joseph Patterson (Oral Presentation)

6. BioPacific MIP All User Meeting, Los Angeles, CA **2024**
“Monitoring Nucleation and Growth of Metal-Organic Frameworks” Rain Talosig, Brooke Carpenter, Justin Mulvey, Youli Li, Joseph Patterson (Invited Oral Presentation)

5. Iota Sigma Pi Symposium, Irvine, CA **2023**
“Polymorph Control in Metal Organic Frameworks” Rain Talosig (Poster)

4. Spring MRS Meeting and Exposition, Honolulu, HI. **2022**
“Combined In Situ Synchrotron X-ray and Electron Microscopy Studies of Metal-Organic Framework Crystallization.” Rain Talosig, Brooke Carpenter, Giuseppe DiPalma, Joseph Patterson, Chenhui Zhu. (Oral Presentation)

3. 263rd ACS National Meeting and Exposition, San Diego, CA. **2022**
“Polymorph Control in Protein-Metal Organic Frameworks.” Rain Talosig, Joseph Patterson. (Oral Presentation)

2. 255th ACS National Meeting and Exposition, New Orleans, LA. **2018**
“Synthesis and Spectroscopic Studies of Rhodium Pincer Hydride Complexes” Rain Talosig, Oleg Ozerov, Anna Larsen (Oral Presentation)

1. 254th ACS National Meeting and Exposition, San Francisco, CA. **2017**
“Synthetic and structural studies of low-melting ionic materials with carborane cluster anions” Rain Talosig, Melissa Raymond, Anna Larsen (Poster)

Research Experience

- **Graduate Research, University of California, Irvine** **2019-2024**
Advisor: Joe Patterson
Explored polymorph control of metal organic frameworks through variation in reaction

parameters and studied their formation through SEM, TEM, cryoTEM, PXRD, in-situ XRD, and ESI-MS.

- **UCIMRI Lab assistant, *University of California, Irvine*** **2022-2024**
Advisor: Qinyun Lin
Assisted in training new users, troubleshooting issues and running samples for industry collaborators with SEM (Magellan) and XRD (Smartlab and Ultima III) instruments.
- **LBNL Advanced Light Source, *Berkeley, CA*** **2021,2022**
Utilized 7.3.3 SAXS/WAXS line to investigate time-resolved formation of ZIF-8.
- **SLAC National Accelerator Laboratory, *Sandford, CA*** **2022**
Utilized 4-2 SAXS line to investigate liquid-liquid phase separation
- **BioPacific MIP, *University of California, Santa Barbra*** **2022-2024**
Utilized the next generation SAXS/WAXS system to determine the effects of confinement of a biomolecule in various MOF systems
- **Undergraduate Research, *Ithaca College*** **2016-2019**
Advisor: Anna Larsen
Investigated carborane based low-melting ionic synthesis and physical properties and rhodium pincer ligand complex synthesis and reactivity with a focus on NMR studies.
- **Summer Internship, *Ithaca College*** **2017**
Advisor: Anna Larsen
Investigated rhodium pincer ligand complex synthesis and reactivity with a focus on NMR studies and single-crystal X-ray crystallography.

Industry Experience

- **Internship, *Ecolectro, Cornell University*** **2018**
Supervisor: Kristina Hugar
Explored conductive abilities and synthesis of solid polymer electrolytes and their use in anion exchange fuel cells
- **Internship, *Connora Technologies*** **2016**
Supervisor: Rey Banatao
Explored silicon based recyclable polymer synthesis and properties

Awards and Fellowships

- 9. Best Platform Talk, UCCS **2024**
- 8. Science Communication Fellowship **2024**
- 7. Excellence for leadership in Research Safety, ACS **2023**

6. 1 st place Science as Art MRS	2022
5. 1 st place UCI engineering art competition	2022
4. Sigma Xi Honors Research Society, <i>Ithaca College</i>	2018
3. Summer Internship Cornell Section ACS Award	2017
2. Larry Metzgar Memorial Scholarship, <i>Ithaca College</i>	2017
1. Presidents Scholarship, <i>Ithaca College</i>	2015-2019

Safety Leadership

Graduate Safety Team

An interdisciplinary team of graduate students working to improve overall department safety through workshops, training, seminars, lab inspections and informational graphics.

Patterson Lab Safety Officer

Lead safety initiatives for the Patterson research lab by writing and maintaining SOPs, new hire training, and safety inspections.

ACS CH&S Peer Leadership

Facilitated RAMP training for EH&S professionals and researchers of all levels to minimize and identify risks in lab environments.

Certifications

Industry Insights, *Fall, UCI*

2023

8-week course for STEM scientists to learn about industry structure, function and growth, 1st place earned in business pitch competition.

Mentorship

Departmental Mentor (CHEMUnity)

Mentoring outside graduate students to navigate different stages of PhD and provide insight on career development. (3 students)

Undergraduate Mentor

Mentoring undergraduate students in the lab to gain research experience and career development. Provide insight on the transition from undergraduate to graduate school. (2 Students)

Teaching Assistant Appointments

Organic Chemistry Lecture
 General Chemistry Lecture
 General Chemistry Lab
 Analytical Chemistry Lab

Leadership/Outreach

UCI: Corona Library Project, Irvine Unified School District Science Fair Mentor, , poster presentation judge for SoCal Undergraduate Research Conference, ACS CHAS peer lead workshop facilitator, Co-chair of LGBTQ+ MRS special interest group, MSE middle school outreach

IC: Chemistry Club, Spooky Science, Peer Tutor, Undergraduate TA program, WICB radio.

ABSTRACT OF THE DISSERTATION

Understanding the Nucleation and Growth of ZIF-8 Polymorphs

by

A. Rain Talosig

Doctor of Philosophy in Chemistry

University of California, Irvine, 2024

Professor Joseph Patterson, Chair

Metal-organic frameworks (MOFs) present a diverse platform for designing high-performance materials with applications spanning drug delivery, catalysis, sensing, and separation. MOF polymorphism has been widely studied from the perspective of which synthetic factors, such as ligand-to-metal ratio, solvent, and temperature, can be used to control the final polymorph formation. However, limited studies on the nucleation mechanism of multi-polymorph MOFs have been performed. This dissertation aims to highlight the study and understanding of metal-organic framework polymorphs and how to observe and control polymorph formation. Advanced microscopy, scattering and spectroscopy techniques such as cryogenic transmission electron microscopy (cryoTEM), scanning electron microscopy (SEM), powder x-ray diffraction (PXRD), and electrospray ionization mass spectrometry (ESI-MS) are employed to conduct these studies. Here we study the formation of a model zeolitic imidazole framework-8 (ZIF-8) and the mechanism that drives the formation of the two most observed polymorphs, sodalite (SOD) and diamondoid (dia). To understand the mechanism and factors that affect polymorph formation, the prenucleation clusters were studied mainly through in-situ WAXS and ESI-MS, uncovering the role of prenucleation cluster size on the polymorph formation. In a follow up study, we investigate the effect of confinement through reaction vessel size on the nucleation and growth of ZIF-8. This study is of importance for studies involving analytical techniques where the experimental reaction volume varies from the bulk reaction. In addition, we study the encapsulation of bovine serum

albumin (BSA) in ZIF-8 frameworks and the effect of supramolecular modification with cyclodextrin on the encapsulation efficiency. To further the studies with cyclodextrin, cyclodextrin-based MOFs are studied to understand their encapsulation efficiency and structure. In summary, this work provides insights into the field of MOF nucleation and growth through a lens of polymorph control and lays the foundation for the development of new MOFs.

Chapter 1:

Introduction

A portion of this chapter appears in the following publications and has been re-formatted for this thesis:

Brooke P. Carpenter, **A. Rain Talosig**, Ben Rose, Giuseppe Di Palma, and Joseph P. Patterson. “Understanding and Controlling the Nucleation and Growth of Metal-Organic Frameworks.” *2023. Chem. Soc. Rev., 2023, 52, 6918-6937*

Aoon Rizvi, Justin Mulvey, Brooke Carpenter, **A. Rain Talosig**, Jovany Merham, Joseph Patterson. “A Closer Look at Molecular Self-Assembly.” *2021. Chem. Rev. 2021, 121, 22, 14232–14280*

Chapter 1: Introduction

1.1 Metal-Organic Frameworks

Metal-organic frameworks (MOFs), also known as porous coordination polymers, are highly ordered materials composed of an organic linker and coordination metals (Figure 1.1). In the past two decades, they have been of interest because of their high surface area and permanent high porosity.¹ The synthesis and development of MOFs have been highly rewarding because of the flexibility and variation that the precursors give. A large amount of structural diversity can be found in the MOF motif because of the wide variation of different organic linkers and coordinating metal cations.² MOFs can be applied to many fields in different applications due to the fairly simple functionalization of the linkers which can be pre-synthesized or functionalized after MOF formation. The permanent and highly tunable porosity of MOFs has led to applications in gas storage, separation, sensing, and catalysis. Although many MOFs have been formed, it has been a process of trial and error without much precision in synthesizing the desired product.^{3,4} This has been a large roadblock in MOF research due to the time-consuming nature of empirical screening, which has made scale-up of these processes difficult. Learning more about the crystallization pathways of different MOFs and finding a common way to analyze different self-assembling systems opens the prospect of crystal engineering in MOFs. This can be achieved through methods devised by fundamental properties of similar systems rather than high throughput screening.

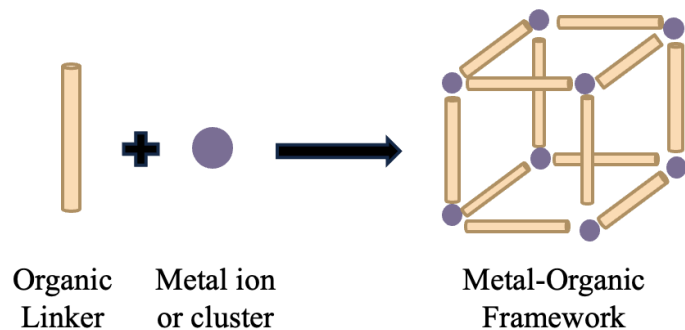


Figure 1.1 Metal-organic framework general reaction scheme.

1.2 Nucleation and Growth Theories and Models

Classical Nucleation and Growth

To create a basis to study crystallization in MOFs, it is necessary to look at previously studied crystal growth mechanisms in other systems. The most common crystallization model is the classical nucleation theory (CNT). CNT can be outlined by homogenous nucleation that describes the nucleation of a new thermodynamic phase, in the case of MOFs from liquid solution to solid. Solutions reach a supersaturation point where the crystallization is thermodynamically driven.⁵

$$\Delta G = \frac{-4\pi r^3}{3v} K T \ln S + 4\pi r^2 \sigma \quad (\text{Equation 1})$$

The CNT model states that the formation of a nucleus occurs with two major contributions, a negative contribution from the difference in chemical potential per unit volume between the crystal and the liquid phase ($\Delta\mu$), and a positive contribution from the unfavorable interfacial free energy between the two phases (γ). Overall, this leads to a free energy that is dependent on radius size (r), shown in equation 1. To reach the most stable thermodynamically favorable

crystallization, CNT describes a critical nucleus size (r^*) which maximizes the free energy (Figure 1.2).

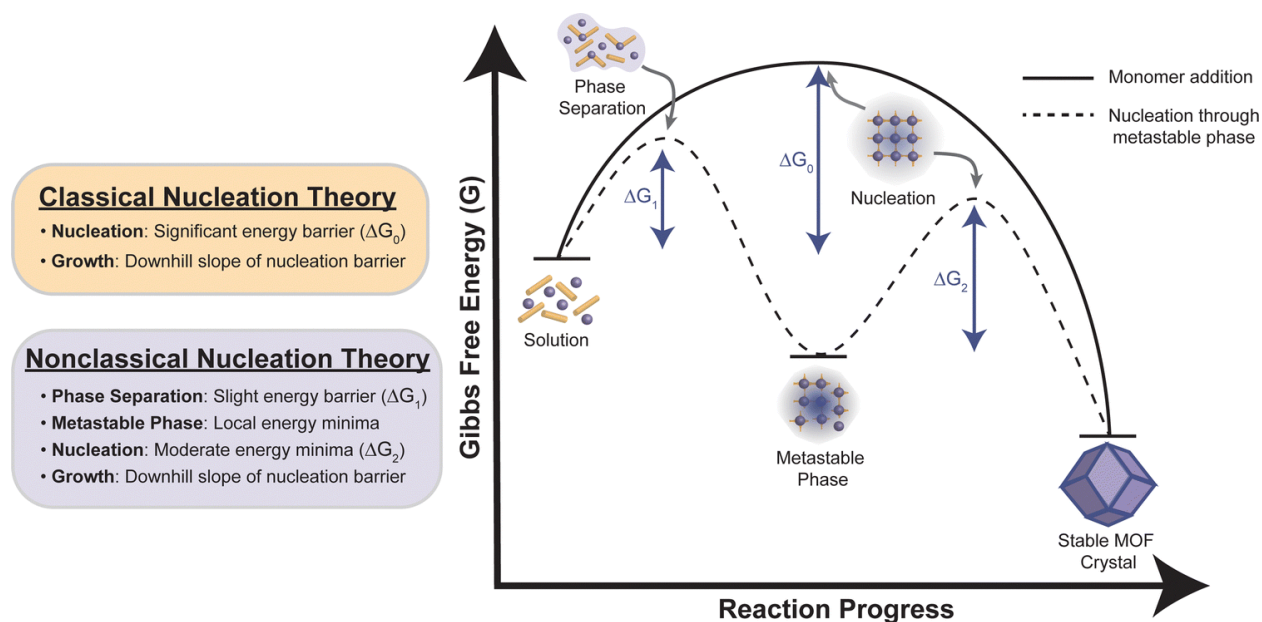


Figure 1.2 Free energy diagram comparing monomer addition (classical nucleation theory) and nucleation through metastable phase (nonclassical nucleation theory) mechanisms.

The critical nucleus is in metastable equilibrium so any addition of molecules will lower the free energy, this makes it more likely to find nucleation sites of the critical nucleus size. The critical nucleus size can vary between systems and can have wide ranges that are influenced by the shape and boundaries of the nucleus. Although CNT describes simple nucleation and growth theories, it has many shortcomings. The pitfalls of CNT are shown because it is unable to explain the vanishing nucleation barrier at high supersaturation points. CNT also makes assumptions that the most thermodynamically stable phase will be the first one to form and that there are no other amorphous or crystalline phases that could form.

Non-Classical Nucleation and Growth

Non-classical nucleation and growth, also described as heterogenous nucleation, proceed through numerous intermediate stages before reaching a global thermodynamic minimum. This theory was first outlined in the Ostwald Step rule that when a particle proceeds through the steps of nucleation and growth, the particle will find a local thermodynamic minimum before finding the lowest thermodynamic state.⁶ The phase with the lowest free energy barrier relative to the solution will be the first to nucleate, rather than the most thermodynamically stable phase, with respect to entropy. Moving through this model, particles move stepwise to the next most stable intermediate, potentially moving through many polymorphs. Many of the transformations that take place in the formation of MOFs go through sequential non-classical stepwise transformations that might individually follow CNT. These structural transformations can take place through dissolution-recrystallization or solid phase rearrangement. These transformations can be monitored through in situ methods such as X-ray scattering⁷, mass spectrometry (MS)⁸, and cryo-electron microscopy (cryoEM).⁹ The presence of a metastable intermediate observed in nonclassical nucleation was first proposed by protein crystallization where the nucleation rate is expressed as a function of protein concentration and temperature.¹⁰

Crystallization by Particle Attachment

Crystallization by particle attachment (CPA), is a nucleation and growth theory that describes assemblies of coaligned nanocrystals. Monomers are dispersed in a solution and assembled via aggregation to form larger structures that can then be added together to form the final kinetically and thermodynamically stable crystal. The intermediate structures may be amorphous but in many cases are structurally distinct from the final crystalline form.¹¹ Like CNT, the magnitude of the free energy barrier to nucleation determines the size and shape of the

particles produced, taking into consideration thermal energy as a crucial factor. At low supersaturation, the free energy barrier is large and the possibility of generating a critical nucleus size is a rare event. Due to the rarity of the ideal nucleation, it is not likely that any other critical nuclei with the same composition will run into each other leading to monomer addition similar to CNT. As the supersaturation increases, the free energy barrier of the phase change decreases, and the particles are generated more rapidly. These particles can transform in size and composition by exchanging monomers between the particles. When the supersaturation reaches a point where the free energy barrier is near kBT , the solution can undergo spinodal decomposition where the particles are generated so rapidly that the growth takes place purely by collision with other particles.¹²

In the cases where the free energy landscape displays a barrier, thermodynamically the system will grow as one large particle. There are no metastable intermediates because they do not reside in a local free energy minimum, but particles arise and exhibit CPA growth behavior. When the landscape contains local free energy minima, there is the possibility of the formation of other particles that are thermodynamically favored. In this case, some morphologies are not seen in the bulk product that are observed in the formation. CPA and CNT are similar as they both assume small growth and unit attachment, but this theory accounts for the different morphologies that do not represent the surface energy minimization that is important in CNT. This growth is seen clearly in zeolitic frameworks, such as $MgSO_4$ and $CaCO_3$. In zeolite synthesis, there are transient nanoparticles that are referred to as “nanoslab” of crystalline intermediate phases that show evidence of aggregation. This type of growth seen in zeolite frameworks can be related to zeolitic imidazole frameworks (ZIFs) which are a subset of MOFs.¹³

Zeolite Nucleation and Zeolitic Imidazolate Frameworks

Zeolites are inorganic molecules that are composed of metal tetrahedral nodes, typically Si or Al, that are linked by oxygen atoms.¹⁴ Along with the structural motif similarities, zeolites and MOFs have permanent porosity, topological diversity, and similar synthetic routes.¹⁵ Due to the diversity of organic linkers and metal nodes, MOFs have more structural diversity and can be used in a variety of different applications. The nucleation and growth of zeolites proceed through an amorphous gel within the monomer model where the arrangement of the gel phase is restructured. The Si-O-Si bonds will break and reform until the most stable polymorph is formed. The monomer growth model is not described by CNT because it contains restructuring from within rather than the formation of the most stable structure initially. Another way to model zeolite formation is to consider the nature of the building units that are used in the formation of the crystal. In this model, secondary building units (SBU) describe the smallest structural units of the product crystal. In this model of growth, the SBU grows onto an already existing nucleus and the amorphous gel acts as a reservoir where the heterogeneous nucleation can take place. In this model, the gel does not lead to the formation of the final crystal but acts as a formation point. The last possibility is nanoparticles developing structures internally, the nanoslab model, also described by CPA or aggregation.

Zeolitic imidazolate frameworks (ZIFs) are a subclass of MOFs that are topologically similar to zeolites.¹⁶ ZIFs are composed of tetrahedrally coordinated transition metal ions that are connected by imidazolate linkers. In the case of zeolitic imidazolate framework-8 (ZIF-8), the framework is formed by the coordination of Zn^{2+} ions and 2-methylimidazole forming two common morphologies: the more common sodalite (SOD) which has a standard dodecahedral morphology, and the more stable diamondoid (dia) that appears to be a stack of more flat

crystals.¹⁷ ZIF-8 has been thoroughly investigated, in part, because it can be synthesized in water at room temperature.

1.3 Polymorphism in MOFs

MOFs can exhibit polymorphism, where MOF crystals can consist of identical chemical compositions but differ in their network topology.¹⁸ As a result, multiple crystalline phases of MOFs can be produced with different symmetries and densities. By tuning the activation energy of the MOF through changing synthesis conditions, higher energy products can be kinetically trapped at low activation energy barriers or the reaction can proceed to the lower energy thermodynamic products at high activation energy barriers; thus polymorphs can be found at different energy minima of a free energy landscape diagram.¹⁹ Since polymorphs can display different crystal structures while retaining identical molecular composition, the structure-function relationship based on structural parameters can be investigated.^{20,21} Polymorph transition can be induced post-synthesis through physical steps like additional heating,²² pressure, or template mediation.²³ Typically, post-synthetic phase transitions result in the formation of more dense, thermodynamic crystalline phases through reconstruction or displacement of internal structures.²⁰ For example, washing of ZIF-8 MOFs synthesized in water with alcohol solvents can initiate phase change from ZIF-C and ZIF-L to ZIF-8 (SOD).^{24,25} Additionally, intrinsic and extrinsic synthetic conditions can control the competition among polymorph phases during the MOF formation.²⁶ For example, the use of template vapors in

chemical vapor deposition enables control over the formation of a porous or nonporous ZIF polymorph.²³

While polymorphism is often not screened in MOF studies, mechanistic studies of zeolites, which have ~250 different polymorphs,²⁷ have aided in polymorph control of MOFs, as the metal-ligand coordination in ZIFs is similar to the building units of inorganic zeolites. Whereas zeolites are composed of SiO₄ and AlO₄ units, ZIFs have tetrahedral metal centers, commonly divalent metals such as Zn²⁺ or Co²⁺, that are bridged with imidazolate ligands. Consequently, ZIFs share many of the same network topologies and rich polymorphisms as zeolites.²⁸ In all zeolite polymorphs' formation reactions, primary amorphous phases form, followed by secondary amorphous phases. Recent computational studies have determined the rate at which this secondary amorphous phase grows into a crystalline phase determines the final polymorph selection.²⁹ Polymorphs with distinct physical properties can be produced by altering the packing density of the building units as well as the orientation of the imidazolate units. For example, ZIF-8 SOD, which is the most widely studied kinetic polymorph of ZIF-8, is the least densely packed, resulting in large pores (~11.4 Å) that are ideal for encapsulating guest molecules.³⁰ In contrast, ZIF-8 diamondoid (*dia*), which is the most thermodynamically stable polymorph, is the most densely packed and not ideal for encapsulating guest molecules. Polymorphs of ZIFs can be revealed through in-situ monitoring techniques such as in situ PXRD, which allowed for the observation of a new metastable ZIF-8 polymorph generated through mechanochemical milling, *kat*.¹⁷ Additionally, cryoTEM studies have shown amorphous particles emerge for the formation of ZIF-8 SOD and *dia* polymorphs.⁹ While these TEM studies have also shown that the amorphous particles undergo a redissolution-crystallization mechanism for SOD, a separate mechanism is suggested for *dia* formation that requires further exploration.

1.4 Controlling MOF Nucleation and Growth

Confinement of MOFs

Nanoscale confinement has been widely used to design high-performance materials with hierarchical structures in the biomineralization community. Nanoscale confinement influences occur in restricted volumes such as membranes and pores which can limit crystal growth in the x , y , or z dimensions. The confinement's character can significantly influence the nucleation rate and stability of intermediate phases. By increasing the degree of confinement on a system—lowering the volume where synthesis and crystallization can take place—studies have observed a decrease in the nucleation rate of crystallization. This decrease is due to a decrease in any impurities that could act as nucleators and volume is proportional to nucleation probability.³¹

Nanoscale confinement has been shown to stabilize metastable products and phases for non-MOF systems. For example, a study found that by increasing the degree of confinement during the crystallization of amorphous calcium carbonate, the amorphous phase was stabilized.³² This is due to the energy barrier for the thermodynamic product increasing. In addition to the degree of confinement affecting growth, the surface area of the synthesis vessel can have a further effect. For example, when a system is assembling in a porous confinement, a greater fraction of the nucleus will be in contact with the substrate and thus have a greater nucleation rate than in a system that occurs within flat confinement.³² Confinement methods using various interfaces, such as colloforms³³ and droplets,³⁴ have synthesized MOF nanoparticles with high uniformity and low size distribution. The key to obtaining such products

lies in having fast nucleation but slow growth. Synthesizing a MOF in a confined environment allows this to occur as it decreases the probability for nuclei to aggregate.

Confinement interfaces have shown the potential to serve as templates for controlling the growth direction of crystals by restricting growth in designated orientations. Many studies have succeeded with this method by using emulsion interfaces to confine MOF growth within a specific geometric mold. By varying the length of the surfactant in a reverse micelle system, ZIF-8 crystals with targeted sizes could be achieved.³⁵ One specific study used an aqueous–organic liquid interface to mold HKUST-1, ZIF-8, and LnBT crystals into a wide range of crystal geometries such as hearts, circles, and rectangles.³⁶ The ability to obtain each crystal geometry was based on localizing the nucleation and growth within molds of specific geometries. This mold was stationed at an opening in the interface surface where its shape could be altered by varying buoyancy and capillarity forces. In addition to emulsion interfaces being used to control crystal shapes, hard confinement surfaces can template MOFs with hierarchical structures and porosity. Synthesizing such hierarchical materials can be advantageous for catalytic applications as demonstrated with PCN-224 which was synthesized within the confinement of macroporous melamine foam to create geometry that promoted greater catalytic activity.³⁷

While studies have used nanoscopic confinement methods to synthesize MOFs with desired physical properties, future research is still needed to use confinement as a method to discover and trap metastable MOF products. Additionally, on the other side of the spectrum, nucleation and growth mechanisms that occur during macroscopic scaling of a MOF synthesis are currently unexplored. Such mechanistic studies are crucial for designing large-scale MOF synthesis using green approaches, as many current synthetic approaches in industry use toxic solvents and MOF precursors along with pressure-sealed reaction vessels, all of which pose high

financial costs.^{38,39} Recently, advances towards this challenge include a study by Deacon *et al.* which investigated kilogram-scale production of ZIF-8 while using water as the solvent. The authors note that the crystals observed in the scale-up synthesis have distinctly different sizes than those reported in literature from small-scale synthesis.²⁴ Such findings emphasize the impact that scaling has on final MOF crystals and the need for mechanistic studies.

Surfaces and Biomolecules

Surface substrates have shown great potential for nanoscale control of crystal formation,⁴⁰ aiding in the discovery of new types of materials for CO₂ separation,⁴¹ water splitting,⁴² and field-effect transistors.⁴³ Surfaces control the self-assembly pathway of crystal formation by modifying the interfacial free energy barrier and offering a site for crystals to nucleate (Figure 1.2).⁴⁴ The effects of surfaces themselves on crystal growth are usually not as pronounced, although confinement by surfaces can noticeably affect growth of MOFs. The extent of which a surface can modify crystal nucleation is largely dependent on two factors: (1) atomic structure of the surface and (2) the strength of the bonds formed by the MOF precursors and the surface. By matching the atomic structure of a surface to a desired lattice plane of a crystal, surfaces can be used to control the orientation of the crystal lattice by minimizing the lattice strain in a desired orientation. Planar substrates include flat, smooth surfaces such as alumina³⁵ and silica^{45,46} and provide a uniform surface for MOFs to grow.

Another aspect to consider when choosing a surface is the chemical composition of the surface interface. The interfacial chemistry can be used to modulate the binding strength of the MOF precursors to the surface, and consequently, the probability of nucleation. By the MOF precursors forming stronger bonds with the surface rather than with the solvent molecules, the interfacial energy barrier required for nucleation decreases.⁴⁷ The available surface area for

strong-bonds to form can also impact the probability of nucleation. Non-planar substrates, which are surfaces that are more complex and have three-dimensional structures, provide a larger surface area for the MOFs to grow on, leading to faster formation and higher yields.^{48–50} Examples of non-planar substrates include foams,⁵¹ fibers,⁵² nanowires,⁵³ proteins,^{50,54–56} and porous metals.^{57,58} A study by Ogata *et al.* used bovine serum albumin as a non-planar substrate to lower the interfacial energy barrier and tune the crystal morphology and structure.⁹ In the study, cryo-TEM observed that a protein was capable of concentrating MOF precursors, forming amorphous protein/Zn/HmIm particles and, subsequently, ZIF-8(sod) crystals through a dissolution recrystallization mechanism. Otherwise, in the absence of protein, ZIF-8(dia), the nonporous and thermodynamically stable ZIF-8 polymorph, formed (Figure 1.3). The ability for the protein to drive crystal formation of ZIF-8 (sod) was strictly dependent on its negatively charged surface as other studies have shown that biomolecules with high isoelectric points (>7) cannot promote crystal formation.⁵⁰ With this insight, molecular modifications of proteins have shown to be promising methods for tailoring the surface chemistry to promote nucleation and growth of a particular MOF phase and morphology.⁵⁹ Furthermore, proteins are believed to add to the growing crystal through particle addition. Through addition, the proteins create defects in the crystal as they are too complex to match the lattice planes of the MOF.^{56,59} By controlling the size and concentration of protein particles, such defects can be tailored.

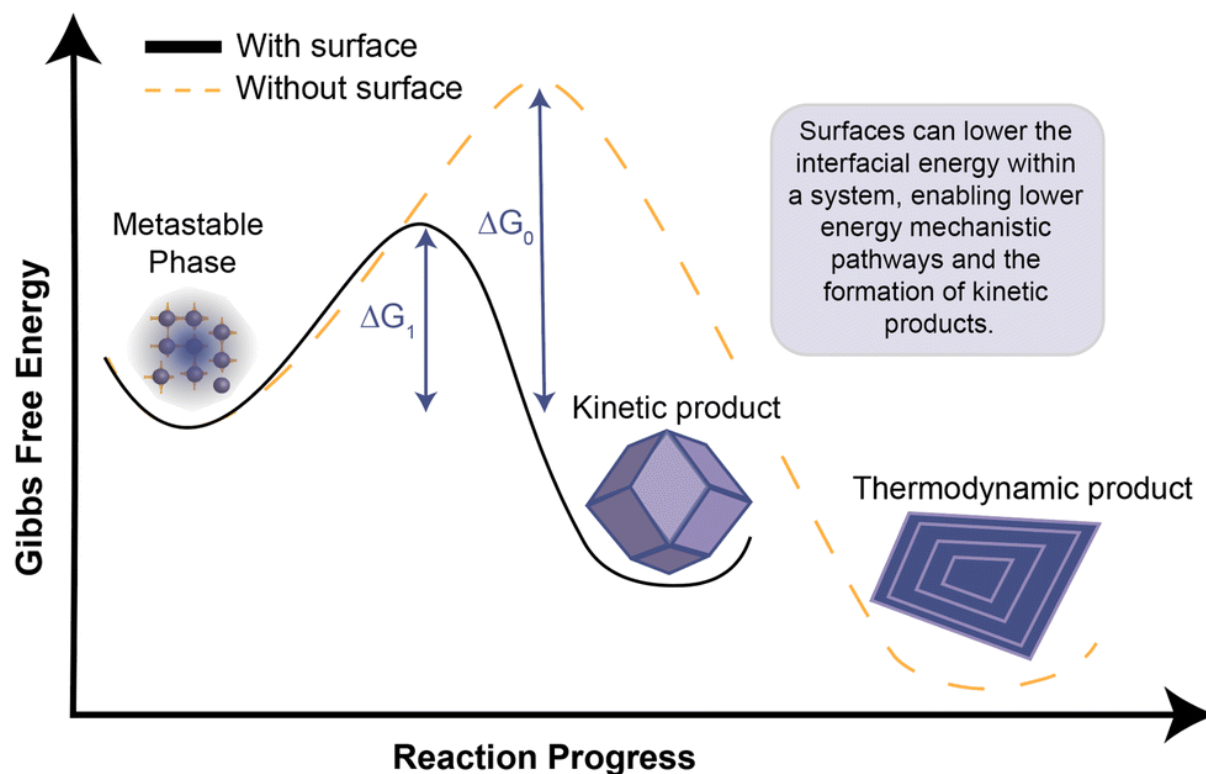


Figure 1.3 Comparison of free energy barrier in homogeneous (without surface) and heterogeneous crystallization (with surface).⁶⁰

Along with biomolecules, polymers can also serve as templates to regulate the crystalline phase, shape, size, and porosity of MOFs.⁶¹ Ionic polymers offer many coordination sites for MOF nucleation, while instead, non-ionic polymers may self-assemble to influence the final MOF structure and porosity through electrostatic interactions. For example, through a coordination–modulation mechanism, a non-ionic block copolymer was able to trap a kinetic crystalline phase through stabilization of prenucleation aggregates.⁶² In summary, each type of surface has its own benefits for tailoring the nucleation and growth of MOF formation. For example, if a planar substrate is being used, a fabrication method may be developed that takes advantage of the flat and smooth surface of the substrate to help control the growth and formation of the MOFs in a precise and uniform manner. On the other hand, if a non-planar

substrate is being used, a fabrication method may be developed that can adequately grow the MOFs on the more complex surface of the substrate, potentially leading to faster formation, higher yields, and trapping of kinetic products.

1.5 Monitoring MOF Nucleation and Growth

MOF nucleation and growth contain complexity that no single instrumentation method can capture. Each instrument has its strength as some instrumental techniques allow for the characterization of a specific localized region and provide qualitative insight into individual crystal size and morphology, while other techniques provide ensemble information and quantitative insight into the crystallization kinetics (Figure 1.4). Complimentary instrumentation methods are required to obtain a complete view of the crystallization by providing descriptions of each phase and phase transitions. The instruments will be discussed in more detail and examples of how each technique can be used to monitor MOF nucleation and growth.

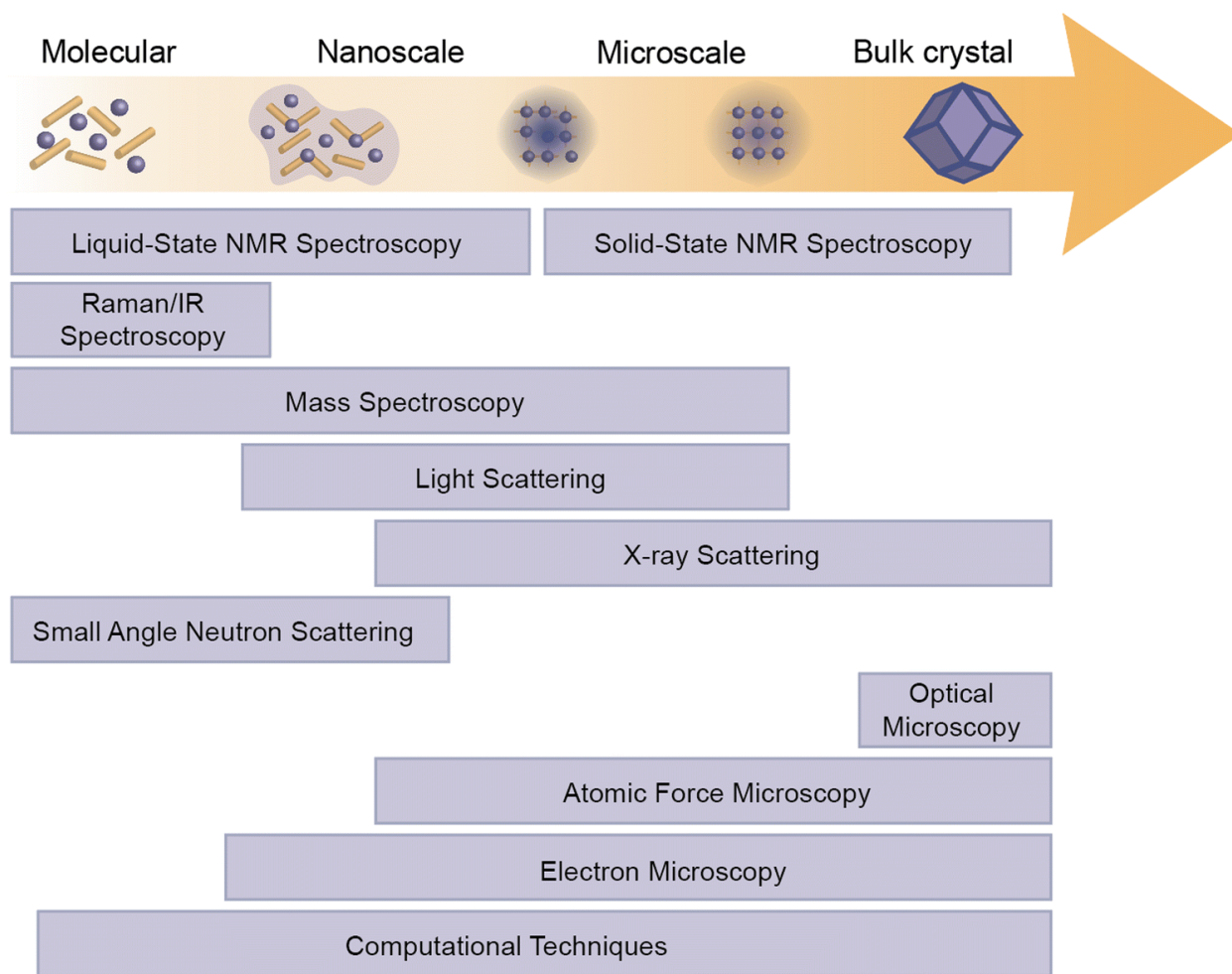


Figure 1.4 Summary of experiential and computational techniques used to study nucleation and growth of MOFs and of the phase regime that they are useful for probing.

X-Ray Techniques

X-ray scattering techniques utilize X-rays as radiation sources, allowing for high resolution due to the short wavelengths of X-rays compared to visible light. Scattering methods can provide insight into the nucleation and growth mechanisms of MOFs through an understanding of the morphological and structural evolution studies of the crystalline and amorphous phases. X-ray diffraction (XRD) is a subclass of X-ray scattering where the scattered radiation is elastic and is limited to measuring crystalline structures. XRD is not ideal for the

early stages of MOF nucleation due to the lack of resolution sub-nano crystalline size regime. Powder XRD (PXRD) has been used to track the final morphology of MOF crystals through characteristic Bragg peaks.⁶³

Small-angle X-ray scattering (SAXS) and wide-angle x-ray scattering (WAXS) are methods of X-ray scattering that can identify crystallographic information as well as probe size and shape of the crystalline and amorphous phases. SAXS is extremely useful in monitoring the early stages of nucleation and growth as it can measure MOF growth in the 1-100nm range. This is useful when analyzing samples that are amorphous, semi-crystalline or crystalline. X-ray scattering can be used to resolve mechanisms of growth and formation by monitoring changes in peak intensity as a function of time and can give insights into the rate of crystallization. Phase changes can be monitored by x-ray scattering and were demonstrated in work done by Katsensis and coworkers where in situ x-ray scattering was used to monitor the changes of ZIF-8 while applying mechanical stress and revealed a transformation into a previously unresolved intermediate structure. WAXS measurements detect larger diffraction angles, analogous to XRD, and can be used to monitor changes in crystalline phases as well. WAXS is typically used to monitor transition phases of MOF formation that would not be captured by diffraction and has been used to elucidate kinetic information about MOF growth.

Microscopy Techniques

Microscopy methods provide images of localized regions of a sample enabling phases that occur simultaneously to be distinguished. The resolution and viewing range of a sample is determined by the wavelength of the beam source and the voltage at which the beam is emitted. Scanning electron microscopy (SEM) and transmission electron microscopy (TEM) have been utilized in time-resolved studies of MOFs. Both techniques probe the sample interaction with an

electron beam and monitor either the scattering or transmission of electrons. SEM is used to provide topologies of large areas of MOFs and determine their surface structure. When used in conjunction with XRD it can be a useful tool for determining the crystal structure topology for various polymorphs.⁶⁴ SEM can be used to study various bulk materials, but TEM is more limited to thin films but can generate a much higher resolution image. TEM requires a higher electron beam dose and MOFs are susceptible to beam damage, so fewer studies use TEM to analyze MOFs.⁶⁵ Recent work with cryo-TEM and liquid cell TEM has allowed MOFs to be more closely studied by TEM while lowering the amount of beam damage.⁶⁶ Low dose TEM advancements have allowed for the determination of crystalline structures⁶⁷, morphologies⁶⁸, local defects^{65,69}, encapsulation of guest species⁷⁰, self-assembly mechanisms⁹, and dynamics^{71,72}.

1.6 Dissertation Overview

In this dissertation, the nucleation and growth mechanisms of MOFs are probed with a particular focus on polymorph control the kinetics and thermodynamics of crystal formation. Such studies are essential to the prediction and development of new MOF systems with finely tuned sizes, morphologies, topologies, and surface chemistries. In each chapter, electron microscopy and x-ray diffraction are used as complementary techniques to characterize intermediate phases and/or final crystal topologies. Products from this dissertation work have resulted in two research chapters, **Chapters 1, 2 and 5** are published in peer-reviewed journals. **Chapter 3 and Chapter 6** are in preparation for peer review and are anticipated to be submitted

during the Summer and Fall of 2024. **Chapters 4 and 7** are intended as stand-alone chapters for this dissertation.

Chapter 1 introduces the field of MOFs while discussing the many theories on MOF nucleation and growth. Then polymorphism in MOFs is discussed to understand how similar synthetic parameters can result in MOFs with a large variation in size, topology, structure, and function. Experimental methods are provided to guide the probing of MOF crystal formation across multiple scale regimes.

Chapter 2 investigates how polymorph formation can be understood by probing the initial stages of nucleation and growth with in-situ techniques such as WAXS and ESI-MS. The possible stages of nucleation and growth are understood by modeling the clusters that were observed in the spectroscopy measurements.

Chapter 3 discusses the effect of confinement conditions on the nucleation and growth of MOFs. This work shows that in confined conditions, the growth is slowed and there is less overall crystallinity observed through stabilization of amorphous precursors. This work highlights a collaboration with the NSF BioPacific facilities and utilizes WAXS and SEM.

Chapter 4 investigates the encapsulation of biomolecules within MOF framework and discusses the supramolecular modification of a model biomolecule, bovine serum albumin, with cyclodextrin to enhance encapsulation and activity.

Chapter 5 utilizes cyclodextrin-based MOFs to encapsulate biomolecules and target drugs to investigate the encapsulation, release profile, and activity of cyclodextrin-based biocomposites.

Chapter 6 discusses work done in the field of lab safety and the leadership initiatives

that have been implemented in my time as a safety officer and a member of the UCI graduate safety team. This work focuses on tools for functional risk assessment and the intersection of mental health awareness and chemical lab safety.

Chapter 7 summarizes the major findings of this work and discusses the promising Future in the study of MOF nucleation and growth.

1.7 References

- (1) Morris, R. E. How Does Your MOF Grow? *ChemPhysChem* **2009**, *10* (2), 327–329. <https://doi.org/10.1002/cphc.200800642>.
- (2) Cheetham, A. K.; Rao, C. N. R.; Feller, R. K. Structural Diversity and Chemical Trends in Hybrid Inorganic–Organic Framework Materials. *Chem. Commun.* **2006**, No. 46, 4780–4795. <https://doi.org/10.1039/B610264F>.
- (3) Islamov, M.; Babaei, H.; Anderson, R.; Sezginel, K. B.; Long, J. R.; McGaughey, A. J. H.; Gomez-Gualdrón, D. A.; Wilmer, C. E. High-Throughput Screening of Hypothetical Metal–Organic Frameworks for Thermal Conductivity. *Npj Comput. Mater.* **2023**, *9* (1), 1–12. <https://doi.org/10.1038/s41524-022-00961-x>.
- (4) Wang, S.; Cheng, M.; Luo, L.; Ji, X.; Liu, C.; Bi, K.; Zhou, L. High-Throughput Screening of Metal–Organic Frameworks for Hydrogen Purification. *Chem. Eng. J.* **2023**, *451*, 138436. <https://doi.org/10.1016/j.cej.2022.138436>.
- (5) Karthika, S.; Radhakrishnan, T. K.; Kalaichelvi, P. A Review of Classical and Nonclassical Nucleation Theories. *Cryst. Growth Des.* **2016**, *16* (11), 6663–6681. <https://doi.org/10.1021/acs.cgd.6b00794>.
- (6) Threlfall, T. Structural and Thermodynamic Explanations of Ostwald’s Rule. *Org. Process Res. Dev.* **2003**, *7* (6), 1017–1027. <https://doi.org/10.1021/op030026l>.
- (7) Cravillon, J.; Schröder, C.A.; Nayuk, R.; Gummel, J.; Huber, K.; Wiebcke, M. Fast Nucleation and Growth of ZIF-8 Nanocrystals Monitored by Time-Resolved In Situ Small Angle and Wide-Angle X-ray Scattering. *Angew. Chem., Int. Ed.*, 2001, **50**, 8067–8071 <https://onlinelibrary.wiley.com/doi/10.1002/anie.20110207>.
- (8) Filez, M.; Caratelli, C.; Rivera-Torrente, M.; Muniz-Miranda, F.; Hoek, M.; Altelaar, M.; Heck, A. J. R.; Van Speybroeck, V.; Weckhuysen, B. M. Elucidation of the Pre-Nucleation Phase Directing Metal–Organic Framework Formation. *Cell Rep. Phys. Sci.* **2021**, *2* (12), 100680. <https://doi.org/10.1016/j.xcrp.2021.100680>.
- (9) Ogata, A.; Rakowski, A.; Carpenter, B.; Fishman, D. Direct Observation of Amorphous Precursor Phases in the Nucleation of Protein–Metal–Organic Frameworks *J. Am. Chem. Soc.*, 2020, **142**, 1433–1442 <https://pubs.acs.org/doi/abs/10.1021/jacs.9b11371>

- (10) Wolde, P. R. ten; Frenkel, D. Enhancement of Protein Crystal Nucleation by Critical Density Fluctuations. *Science* **1997**, *277* (5334), 1975–1978. <https://doi.org/10.1126/science.277.5334.1975>.
- (11) De Yoreo, J. J.; Gilbert, P. U. P. A.; Sommerdijk, N. A. J. M.; Penn, R. L.; Whitlam, S.; Joester, D.; Zhang, H.; Rimer, J. D.; Navrotsky, A.; Banfield, J. F.; Wallace, A. F.; Michel, F. M.; Meldrum, F. C.; Cölfen, H.; Dove, P. M. Crystallization by Particle Attachment in Synthetic, Biogenic, and Geologic Environments. *Science* **2015**, *349* (6247), 6760. <https://doi.org/10.1126/science.aaa6760>.
- (12) Scheifele, B.; Saika-Voivod, I.; Bowles, R. K.; Poole, P. H. Heterogeneous Nucleation in the Low-Barrier Regime. *Phys. Rev. E* **2013**, *87* (4), 042407. <https://doi.org/10.1103/PhysRevE.87.042407>.
- (13) Aerts, A.; Kirschhock, C. E. A.; Martens, J. A. Methods for in Situ Spectroscopic Probing of the Synthesis of a Zeolite. *Chem. Soc. Rev.* **2010**, *39* (12), 4626–4642. <https://doi.org/10.1039/B919704B>.
- (14) Li, R.; Chawla, A.; Linares, N.; Sutjianto, J. G.; Chapman, K. W.; Martínez, J. G.; Rimer, J. D. Diverse Physical States of Amorphous Precursors in Zeolite Synthesis. *Ind. Eng. Chem. Res.* **2018**, *57* (25), 8460–8471. <https://doi.org/10.1021/acs.iecr.8b01695>.
- (15) Li, L. J.; Chu, C.-H.; Yu, O. Y. Application of Zeolites and Zeolitic Imidazolate Frameworks in Dentistry—A Narrative Review. *Nanomaterials* **2023**, *13* (22), 2973. <https://doi.org/10.3390/nano13222973>.
- (16) Chen, B.; Yang, Z.; Zhu, Y.; Xia, Y. Zeolitic Imidazolate Framework Materials: Recent Progress in Synthesis and Applications. *J. Mater. Chem. A* **2014**, *2* (40), 16811–16831. <https://doi.org/10.1039/C4TA02984D>.
- (17) Katsenis, A. D.; Puškarić, A.; Štrukil, V.; Mottillo, C.; Julien, P. A.; Užarević, K.; Pham, M.-H.; Do, T.-O.; Kimber, S. A. J.; Lazić, P.; Magdysyuk, O.; Dinnebier, R. E.; Halasz, I.; Friščić, T. In Situ X-Ray Diffraction Monitoring of a Mechanochemical Reaction Reveals a Unique Topology Metal–Organic Framework. *Nat. Commun.* **2015**, *6*, 6662. <https://doi.org/10.1038/ncomms7662>.
- (18) Cruz-Cabeza, A. J.; Bernstein, J. Conformational Polymorphism. *Chem. Rev.* **2014**, *114* (4), 2170–2191. <https://doi.org/10.1021/cr400249d>.
- (19) Balog, E.; Varga, G.; Kukovecz, Á.; Tóth, Á.; Horváth, D.; Lagzi, I.; Schusztter, G. Polymorph Selection of Zeolitic Imidazolate Frameworks via Kinetic and Thermodynamic Control. *Cryst. Growth Des.* **2022**, *22* (7), 4268–4276. <https://doi.org/10.1021/acs.cgd.2c00265>.
- (20) Aulakh, D.; Varghese, J. R.; Wriedt, M. The Importance of Polymorphism in Metal–Organic Framework Studies. *Inorg. Chem.* **2015**, *54* (17), 8679–8684. <https://doi.org/10.1021/acs.inorgchem.5b01311>.
- (21) Ke, Q.; Duan, Y.; Ji, Y.; Zhao, D.; Zhang, H.; Duan, C.; Li, L.; Wei, Y. Identical Composition and Distinct Performance: How ZIF-8 Polymorphs’ Structures Affect the Adsorption/Separation of Ethane and Ethene. *J. Chem. Eng. Data* **2021**, *66* (9), 3483–3492. <https://doi.org/10.1021/acs.jced.1c00322>.
- (22) Widmer, R. N.; Lampronti, G. I.; Chibani, S.; Wilson, C. W.; Anzellini, S.; Farsang, S.; Kleppe, A. K.; Casati, N. P. M.; MacLeod, S. G.; Redfern, S. A. T.; Coudert, F.-X.; Bennett, T. D. Rich Polymorphism of a Metal–Organic Framework in Pressure–Temperature Space. *J. Am. Chem. Soc.* **2019**, *141* (23), 9330–9337. <https://doi.org/10.1021/jacs.9b03234>.

- (23) Tu, M.; Kravchenko, D. E.; Xia, B.; Rubio-Giménez, V.; Wauteraerts, N.; Verbeke, R.; Vankelecom, I. F. J.; Stassin, T.; Egger, W.; Dickmann, M.; Amenitsch, H.; Ameloot, R. Template-Mediated Control over Polymorphism in the Vapor-Assisted Formation of Zeolitic Imidazolate Framework Powders and Films. *Angew. Chem.* **2021**, *133* (14), 7631–7636. <https://doi.org/10.1002/ange.202014791>.
- (24) Deacon, A.; Briquet, L.; Malankowska, M.; Massingberd-Mundy, F.; Rudić, S.; Hyde, T. I.; Cavaye, H.; Coronas, J.; Poulston, S.; Johnson, T. Understanding the ZIF-L to ZIF-8 Transformation from Fundamentals to Fully Costed Kilogram-Scale Production. *Commun. Chem.* **2022**, *5* (1), 1–10. <https://doi.org/10.1038/s42004-021-00613-z>.
- (25) Carraro, F.; Velásquez-Hernández, M. de J.; Atria, E.; Liang, W.; Twight, L.; Parise, C.; Ge, M.; Huang, Z.; Ricco, R.; Zou, X.; Villanova, L.; Kappe, C. O.; Doonan, C.; Falcaro, P. Phase Dependent Encapsulation and Release Profile of ZIF-Based Biocomposites. *Chem. Sci.* **2020**, *11* (13), 3397–3404. <https://doi.org/10.1039/C9SC05433B>.
- (26) Lyu, F.; Zhang, Y.; Zare, R. N.; Ge, J.; Liu, Z. One-Pot Synthesis of Protein-Embedded Metal–Organic Frameworks with Enhanced Biological Activities. *Nano Lett.* **2014**, *14* (10), 5761–5765. <https://doi.org/10.1021/nl5026419>.
- (27) *Database of Zeolite Structures*. <http://www.iza-structure.org/databases/>
- (28) Eddaoudi, M.; Kim, J.; Rosi, N. *Systematic Design of Pore Size and Functionality in Isorecticular MOFs and Their Application in Methane Storage*. <https://www.science.org/doi/10.1126/science.1067208> (accessed 2021-11-11).
- (29) Bertolazzo, A. A.; Dhabal, D.; Molinero, V. Polymorph Selection in Zeolite Synthesis Occurs after Nucleation. *J. Phys. Chem. Lett.* **2022**, *13* (4), 977–981. <https://doi.org/10.1021/acs.jpcclett.2c00033>.
- (30) Lo, Y.; Lam, C. H.; Chang, C.-W.; Yang, A.-C.; Kang, D.-Y. Polymorphism/Pseudopolymorphism of Metal–Organic Frameworks Composed of Zinc(II) and 2-Methylimidazole: Synthesis, Stability, and Application in Gas Storage. *RSC Adv.* **2016**, *6* (92), 89148–89156. <https://doi.org/10.1039/C6RA19437K>.
- (31) Meldrum, F. C.; O’Shaughnessy, C. Crystallization in Confinement. *Adv. Mater.* **2020**, *32* (31), 2001068. <https://doi.org/10.1002/adma.202001068>.
- (32) Stephens, C. J.; Ladden, S. F.; Meldrum, F. C.; Christenson, H. K. Amorphous Calcium Carbonate Is Stabilized in Confinement. *Adv. Funct. Mater.* **2010**, *20* (13), 2108–2115. <https://doi.org/10.1002/adfm.201000248>.
- (33) Pang, M.; Cairns, A. J.; Liu, Y.; Belmabkhout, Y.; Zeng, H. C.; Eddaoudi, M. Synthesis and Integration of Fe-Soc-MOF Cubes into Colloidosomes via a Single-Step Emulsion-Based Approach. *J. Am. Chem. Soc.* **2013**, *135* (28), 10234–10237. <https://doi.org/10.1021/ja403994u>.
- (34) Cui, J.; Gao, N.; Yin, X.; Zhang, W.; Liang, Y.; Tian, L.; Zhou, K.; Wang, S.; Li, G. Microfluidic Synthesis of Uniform Single-Crystalline MOF Microcubes with a Hierarchical Porous Structure. *Nanoscale* **2018**, *10* (19), 9192–9198. <https://doi.org/10.1039/C8NR01219A>.
- (35) Zhao, X.; Fang, X.; Wu, B.; Zheng, L.; Zheng, N. Facile Synthesis of Size-Tunable ZIF-8 Nanocrystals Using Reverse Micelles as Nanoreactors. *Sci. China Chem.* **2014**, *57* (1), 141–146. <https://doi.org/10.1007/s11426-013-5008-4>.
- (36) Kim, J.-O.; Min, K.-I.; Noh, H.; Kim, D.-H.; Park, S.-Y.; Kim, D.-P. Direct Fabrication of Free-Standing MOF Superstructures with Desired Shapes by Micro-Confined

- Interfacial Synthesis. *Angew. Chem. Int. Ed.* **2016**, *55* (25), 7116–7120. <https://doi.org/10.1002/anie.201601754>.
- (37) Huang, N.; Drake, H.; Li, J.; Pang, J.; Wang, Y.; Yuan, S.; Wang, Q.; Cai, P.; Qin, J.; Zhou, H.-C. Flexible and Hierarchical Metal–Organic Framework Composites for High-Performance Catalysis. *Angew. Chem. Int. Ed.* **2018**, *57* (29), 8916–8920. <https://doi.org/10.1002/anie.201803096>.
- (38) Silva, P.; Vilela, S. M. F.; Tomé, J. P. C.; Paz, F. A. A. Multifunctional Metal–Organic Frameworks: From Academia to Industrial Applications. *Chem. Soc. Rev.* **2015**, *44* (19), 6774–6803. <https://doi.org/10.1039/C5CS00307E>.
- (39) Julien, P. A.; Mottillo, C.; Frišćić, T. Metal–Organic Frameworks Meet Scalable and Sustainable Synthesis. *Green Chem.* **2017**, *19* (12), 2729–2747. <https://doi.org/10.1039/C7GC01078H>.
- (40) Lewis, D. J.; Zornberg, L. Z.; Carter, D. J. D.; Macfarlane, R. J. Single-Crystal Winterbottom Constructions of Nanoparticle Superlattices. *Nat. Mater.* **2020**, *19* (7), 719–724. <https://doi.org/10.1038/s41563-020-0643-6>.
- (41) Venna, S. R.; Carreon, M. A. Metal Organic Framework Membranes for Carbon Dioxide Separation. *Chem. Eng. Sci.* **2015**, *124*, 3–19. <https://doi.org/10.1016/j.ces.2014.10.007>.
- (42) Liu, S.; Xiao, W.; Jin, C.; Xia, S.; Wang, W.; Jiang, X.; Li, L.; Wang, S.; Chen, C. MOFs Derived CdS/CdO Heterojunction Photoanode for High-Efficient Water Splitting. *Appl. Surf. Sci.* **2022**, *605*, 154697. <https://doi.org/10.1016/j.apsusc.2022.154697>.
- (43) Kumar, S.; Pramudya, Y.; Müller, K.; Chandresh, A.; Dehm, S.; Heidrich, S.; Fediai, A.; Parmar, D.; Perera, D.; Rommel, M.; Heinke, L.; Wenzel, W.; Wöll, C.; Krupke, R. Sensing Molecules with Metal–Organic Framework Functionalized Graphene Transistors. *Adv. Mater.* **2021**, *33* (43), 2103316. <https://doi.org/10.1002/adma.202103316>.
- (44) Altintas, C.; Keskin, S. Molecular Simulations of MOF Membranes and Performance Predictions of MOF/Polymer Mixed Matrix Membranes for CO₂/CH₄ Separations. *ACS Sustain. Chem. Eng.* **2019**, *7* (2), 2739–2750. <https://doi.org/10.1021/acssuschemeng.8b05832>.
- (45) Horcajada, P.; Serre, C.; Grosso, D.; Boissière, C.; Perruchas, S.; Sanchez, C.; Férey, G. Colloidal Route for Preparing Optical Thin Films of Nanoporous Metal–Organic Frameworks. *Adv. Mater.* **2009**, *21* (19), 1931–1935. <https://doi.org/10.1002/adma.200801851>.
- (46) Makiura, R.; Motoyama, S.; Umemura, Y.; Yamanaka, H.; Sakata, O.; Kitagawa, H. Surface Nano-Architecture of a Metal–Organic Framework. *Nat. Mater.* **2010**, *9* (7), 565–571. <https://doi.org/10.1038/nmat2769>.
- (47) De Yoreo, J. J.; Vekilov, P. G. Principles of Crystal Nucleation and Growth. *Rev. Mineral. Geochem.* **2003**, *54* (1), 57–93. <https://doi.org/10.2113/0540057>.
- (48) Liu, J.; Wöll, C. Surface-Supported Metal–Organic Framework Thin Films: Fabrication Methods, Applications, and Challenges. *Chem. Soc. Rev.* **2017**, *46* (19), 5730–5770. <https://doi.org/10.1039/C7CS00315C>.
- (49) Lv, M.; Sun, M.; Wu, M.; Zhang, F.; Yin, H.; Sun, Y.; Liu, R.; Fan, Z.; Du, J. Tryptophan-Modulated Nanoscale Metal–Organic Framework for Coordinated Loading of Biomolecules for Cascade Production of Reactive Oxygen and Nitrogen Species. *Nano Lett.* **2022**, *22* (23), 9621–9629. <https://doi.org/10.1021/acs.nanolett.2c03778>.

- (50) Maddigan, N. K.; Tarzia, A.; Huang, D. M.; Sumbly, C. J.; Bell, S. G.; Falcaro, P.; Doonan, C. J. Protein Surface Functionalisation as a General Strategy for Facilitating Biomimetic Mineralisation of ZIF-8. *Chem. Sci.* **2018**, *9* (18), 4217–4223. <https://doi.org/10.1039/C8SC00825F>.
- (51) Shekhah, O.; Fu, L.; Sougrat, R.; Belmabkhout, Y.; Cairns, A. J.; Giannelis, E. P.; Eddaoudi, M. Successful Implementation of the Stepwise Layer-by-Layer Growth of MOF Thin Films on Confined Surfaces: Mesoporous Silica Foam as a First Case Study. *Chem. Commun.* **2012**, *48* (93), 11434–11436. <https://doi.org/10.1039/C2CC36233C>.
- (52) Liu, F.; Xu, H. Development of a Novel Polystyrene/Metal-Organic Framework-199 Electrospun Nanofiber Adsorbent for Thin Film Microextraction of Aldehydes in Human Urine. *Talanta* **2017**, *162*, 261–267. <https://doi.org/10.1016/j.talanta.2016.09.065>.
- (53) Yao, M.-S.; Tang, W.-X.; Wang, G.-E.; Nath, B.; Xu, G. MOF Thin Film-Coated Metal Oxide Nanowire Array: Significantly Improved Chemiresistor Sensor Performance. *Adv. Mater.* **2016**, *28* (26), 5229–5234. <https://doi.org/10.1002/adma.201506457>.
- (54) Liang, K.; Ricco, R.; Doherty, C. M.; Styles, M. J.; Bell, S.; Kirby, N.; Mudie, S.; Haylock, D.; Hill, A. J.; Doonan, C. J.; Falcaro, P. Biomimetic Mineralization of Metal-Organic Frameworks as Protective Coatings for Biomacromolecules. *Nat. Commun.* **2015**, *6* (1), 7240. <https://doi.org/10.1038/ncomms8240>.
- (55) Bim-Junior, O.; Alania, Y.; Tabatabaei, F. S.; Frem, R.; Bedran-Russo, A. K.; Lisboa-Filho, P. N. Biomimetic Growth of Metal–Organic Frameworks for the Stabilization of the Dentin Matrix and Control of Collagenolysis. *Langmuir* **2022**, *38* (4), 1600–1610. <https://doi.org/10.1021/acs.langmuir.1c03073>.
- (56) Li, C.; Chen, C.; Li, S.; Rasheed, T.; Huang, P.; Huang, T.; Zhang, Y.; Huang, W.; Zhou, Y. Self-Assembly and Functionalization of Alternating Copolymer Vesicles. *Polym. Chem.* **2017**, *8* (32), 4688–4695. <https://doi.org/10.1039/C7PY00908A>.
- (57) Huang, A.; Bux, H.; Steinbach, F.; Caro, J. Molecular-Sieve Membrane with Hydrogen Permselectivity: ZIF-22 in LTA Topology Prepared with 3-Aminopropyltriethoxysilane as Covalent Linker. *Angew. Chem. Int. Ed.* **2010**, *49* (29), 4958–4961. <https://doi.org/10.1002/anie.201001919>.
- (58) Kwon, H. T.; Jeong, H.-K.; Lee, A. S.; An, H. S.; Lee, J. S. Heteroepitaxially Grown Zeolitic Imidazolate Framework Membranes with Unprecedented Propylene/Propane Separation Performances. *J. Am. Chem. Soc.* **2015**, *137* (38), 12304–12311. <https://doi.org/10.1021/jacs.5b06730>.
- (59) Carpenter, B. P.; Talosig, A. R.; Mulvey, J. T.; Merham, J. G.; Esquivel, J.; Rose, B.; Ogata, A. F.; Fishman, D. A.; Patterson, J. P. Role of Molecular Modification and Protein Folding in the Nucleation and Growth of Protein–Metal–Organic Frameworks. *Chem. Mater.* **2022**, *34* (18), 8336–8344. <https://doi.org/10.1021/acs.chemmater.2c01903>.
- (60) Sudhakar, K.; Reddy, N. N.; Jayaramudu, T.; Jayaramudu, J.; Reddy, A. B.; Manjula, B.; Sadiku, E. R. Chapter 5 - Aerogels and Foamed Nanostructured Polymer Blends. In *Design and Applications of Nanostructured Polymer Blends and Nanocomposite Systems*; Thomas, S., Shanks, R., Chandrasekharakurup, S., Eds.; Micro and Nano Technologies; William Andrew Publishing: Boston, 2016; pp 75–99. <https://doi.org/10.1016/B978-0-323-39408-6.00005-4>.
- (61) Kalaj, M.; Bentz, K. C.; Ayala, S.; Palomba, J. M.; Barcus, K. S.; Katayama, Y.; Cohen, S. M. MOF-Polymer Hybrid Materials: From Simple Composites to Tailored

- Architectures. *Chem. Rev.* **2020**, *120* (16), 8267–8302. <https://doi.org/10.1021/acs.chemrev.9b00575>.
- (62) Hwang, J.; Heil, T.; Antonietti, M.; Schmidt, B. V. K. J. Morphogenesis of Metal–Organic Mesocrystals Mediated by Double Hydrophilic Block Copolymers. *J. Am. Chem. Soc.* **2018**, *140* (8), 2947–2956. <https://doi.org/10.1021/jacs.7b12633>.
- (63) Jian, M.; Liu, B.; Liu, R.; Qu, J.; Wang, H.; Zhang, X. Water-Based Synthesis of Zeolitic Imidazolate Framework-8 with High Morphology Level at Room Temperature. *RSC Adv.* **2015**, *5* (60), 48433–48441. <https://doi.org/10.1039/C5RA04033G>.
- (64) Millange, F.; Medina, M. I.; Guillou, N.; Férey, G.; Golden, K. M.; Walton, R. I. Time-Resolved In Situ Diffraction Study of the Solvothermal Crystallization of Some Prototypical Metal–Organic Frameworks. *Angew. Chem. Int. Ed.* **2010**, *49* (4), 763–766. <https://doi.org/10.1002/anie.200905627>.
- (65) Liu, L.; Zhang, D.; Zhu, Y.; Han, Y. Bulk and Local Structures of Metal–Organic Frameworks Unravelling by High-Resolution Electron Microscopy. *Commun. Chem.* **2020**, *3* (1), 1–14. <https://doi.org/10.1038/s42004-020-00361-6>.
- (66) De Yoreo, J. J.; M, S. N. A. J. Investigating Materials Formation with Liquid-Phase and Cryogenic TEM. *Nat. Rev. Mater.* **2016**, *1* (8), 1–18. <https://doi.org/10.1038/natrevmats.2016.35>.
- (67) Wiktor, C.; Meledina, M.; Turner, S.; Lebedev, O. I.; Fischer, R. A. Transmission Electron Microscopy on Metal–Organic Frameworks – a Review. *J. Mater. Chem. A* **2017**, *5* (29), 14969–14989. <https://doi.org/10.1039/C7TA00194K>.
- (68) Pham, M.-H.; Vuong, G.-T.; Fontaine, F.-G.; Do, T.-O. Rational Synthesis of Metal–Organic Framework Nanocubes and Nanosheets Using Selective Modulators and Their Morphology-Dependent Gas-Sorption Properties. *Cryst. Growth Des.* **2012**, *12* (6), 3091–3095. <https://doi.org/10.1021/cg300297p>.
- (69) Liu, L.; Chen, Z.; Wang, J.; Zhang, D.; Zhu, Y.; Ling, S.; Huang, K.-W.; Belmabkhout, Y.; Adil, K.; Zhang, Y.; Slater, B.; Eddaoudi, M.; Han, Y. Imaging Defects and Their Evolution in a Metal–Organic Framework at Sub-Unit-Cell Resolution. *Nat. Chem.* **2019**, *11* (7), 622–628. <https://doi.org/10.1038/s41557-019-0263-4>.
- (70) Hermes, S.; Schröder, F.; Amirjalayer, S.; Schmid, R.; Fischer, R. A. Loading of Porous Metal–Organic Open Frameworks with Organometallic CVD Precursors: Inclusion Compounds of the Type [LnM]a@MOF-5. *J. Mater. Chem.* **2006**, *16* (25), 2464–2472. <https://doi.org/10.1039/B603664C>.
- (71) Patterson, J. P.; Abellan, P.; Denny, M. S.; Park, C.; Browning, N. D.; Cohen, S. M.; Evans, J. E.; Gianneschi, N. C. Observing the Growth of Metal–Organic Frameworks by in Situ Liquid Cell Transmission Electron Microscopy. *J. Am. Chem. Soc.* **2015**, *137* (23), 7322–7328. <https://doi.org/10.1021/jacs.5b00817>.
- (72) Lyu, J.; Gong, X.; Lee, S.-J.; Gnanasekaran, K.; Zhang, X.; Wasson, M. C.; Wang, X.; Bai, P.; Guo, X.; Gianneschi, N. C.; Farha, O. K. Phase Transitions in Metal–Organic Frameworks Directly Monitored through In Situ Variable Temperature Liquid-Cell Transmission Electron Microscopy and In Situ X-Ray Diffraction. *J. Am. Chem. Soc.* **2020**, *142* (10), 4609–4615. <https://doi.org/10.1021/jacs.0c00542>.

Chapter 2:

Understanding the Nucleation and Growth of ZIF-8 Polymorphs

This work appears in the following publication and has been re-formatted for this thesis:

A. Rain Talosig, Fangni Wang, Justin T. Mulvey, Brooke P. Carpenter, Elisa M. Olivas, Benjamin B. Katz, Chenhui Zhu, and Joseph P. Patterson. Understanding the Nucleation and Growth of ZIF-8 Polymorphs. *Cryst. Growth Des.*, 2024, **24**, 10, 4136–4142

Chapter 2. Understanding the Nucleation and Growth of ZIF-8 Polymorphs

2.1 Introduction

Metal-organic frameworks (MOFs) are a class of nanoporous materials consisting of inorganic metal nodes that are bridged by organic linkers.^{1,2} MOFs have a wide range of applications due to their ultra-high surface area, fixed porosity, and high thermal stability.³ MOFs can exhibit polymorphism, where the MOF structure contains identical chemical composition, but varies in network topology.⁴⁻⁶ Polymorphism in MOFs can be a determining factor in function as demonstrated by the ZIF-8 system where enhanced separation of ethane and ethene is observed for more dense ZIF-8 structures such as ZIF-8_ $I\bar{4}3m$, ZIF-8_ $R3m$, and ZIF-8_ Cm .⁷

While much work has focused on the characterization of MOF polymorphs,⁸ and the synthetic factors affecting polymorph selection, the mechanisms by which different polymorphs form have largely been unexplored. This leaves a substantial knowledge gap in our understanding of MOF nucleation and growth.^{9,10} Characterizing MOF nucleation and growth is challenging due to the transient nature of the prenucleation clusters (PNCs) and amorphous phases which are commonly found in the nonclassical nucleation and growth mechanisms¹¹. Currently nucleation and growth are studied through complementary methods to understand each phase and phase transition.^{9,12-14} Microscopy allows for insight into final crystal morphology and size, while spectroscopy and diffraction allow for an understanding of ensemble information and crystallization kinetics. In a study by Filez *et al*, a molecular understanding of prenucleation clusters and crystal formation in Zeolitic imidazolate framework - 67 (ZIF-67) was unveiled using mass spectrometry, which, due to the soft analysis techniques would not deteriorate the

fragile bonds in the prenucleation clusters. Furthermore, a comprehensive understanding of the nucleation and growth mechanisms attributed to the final morphology will aid in elucidating the classical and nonclassical routes of crystal growth in MOFs. This work aims to gain an understanding of nucleation and growth of MOFs through analysis of prenucleation phases with a goal of uncovering a connection between the prenucleation stages and the final polymorph selection. Understanding this will facilitate and streamline the development of high-performance MOFs without the need for high throughput synthesis and instead utilize a thorough understanding of their structure-function relationship.¹⁵

ZIFs are a subclass of MOFs that are topologically similar to zeolites, sharing similar structures to those seen in aluminosilicate zeolite minerals.^{16,17} ZIFs are composed of tetrahedrally coordinated transition metal ions that are connected by molecular imidazolate linkers. In the case of ZIF-8, the structure is formed by the coordination of Zn^{2+} ions and 2-methylimidazole (HmIm). ZIF-8 self-assembles into two prominent morphologies: sodalite (SOD), which has a rhombic dodecahedral morphology, and diamondoid (dia), a collection of flat, stacked crystals of diamond cubic morphologies.¹² ZIF-8 SOD is the kinetic product and has a large pore size (3.4\AA) and high thermal stability and surface area (BET: $1630\text{m}^2\text{g}^{-1}$).¹⁷ ZIF-8 dia is the thermodynamic product as discovered by mechanochemical milling of ZIF-8 SOD.¹² ZIF-8 dia has the same secondary building units (SBUs) as SOD but grows into a nonporous 1D channel that has hexagonal structures that intersect with other channels to create the 3D dia topology. Although the secondary building units of these two polymorphs are identical, their topology and porosity differ and influence their functionality and biomolecule encapsulation.¹⁸ ZIF-8 has been thoroughly investigated due to its facile synthesis under aqueous conditions at

room temperature. However, the molecular origin of polymorph control in ZIF-8 is still unknown.

In this chapter, we investigate the polymorph control of ZIF-8 through variation in ligand (2-methylimidazole) to metal (zinc acetate) ratio. A combination of scanning electron microscopy (SEM) and powder X-ray diffraction (PXRD) aids in understanding the topology and morphology that is observed in ZIF-8 polymorphs. Time-resolved electrospray ionization mass spectrometry (ESI-MS) and cryogenic transmission electron microscopy (cryo-TEM) are used to understand the prenucleation cluster composition and structure prior to polymorph formation. In-situ wide angle X-ray scattering (WAXS) is used to uncover the rate of crystallization during polymorph formation.

2.2 Results

ZIF-8 Synthesis

Stock solutions of HmIm (160 mM, 700 mM and 1400 mM 1 mL) and zinc acetate (40 mM, 1 mL) were prepared with Milli-Q water. Stock solutions were used to prepare a series of MOF crystallization experiments with variation in the HmIm/Zn ratio (4:1, 17.5:1, 35:1). The solutions were combined together without mixing and aged for 24 h. The precipitate was obtained by centrifugation at 10,000 rpm for 10 min. The precipitates were washed with Milli-Q water and centrifuged three times prior to Cyro-TEM and powder PXRD analysis.

Polymorph Characterization

To characterize the polymorph formation at HmIm:Zn ratios of 4:1, 17.5:1 and 35:1, bulk analysis was carried out by PXRD of the final crystals collected by centrifugation after 24 h of reaction. ZIF-8 4:1 diffraction peaks appear around 2θ of 12.4° , 12.9° and 13.6° that relate to the

dia polymorph. 35:1 displays diffraction peaks around 2θ of 7° , 10.2° and 12.7° that relate to the simulated SOD PXRD pattern. 17.5:1 reveals that both of the PXRD patterns for SOD and dia can be observed with a slight preference for dia morphology as the SOD peaks are much less intense. SEM was used to analyze the morphology of the different polymorphs. SEM of the 4:1 ratio revealed that only the dia polymorph for ZIF-8 is defined by larger crystals, ranging in size around $3\ \mu\text{m}$ (Figure 2.1a). With an increase in ratio to 35:1 the surfaces become more faceted and represent the truncated dodecahedron structure of SOD (Figure 2.1b). The 17.5:1 ratio displays a mix of both polymorphs in equal distributions with the dia crystals being significantly larger and varying in size compared to the smaller, more uniform SOD crystals (Figure 2.1c). Intermediate ranges of HmIm:Zn ratios were compared to identify the amount of SOD and dia present in the final crystals and it was shown that the amount of SOD character increases with HmIm increase (Figure A5).

Crystal size analysis on the final crystals was performed to determine the size and polydispersity of each of these polymorphs (Figure 2.2). 35:1 contains much smaller crystals than that of dia and also has a smaller size distribution showing more uniform crystals. 17.5:1 displays smaller dia crystals that are seen in 4:1 and slightly smaller (2000nm) SOD crystals. This is consistent with previous studies that show as you increase the HmIm ratio the polydispersity decreases.¹³

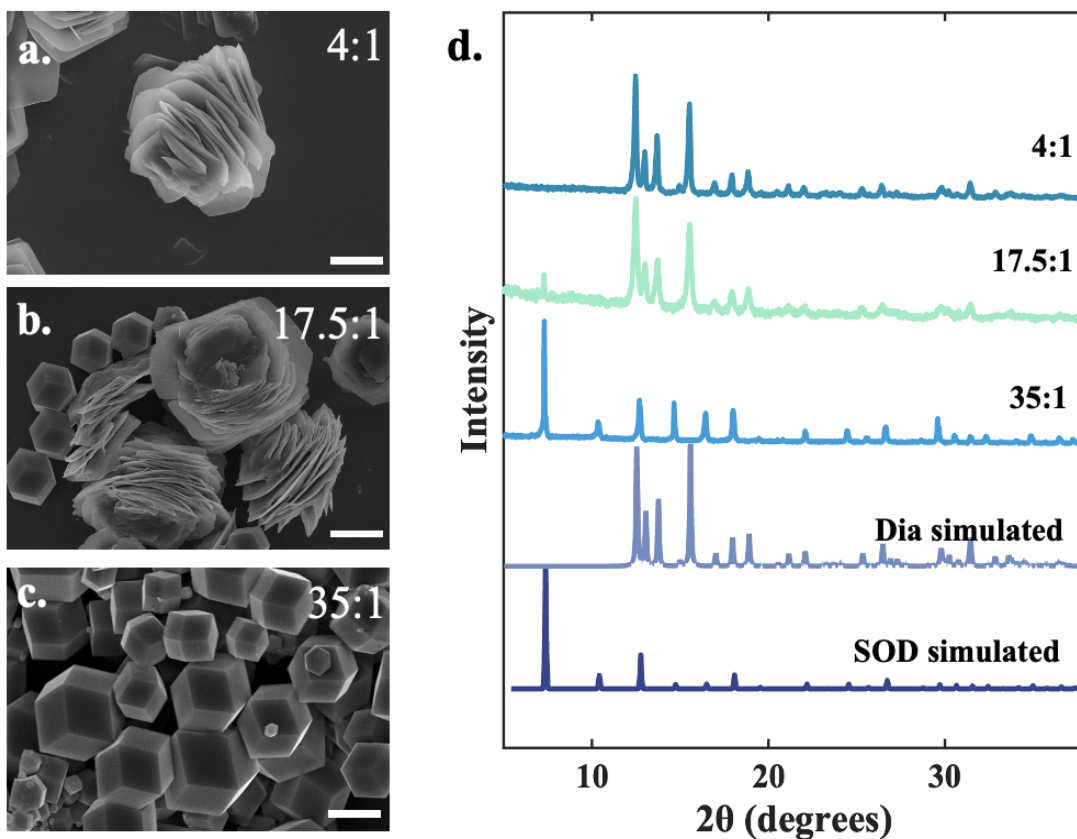


Figure 2.1 SEM of ZIF-8 (a) 4:1 (b) 17.5:1 (c) 35:1 (all scale bars are 2 μm) and (d) PXRD of ZIF-8 at HmIm:Zn ratios of 4:1, 17.5:1, 35:1 and simulated patterns for SOD and dia

HmIm:Zn (mM:mM)	Ratio HmIm:Zn	Crystal Size SOD (nm)	Crystal Size dia (nm)
80:20	4:1		5500 ± 1100
350:20	17.5:1	1700 ± 390	3500 ± 1100
700:20	35:1	2200 ± 810	

Table 2.1 Summary of crystal sizes of ZIF-8 at three different HmIm ratios (35:1, 17.5:1, 4:1).

In-situ X-ray Scattering

In-situ WAXS was utilized to understand the time-resolved crystallization kinetics of ZIF-8. To gain information about the rate of crystallinity experiments were performed using an in-house X-ray source, monitoring $6.5 - 7.5^\circ 2\theta$ every 10 minutes for 24 h. Following measurements, the data was normalized against the background, and the integrated intensity was plotted to determine the extent of crystallization (Figure 2.2a). The ZIF-8 solutions were prepared by mixing HmIm and Zn precursors at 35:1 and 4:1 ratios and immediately placed into 1 mm special glass capillaries. We define $t = 0$ as the time of mixing and the first collected data point is 10 minutes. 35:1 ZIF-8 reaches full extent of crystallization at around 3 h. 4:1 ZIF-8 takes around 8 h to begin to plateau in crystallinity and does not completely flatten by the end of the collection time around 12 h. In-house X-ray sources were ideal for long collection times, but the time resolution and collection angle were limited by the intensity of the X-ray source. To achieve a higher temporal resolution, synchrotron-based in-situ WAXS was utilized to collect the entire spectrum of $5-40^\circ 2\theta$ in 1 second.

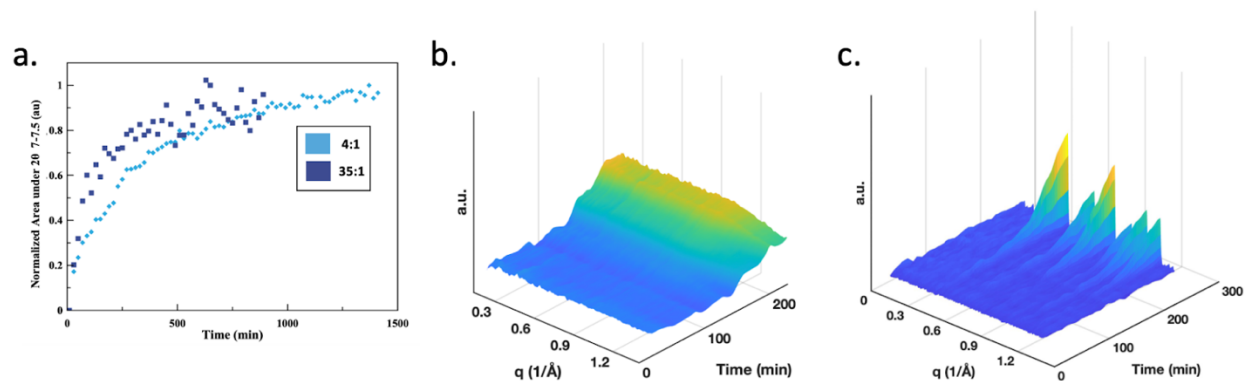


Figure 2.2 (a) Plot of the normalized area under 2θ 7-7.5 versus time produced by the integrated intensity of the (211) reflections collected by time-resolved in situ XRD. Time-resolved wide-angle x-ray scattering patterns of ZIF-8 (b) 4:1 and (c) 35:1 for the first 250 min. Background subtraction was performed for c) using an in-house MATLAB script, see SI for details.

In-situ WAXS experiments were performed on the 7.3.3 beamline of the Advanced Light Source at Lawrence Berkeley National Laboratory (Berkeley, CA). The ZIF-8 reaction was initiated through mixing precursor solutions in a glass vial, and the solutions were immediately added to a 1 mm quartz capillary. The capillary was then mounted into the instrument over the course of 5 min. The data collection began once the sample was mounted. We define $t = 0$ as the time of mixing and the first data was collected at $t = 10$ minutes. Figure 2.2b and 2.2c show the WAXS plots of HmIm:Zn ratios of 4:1 and 35:1 respectively over the reaction time of 4 h. The peaks that are present in 35:1 after 150 min are related to the lattice for ZIF-8 SOD. The spectrum for 4:1 does not show any significant peaks but an increase in overall intensity after the 4 h collection period. This is not consistent with the in-house collected WAXS which shows an increase in intensity of the $6.5 - 7.5^\circ 2\theta$. This could be due to the lack of range in which the in-house WAXS could collect in comparison to the synchrotron based WAXS, and therefore could include some of the formation of amorphous phases which can cause an increase in intensity.

This wider range data allows us to understand that in the first 4 h, significant nucleation occurs in the 35:1 system but not in the 4:1 system.

Mass Spectroscopy

To gain a better understanding of the species present during the initial stage of nucleation under different precursor conditions, the relative abundance of different Zn clusters was determined from time-resolved ESI-MS. This methodology was adapted from previous work which studied the evolution of Zn clusters for understanding the nucleation and growth of ZIF-67.¹¹

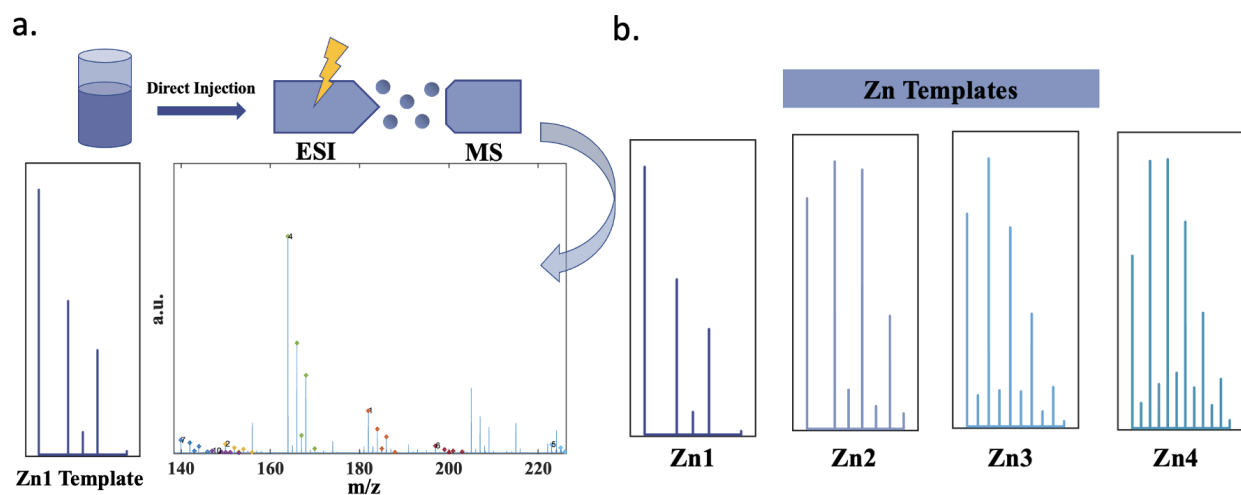


Figure 2.3 (a) ESI source where a dilute solution of ZIF-8 is injected, electrosprayed, and projected toward the MS inlet, yielding relative abundance versus mass/charge. Automated peak analysis shows the intensity of n Zn oligomers with size $n = 1-4$ (b) Zn fragmentation patterns of n Zn oligomers with size $n = 1-4$.

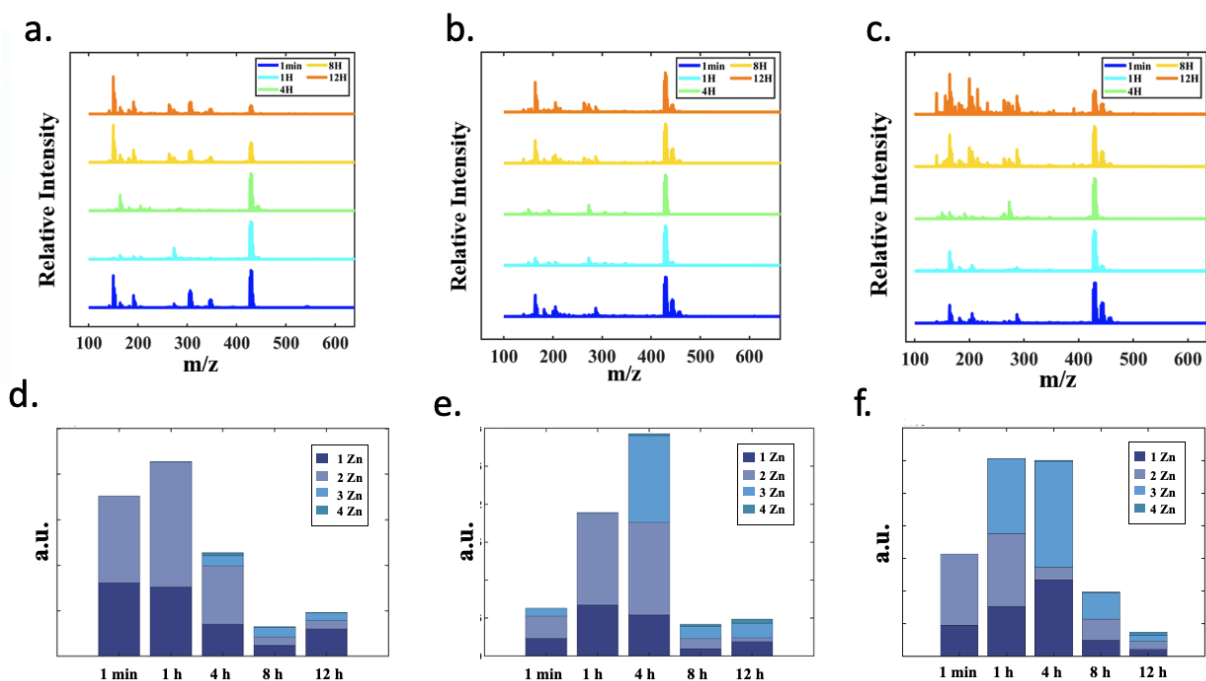


Figure 2.4 Stacked ESI-MS plots of ZIF-8 at times 1 min, 1H, 4H, 8H, 12H at Zn: HmIm ratio of (a) 4:1 (b) 17.5:1 (c)35:1. Sum of peaks of Zn oligomer size for Zn:HmIm ratios of (d) 4:1 (e) 17.5:1 (f)35:1.

The ESI-MS data was analyzed using an in-house MATLAB script developed to automatically identify characteristic PNC fragmentation patterns in the data based on simulated fragmentation patterns of Zn in solution (Figure 2.3b). $n\text{Zn}$ fragments were simulated from $n=1-4$ which displayed distinct isotope patterns. Zn clusters larger than 4Zn were difficult to distinguish so the analysis is capped at 4Zn . The maximum peaks from each characteristic fragmentation pattern were integrated and summed to determine the total amount of PNC present in each ESI-MS dataset (Figure 2.3). The crystallization solutions were mixed for 5 times points running from 1 min to 12 h and at the desired reaction time, diluted by 100x to stop reaction as well as prepare the solution for mass spectroscopy appropriate concentrations (Figure 2.4a-c). Time points after 12 h were not collected due to a decrease in signal observed after 12 h as the

clusters moved from prenucleation to bulk crystal phases.¹¹ As ZIF-8 crystallizes, the precipitates crash out of solution and sink towards the bottom of the reaction vial, to ensure that a majority of the sample is the prenucleation clusters and not the bulk phases, the samples are taken from the top of the reaction vessel.

After the Zn clusters were assigned, the sum of each Zn cluster intensity was calculated at each sampling interval to show the change in Zn cluster composition as the reaction progressed (Figure 2.4d-f). The 4:1 ratio showed exclusively 1Zn and 2Zn clusters at 1 h and predominantly 1Zn and 2Zn clusters at 4 h with only 10% of the clusters represented by 3Zn and 4Zn respectively (Figure 2.4d). In comparison, 35:1 showed the development of 3Zn as soon as 1 h into the reaction and the majority of the solution consists of 3Zn at 4 h (Figure 2.4f). At the 8h time point the abundance of Zn clusters decreases to less than the initial abundances indicating that the majority of Zn PNCs are no longer present in the solution and have crystallized into ZIF-8 SOD. This continues to 12 h where there is half of the abundance of Zn clusters observed in 8 h. The 17.5:1 system indicates an intermediate between the 4:1 and 35:1 with 2Zn not appearing in large abundances until 4 h, but still showing a large decrease in Zn clusters around 8 h indicating that many of the Zn clusters have left the pre-nucleation phase (Figure 2.4e). This is supported by the WAXS data that shows an increase in crystallinity as the prenucleation cluster concentration decreases (Figure 2.2). Precautions were taken to ensure that little of the bulk crystal was sampled, but it is possible that the solution sampled contains some larger Zn clusters that have fragmented. Although there may be a mixture of prenucleation species and fragmented species in the sample, there is a clear trend in the concentration of Zn clusters that demonstrates the presence of prenucleation clusters.

Cryo-TEM

Cryo-TEM was used to compare the structure of the amorphous precursor particles at 1 h of reaction time. 4:1 (Figure 2.5a) shows < 100 nm spherical particles that appear to be stable to aggregation. 17.5 (Figure 2.5b) shows smaller particles but they appear to be highly aggregated. Although 17.5:1 at 1 h of reaction shows aggregation, based on the spherical morphology and our previous data on ZIF-8, we interpret these to be amorphous particles. Crystallinity of ZIF-8 at early time points was showcased in a previous publication from our lab.¹³ This work shows crystallinity of 35:1 at the 1 min time point through diffraction patterns and faceted crystals. The cryo-TEM images for 17.5:1 appear to be similar to previous studies of aggregation that did not display crystallinity.

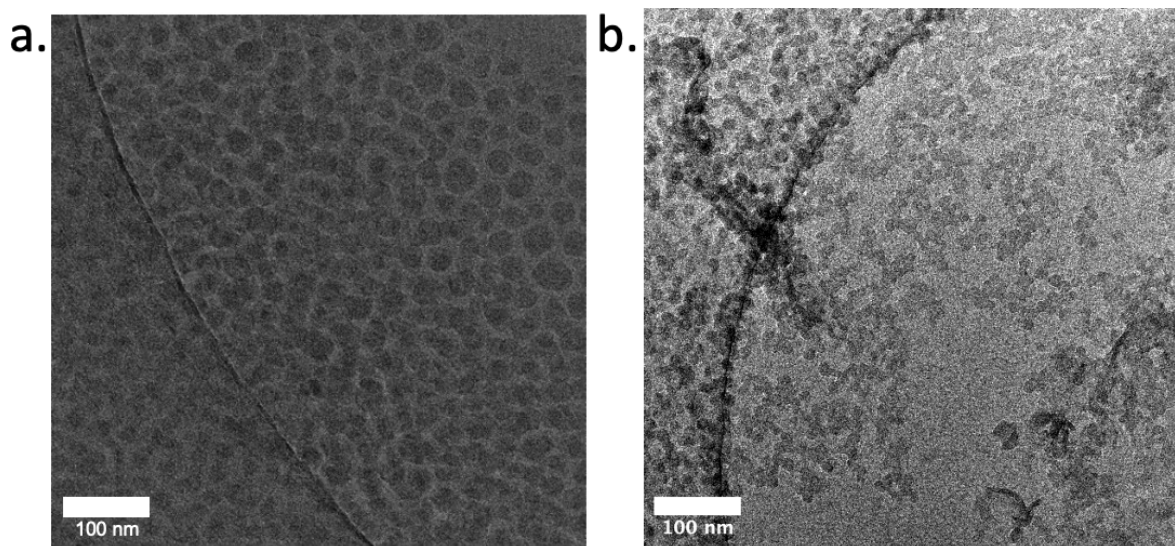


Figure 2.5 Representative Cryo-TEM images of nucleation and growth at 1 h of ZIF-8 in water. Scale bars are 100 nm. ZIF-8 with precursor ratios of (a) 4:1 (b) 17.5:1

2.3 Discussion

The collective data shows that the formation of ZIF-8 SOD and dia occurs via the formation of prenucleation clusters which aggregate into spherical amorphous particles. SOD crystallization occurs more rapidly than dia as supported by the in-situ x-ray studies. The formation of SOD occurs through the rapid aggregation of particles (cryo-TEM) which results in the formation of 3Zn clusters (ESI-MS). In contrast, the formation of dia occurs via the formation of particles that are more stable to aggregation (Cryo-TEM) and results in the formation of 2Zn clusters (ESI-MS). This would indicate that the rate-determining steps in the nucleation of dia and SOD occur through the reaction of the 2Zn and 3Zn clusters respectively. This reaction could be through the addition of another Zn or through the aggregation of the 2Zn and 3Zn clusters (Figure A6). The main difference between the dia and SOD synthesis is that for the latter there is a much greater concentration of ligand. The excess ligand appears to be responsible for the rapid formation of 3Zn clusters and the rapid aggregation of amorphous particles, both of which lead to nucleation of the SOD polymorph. Specifically, how the excess ligand is controlling these phenomena remains an open question requiring further investigation.

2.4 Conclusions

This study of the early stages of nucleation and growth demonstrates the importance of studying the PNCs of ZIF-8 to understand polymorph control. The main challenge that we address in this study is a molecular understanding of the PNCs and their role in the final polymorph formation. To address this challenge, we utilized complementary methods to study the formation of ZIF-8 through the stages of nucleation and growth and the combination of these techniques allowed for

a more complete picture understanding of polymorph control in ZIF-8 systems. The combined data revealed that SOD nucleates rapidly via the formation and aggregation of amorphous particles which contain a significant amount of 3Zn clusters whereas dia nucleates more slowly via the formation of stable amorphous particles which are composed of 2Zn clusters.

2.5 Methods

Materials. All chemical reagents used for ZIF-8 were obtained from Sigma Aldrich and were used without further purification unless stated otherwise. Stock solutions of bovine serum albumin, β -cyclodextrin, 2-methylimidazole (HmIm), and zinc acetate (Zn) were made using Milli-Q water (18MW). Glass capillaries were obtained from Hampton Research.

ZIF-8 Synthesis

Stock solutions of 2-methylimidazole (HmIm) (1400 mM, 700 mM, and 160mM, 1 mL) and zinc acetate (Zn) (40 mM, 1 mL) were prepared in water ($\rho > 18 \text{ M}\Omega \text{ cm}$). Stock solutions were then used to prepare a series of crystallization experiments with variation in the HmIm:Zn ratio (35:1, 17.5:1, 4:1) Zinc acetate solution was added to 2-methylimidazole solutions and crystallization was initiated. The solutions were aged for 24 h at room temperature without stirring and the precipitate was obtained via centrifugation at 10,000 rpm for 10 min. The precipitate was washed by water and centrifuged twice more and a final rinse with methanol.

SEM: Samples were prepared by pipetting 10uL of diluted MOF sample onto 1mm thick glass slides which were then coated with 5 nm Iridium (Quorum Q150T) to reduce charging. Samples were imaged with Magellan 400 XRH system with secondary electron images taken at an accelerating current ranging from 2-3 keV.

Cryo-TEM. Cryo-TEM samples were prepared using a Quantifoil R2/2 Holey Carbon Films from Electron Microscopy Sciences or 400 Mesh Carbon grids from TedPella. Prior to sample application, glow discharge was applied to the grids for 70 s. Reaction solutions at various time points were centrifuged for ~ 2 s, and 3 μL of each sample was taken from the reaction solutions and underwent vitrification using an Automatic Plunge Freezer ME GP2 (Leica Microsystems). Vitrification was performed at a $\sim 95\%$ humidity with a blot time of 4 s, and samples were plunged into liquid propane. Samples were then analyzed using a JOEL-2100 TEM with a Schottky field-type emission gun set to 200 kV. Images were obtained using Digital Micrograph software or a Gatan OneView Camera.

PXRD. After removing all liquid from the top of centrifuged crystal precipitates and allowing samples to air dry, a Rigaku SmartLab X-ray diffractometer was used to obtain PXRD pattern at 40 kV and 30 mA. Results were plotted with background subtraction using IGOR software.

In-situ WAXS (UCI IMRI). MOF samples were prepared and immediately after mixing were loaded into 1mm special glass capillaries. All measurements were performed on a Rigaku SmartLab X-ray diffractometer was used to obtain a PXRD pattern at 40 kV and 30 mA scanning from 2θ 6.5-7.5°. Results were plotted and analyzed in Matlab using an in-house script.

In-situ WAXS (LBNL ALS). WAXS samples were prepared in 2mL quantities as described in the ZIF-8 synthesis and immediately after mixing the solutions were added to 2 mm in diameter special glass capillaries (10 micron wall thickness) and mounted onto a custom built sample holder. The solutions were mounted horizontally to ensure the entire width of the capillary was being sampled. In-situ wide X-ray scattering (WAXS) data was collected at the SAXSWAXS beamline (7.3.3) at the Advanced Light Source (ALS), Lawrence Berkeley National Laboratory, using a photon energy of 10 keV (wavelength = 1.24 Å). Measurements took place in ambient

temperatures. Data was collected by a Dectris Pilatus 2M detector with a pixel size of 0.172×0.172 mm and 1475×1679 pixels was used to capture the 2D scattering patterns at a distance of 300 mm from the sample. A silver behenate standard was used as a calibrant. Data was analyzed using the Nika package for Igor Pro.¹⁹ Background subtraction was performed via an in-house MATLAB script (see SI for details).

ESI-MS. Spectra were recorded on Xevo G2-XS QToF (Waters Corporation, Massachusetts, U.S) in positive ion mode. ZIF-8 solutions were mixed to make various HmIm:Zn ratios and were diluted 100x to reach MS appropriate concentrations at time points of 1 min, 1h, 4h, 8h, 12h. Samples were electrosprayed using a syringe pump at a flow of 0.1 mL/min coupled to an ion max source set to 3.5kV spray voltage. A mass range of 100-2000 m/z was used.²⁰ After each sample a reference of pure water was collected for data correction. An in-house MATLAB script was developed to identify characteristic PNC fragmentation patterns based on simulated fragmentation patterns. Each simulated fragmentation pattern was analyzed individually. The script first identified all possible peak combinations which had the characteristic spacing found in the simulated data within an error of 0.01 m/z. For each valid peak combination, the “goodness of match” was determined by calculating the mean squared error between the normalized peak heights of the valid peak combination with the normalized peak heights of the simulated fragmentation pattern. The top matches were manually checked, and any anomalous matches were removed from the analysis allowing preference for higher ranking matches.

2.6 Acknowledgements

This chapter was primarily supported by the National Science Foundation CBET Award #2102033. The authors acknowledge the use of facilities and instrumentation at the UC Irvine Materials Research Institute (IMRI), which was supported in part by the National Science Foundation through the UC Irvine Materials Research Science and Engineering Center (DMR-2011967). The use of BioPACIFIC SAXS instrument was supported by the BioPACIFIC Materials Innovation Platform of the National Science Foundation under Award No. DMR-1933487.

We wish to thank the UCI Mass Spectrometry Facility and Ben Katz for assistance with collection and analyses of protein mass spectrometry data. Data were collected on a Waters Acquity UPLC Xevo G2-XS QTOF system (NIH supplemental funding support received by: J.S. Nowick (NIGMS GM097562), Vy Y. Duong (NIH GM105938) and O. Cinquin (NIGMS GM102635). Data were analyzed with Waters MassLynx v.4.1 and MATLAB.

This research used beamline 7.3.3 of the Advanced Light Source, which is a DOE Office of Science User Facility under contract no. DE-AC02-05CH11231.

2.7 References

- (1) Bertolazzo, A. A.; Dhabal, D.; Molinero, V. Polymorph Selection in Zeolite Synthesis Occurs after Nucleation. *J. Phys. Chem. Lett.* **2022**, *13* (4), 977–981. <https://doi.org/10.1021/acs.jpcclett.2c00033>
- (2) Zhou, H.C.; Long, J. R.; Yaghi, O. *Chem. Rev.* **2012**, *112*, 2, 673–674 <https://doi.org/10.1021/cr300014x>
- (3) Furukawa, H.; Cordova, K. E. The Chemistry and Applications of Metal-Organic Frameworks. *Science* **2013**, *341*, 1230444. <https://doi.org/10.1126/science.1230444>
- (4) Matemb Ma Ntep, T. J.; Wahiduzzaman, M.; Laurenz, E.; Cornu, I.; Mouchaham, G.; Dovgaliuk, I.; Nandi, S.; Knop, K.; Jansen, C.; Nouar, F.; Florian, P.; Földner, G.; Maurin,

- G.; Janiak, C.; Serre, C. When Polymorphism in Metal–Organic Frameworks Enables Water Sorption Profile Tunability for Enhancing Heat Allocation and Water Harvesting Performance. *Adv. Mater.* **2023**, 2211302. <https://doi.org/10.1002/adma.202211302>
- (5) Karadeniz, B.; Žilić, D.; Huskić, I.; Germann, L. S.; Fidelli, A. M.; Muratović, S.; Lončarić, I.; Etter, M.; Dinnebier, R. E.; Barišić, D.; Cindro, N.; Islamoglu, T.; Farha, O. K.; Friščić, T.; Užarević, K. Controlling the Polymorphism and Topology Transformation in Porphyrinic Zirconium Metal–Organic Frameworks via Mechanochemistry. *J. Am. Chem. Soc.* **2019**, *141* (49), 19214–19220. <https://doi.org/10.1021/jacs.9b10251>
- (6) Aulakh, D.; Varghese, J. R.; Wriedt, M. The Importance of Polymorphism in Metal–Organic Framework Studies. *Inorg. Chem.* **2015**, *54* (17), 8679–8684. <https://doi.org/10.1021/acs.inorgchem.5b01311>
- (7) Ke, Q.; Duan, Y.; Ji, Y.; Zhao, D.; Zhang, H.; Duan, C.; Li, L.; Wei, Y. Identical Composition and Distinct Performance: How ZIF-8 Polymorphs’ Structures Affect the Adsorption/Separation of Ethane and Ethene. *J. Chem. Eng. Data* **2021**, *66* (9), 3483–3492. <https://doi.org/10.1021/acs.jced.1c00322>
- (8) Widmer, R. N.; Lampronti, G. I.; Chibani, S.; Wilson, C. W.; Anzellini, S.; Farsang, S.; Kleppe, A. K.; Casati, N. P. M.; MacLeod, S. G.; Redfern, S. A. T.; Coudert, F.-X.; Bennett, T. D. Rich Polymorphism of a Metal–Organic Framework in Pressure–Temperature Space. *J. Am. Chem. Soc.* **2019**, *141* (23), 9330–9337. <https://doi.org/10.1021/jacs.9b03234>
- (9) Carpenter, B. P.; Talosig, A. R.; Rose, B.; Palma, G. D.; Patterson, J. P. Understanding and Controlling the Nucleation and Growth of Metal–Organic Frameworks. *Chem. Soc. Rev.* **2023**, *52* (20), 6918–6937. <https://doi.org/10.1039/D3CS00312D>
- (10) Van Vleet, M. J.; Weng, T.; Li, X.; Schmidt, J. R. In Situ, Time-Resolved, and Mechanistic Studies of Metal–Organic Framework Nucleation and Growth. *Chem. Rev.* **2018**, *118* (7), 3681–3721. <https://doi.org/10.1021/acs.chemrev.7b00582>
- (11) Filez, M.; Caratelli, C.; Rivera-Torrente, M.; Muniz-Miranda, F.; Hoek, M.; Altelaar, M.; Heck, A. J. R.; Van Speybroeck, V.; Weckhuysen, B. M. Elucidation of the Pre-Nucleation Phase Directing Metal-Organic Framework Formation. *Cell Rep. Phys. Sci.* **2021**, *2* (12), 100680. <https://doi.org/10.1016/j.xcrp.2021.100680>
- (12) Katsenis, A. D.; Puškarić, A.; Štrukil, V.; Mottillo, C.; Julien, P. A.; Užarević, K.; Pham, M.-H.; Do, T.-O.; Kimber, S. A. J.; Lazić, P.; Magdysyuk, O.; Dinnebier, R. E.; Halasz, I.; Friščić, T. In Situ X-Ray Diffraction Monitoring of a Mechanochemical Reaction Reveals a Unique Topology Metal-Organic Framework. *Nat. Commun.* **2015**, *6*, 6662. <https://doi.org/10.1038/ncomms7662>
- (13) Ogata, A.; Rakowski, A.; Carpenter, B.; Fishman, D. Direct Observation of Amorphous Precursor Phases in the Nucleation of Protein–Metal–Organic Frameworks *J. Am. Chem. Soc.* **2020**, *142*, 3, 1433–1442. <https://doi.org/10.1021/jacs.9b11371>
- (14) Cravillon, J.; Schröder, C.A.; Nayuk, R.; Gummel, J.; Huber, K.; Wiebcke, M. Fast Nucleation and Growth of ZIF-8 Nanocrystals Monitored by Time-Resolved In Situ Small-Angle and Wide-Angle X-Ray Scattering. *Angew. Chem.* **2011**, *50*, 8067–8071. <https://doi.org/10.1002/anie.201102071>
- (15) Yoreo, J. J. D.; Gilbert, P. U. P. A.; Sommerdijk, N. A. J. M.; Penn, R. L.; Whitlam, S.; Joester, D.; Zhang, H.; Rimer, J. D.; Navrotsky, A.; Banfield, J. F.; Wallace, A. F.; Michel, F. M.; Meldrum, F. C.; Cölfen, H.; Dove, P. M. Crystallization by Particle Attachment in

- Synthetic, Biogenic, and Geologic Environments. *Science* **2015**, *349* (6247).
<https://doi.org/10.1126/science.aaa6760>
- (16) Chen, B.; Yang, Z.; Zhu, Y.; Xia, Y. Zeolitic Imidazolate Framework Materials: Recent Progress in Synthesis and Applications. *J. Mater. Chem. A* **2014**, *2* (40), 16811–16831.
<https://doi.org/10.1039/C4TA02984D>
- (17) Park, K. S.; Ni, Z.; Côté, A. P.; Choi, J. Y.; Huang, R.; Uribe-Romo, F. J.; Chae, H. K.; O’Keeffe, M.; Yaghi, O. M. Exceptional Chemical and Thermal Stability of Zeolitic Imidazolate Frameworks. *Proc. Natl. Acad. Sci.* **2006**, *103* (27), 10186–10191.
<https://doi.org/10.1073/pnas.060243910>
- (18) Carpenter, B. P.; Talosig, A. R.; Mulvey, J. T.; Merham, J.; Patterson, J. P. The Role of Molecular Modification and Protein Folding in the Nucleation and Growth of Protein-Metal-Organic Frameworks. *Chem. Mater.* **2022**, *34*, 18, 8336–8344
<https://doi.org/10.1021/acs.chemmater.2c01903>
- (19) Ilavsky, J. Nika: Software for Two-Dimensional Data Reduction. *J. Appl. Crystallogr.* **2012**, *45* (2), 324–328.
- (20) Rosnes, M. H.; Mathieson, J. S.; Törnroos, K. W.; Johnsen, R. E.; Cronin, L.; Dietzel, P. D. C. Electrospray Mass Spectrometry Investigation into the Formation of CPO-27. *Cryst. Growth Des.* **2019**, *19* (4), 2089–2096. <https://doi.org/10.1021/acs.cgd.8b01657>

Appendix A:
Supplementary Information for Chapter 2

Appendix A: Supplementary Information for Chapter 2

A.1 ESI-MS Analysis

ESI-MS analysis of ZIF-8 was analyzed using simulated isotope patterns for 1-4Zn species (A1).

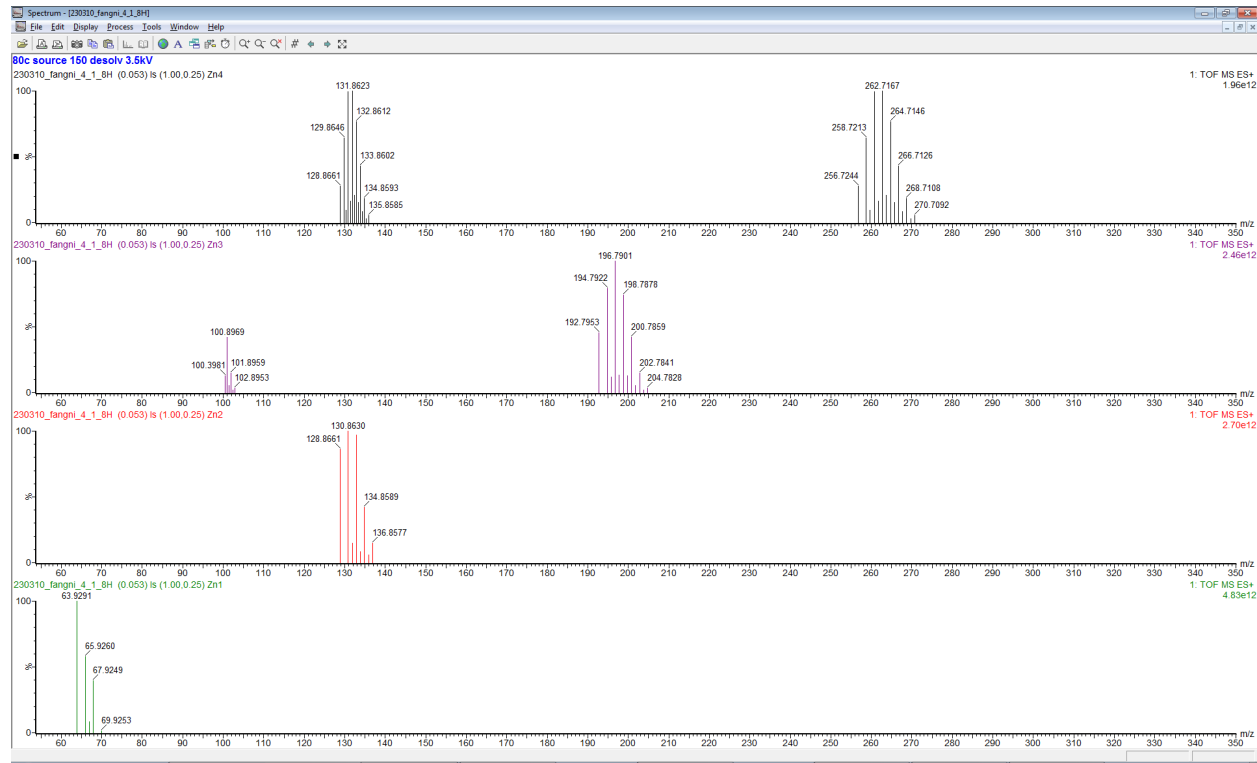


Figure A1. Simulated data for Zn isotope patterns for 1-4Zn species. Isotope patterns were used with in-house MATLAB script to determine the presence of Zn species.

A.2 WAXS analysis of ZIF-8

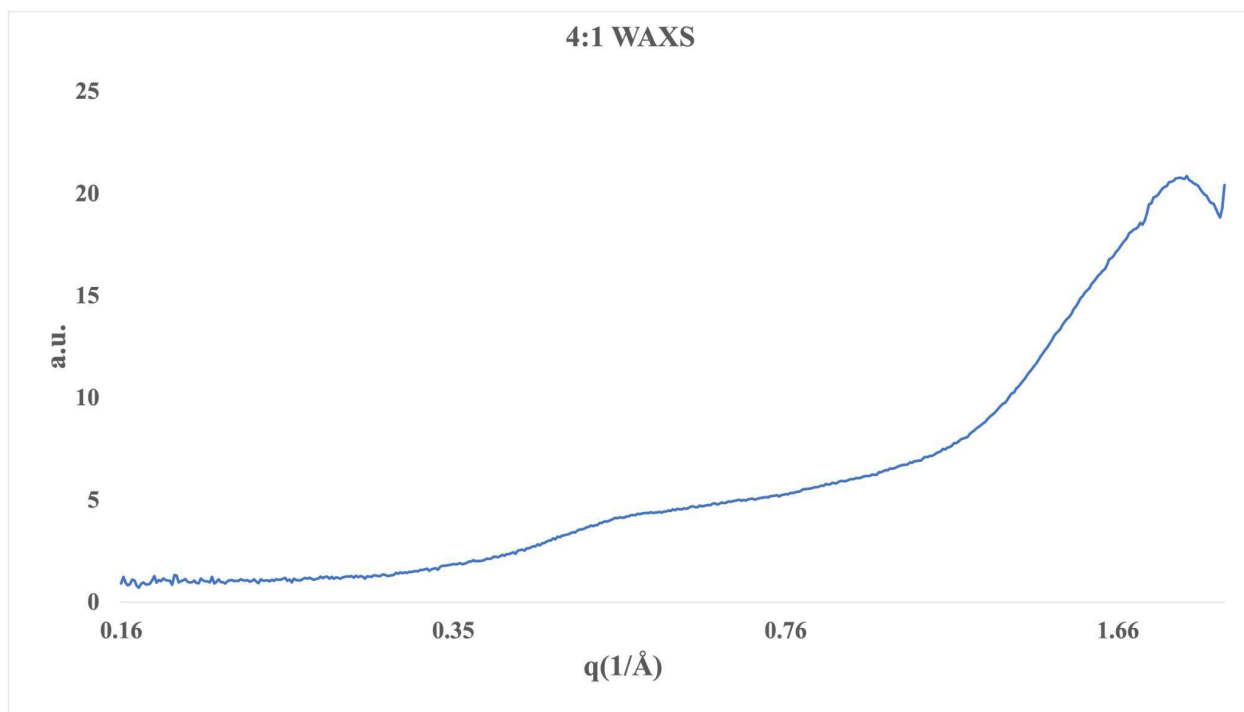


Figure A2: WAXS of 4:1 ZIF-8 collected after 12 hours in solution

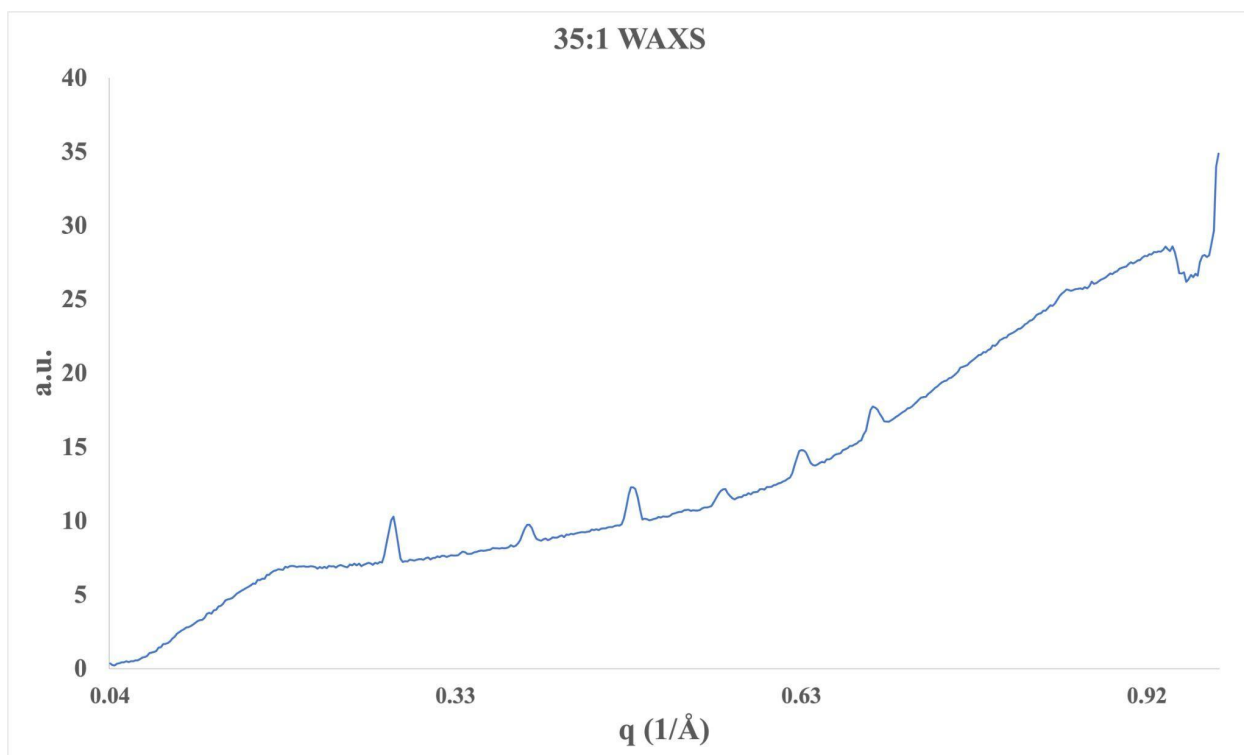


Figure A3: WAXS of 35:1 ZIF-8 collected after 12 hours in solution.

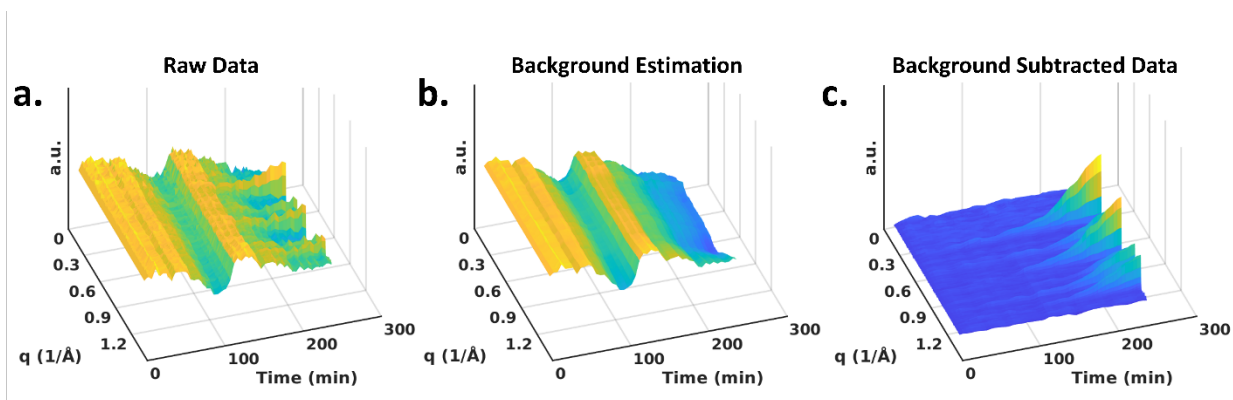


Figure A4: Background subtraction performed on time resolved WAXS data of ZIF-8 35:1 (Figure 4c). a) Raw data. b) Background estimation was performed by applying 2 sequential, orthogonal 1D Gaussian blurs to the 2D raw data. The first 1D Gaussian filter was applied to the q domain, with a first standard deviation of 5 datapoints (0.012 1/ \AA). The second 1D Gaussian filter was applied to the time domain, with a first standard deviation of 0.5 datapoints (2.5 seconds). The resulting 2D background is displayed above. c) Background subtraction was performed by dividing the raw data by the background estimation.

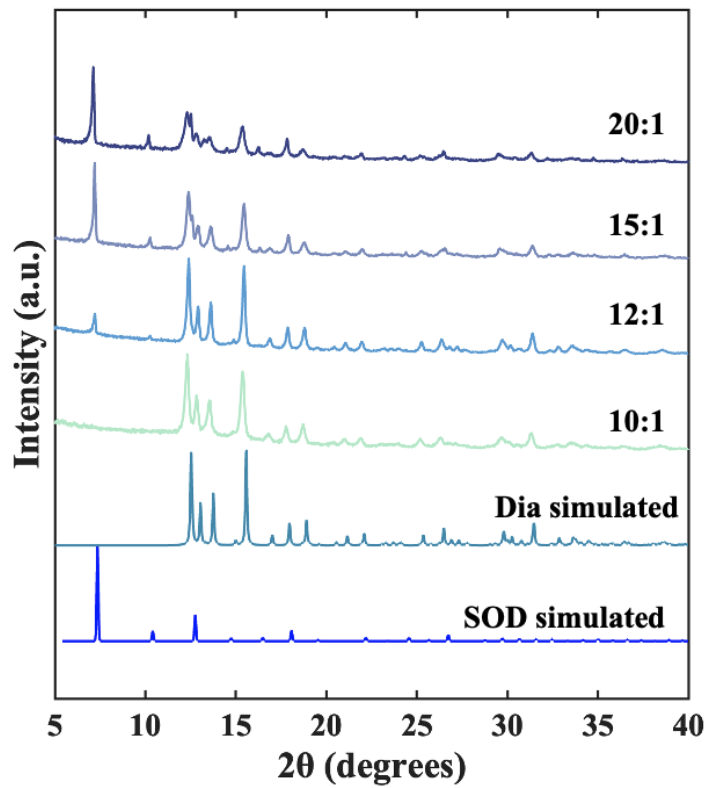


Figure A5. PXRD of ZIF-8 at HmIm:Zn ratios of 10:1, 12:1, 15:1, 20:1 and simulated patterns for SOD and dia

A.3 ESI-MS Cluster Analysis

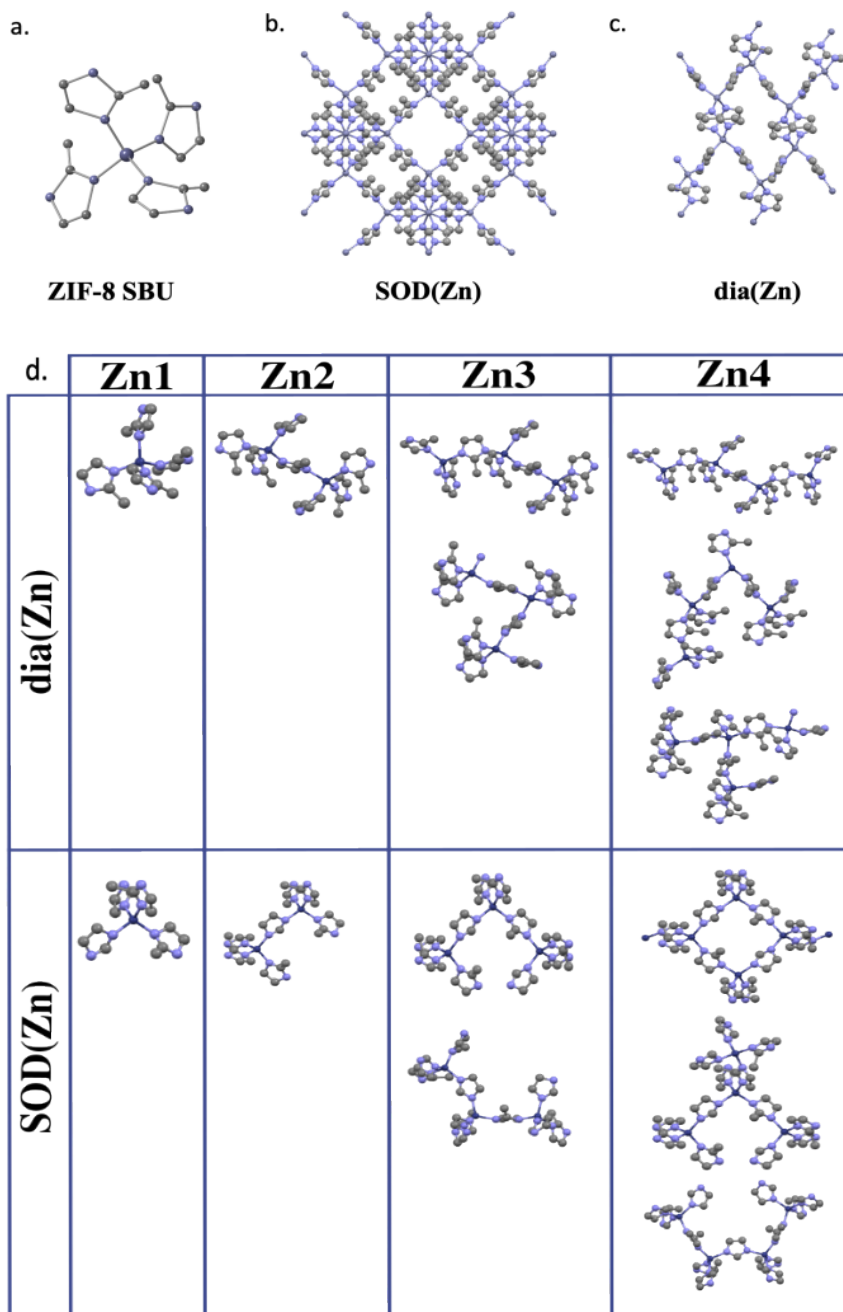


Figure A6: Crystal structures of ZIF-8 as (a) secondary building unit of one Zn tetrahedrally coordinated to four HmIm linkers (b) porous ZIF-8 SOD structure and (c) ZIF-8 dia. (d) Structures of 1-4 Zn clusters for SOD and dia. Crystal Structures of ZIF-8 SOD and dia were obtained from

previously solved structures¹ and atoms were removed until appropriate sizes of the molecular clusters were reached based on the amount of Zn present.

A.4 Crystal Size Analysis

SEM was used to determine crystal diameter by averaging the length of ~50-100 crystals per sample using Fiji, ImageJ (Figure A7). From the analysis, crystal sizes were averaged and the standard deviation was calculated.

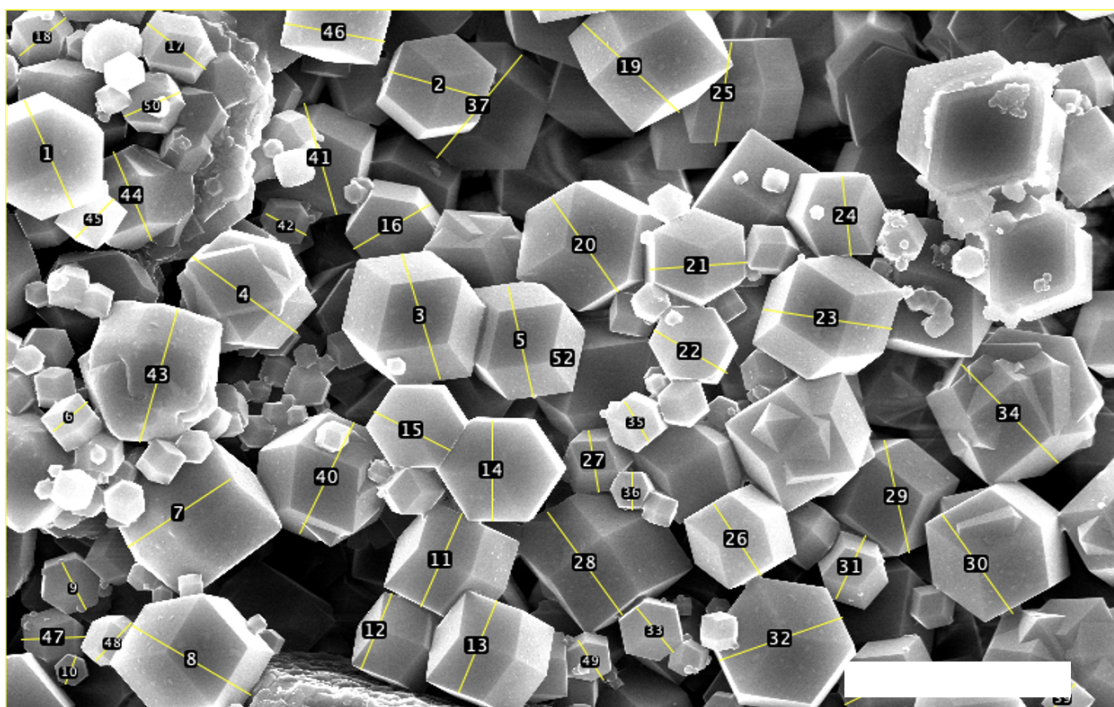


Figure A7: SEM image (scale bar 10 μm) of ZIF-8 at 35:1 (HmIm:Zn) at $t = 24\text{h}$. Numbered yellow lines indicate the diameter of the crystal measured using Fiji, ImageJ.

A.5 References

- (1) Karagiari, O.; Lalonde, M. B.; Bury, W.; Sarjeant, A. A.; Farha, O. K.; Hupp, J. T. Opening ZIF-8: A Catalytically Active Zeolitic Imidazolate Framework of Sodalite Topology with Unsubstituted Linkers. *J. Am. Chem. Soc.* **2012**, *134* (45), 18790–18796.

- (2) Shi, Q.; Chen, Z.; Song, Z.; Li, J.; Dong, J. Synthesis of ZIF-8 and ZIF-67 by Steam-Assisted Conversion and an Investigation of Their Tribological Behaviors. *Angew. Chem. Int. Ed.* **2011**, *50* (3), 672–675.

Chapter 3:
**Confinement Effects on the Nucleation and
Growth of ZIF-8**

Chapter 3: Confinement Effects on the Nucleation and Growth of ZIF-8

3.1 Introduction

Confinement effects on metal-organic framework (MOF) nucleation and growth have not been well explored, however, there have been examples of nanoscopic confinement in MOF synthesis. In this work, confinement does not apply to the incorporation of nanoparticles¹ or biomolecules² but instead refers to the reaction volume size and volume confinement.^{3,4} Nanoscopic confinement influences, defined as confinement on a nanometer scale, are observed in restricted volumes and can limit crystal growth in the x,y, and/or z dimensions and have been shown to stabilize metastable products and phases for non-MOF systems.³⁻⁵ Specifically, this has been observed in calcium carbonate systems where amorphous phases were stabilized by increasing the degree of confinement.⁶ Stabilization of metastable phases occurs due to the increasing energy barrier for thermodynamic products. The degree of confinement can also affect growth, where the surface area of the synthesis vessel can play a role in determining the growth rate. Macroscale confinement has been demonstrated in the self-assembly and growth of cellulose nanocrystals, and with an increase in confinement there is a loss of long-range order in the growth of the nanocrystals.⁷ Confinement methods have been used to synthesize MOF nanoparticles with high uniformity and low size distribution using interfaces such as colloforms⁸ and droplets.⁹ Directional confinement has also been used to template the growth direction of MOF crystals by restricting growth in various orientations.^{10,11}

In-situ techniques, such as wide angle x-ray scattering (WAXS) and small-angle x-ray scattering (SAXS) have been used to study MOF nucleation and growth to understand the crystallization kinetics.¹² Although in-situ techniques have helped directly measure reaction

kinetics and crystallization pathways, few experimental techniques can exactly replicate the bulk reaction conditions used for MOF synthesis, therefore not accurately representing bulk reaction environments through in-situ data collection. Ex situ experimental techniques such as cryo transmission electron microscopy (cryo-TEM)¹³ allow for accurate replication of reaction conditions and can directly monitor the growth of MOFs in synthetic conditions by sampling from the bulk reaction and vitrifying the sample. Time-resolved techniques that sample aliquots from the bulk solution and stabilize the sample can more accurately represent the state of the overall reaction. Techniques such as in situ WAXS and SAXS cannot exactly replicate accurate conditions because the reaction takes place in a smaller reaction volume to fit the experimental setup than is used in the bulk reaction. This discrepancy makes comparing different technical approaches challenging. For example, changing the reaction volume and vessel size leads to changes in the extrinsic effects, which directly affect the surface energy barrier to nucleation.¹⁴ Studies have observed a decrease in nucleation rate by increasing the degree of confinement on a system by lowering the volume where synthesis and crystallization can take place.¹⁵ Calcium phosphate and calcium carbonate systems have demonstrated the stabilization of amorphous aggregates with the introduction of spatial constraints.¹⁶ In the case of calcium carbonate systems, with an increase in confinement, amorphous calcium carbonate (ACC) is more stabilized than crystalline polymorphs of calcium carbonate.¹⁷ Increasing the rate of nucleation and growth by altering the reaction vessel size is commonly observed in cases of scaling up the reaction for industrial purposes. The scaled-up synthesis results in different crystalline sizes than those reported from smaller-scale synthesis.^{16,18}

In this chapter, we investigate the effect of reaction vessel confinement on the rate of crystallization of zeolitic imidazolate framework 8 (ZIF-8) with the use of in-situ WAXS and time-

resolved scanning electron microscopy (SEM). The information discussed in this chapter is essential for studying MOF nucleation and growth when we compare the reaction kinetics monitored by that in a small capillary to the reaction on a larger scale.

3.2 Results and Discussion

To understand the effect that confinement has on the nucleation and growth of ZIF-8, the extent of crystallization after 4 hours of reaction time in different-sized reaction vessels was measured using in-situ WAXS (Figure 3.1). In-situ WAXS was performed to monitor the crystallization of ZIF-8 and performed on the Next Generation SAXS/WAXS line of the BioPacific MIP (Santa Barbra, CA). The ZIF-8 reaction was initiated by mixing precursor solutions of HmIm (1400 mM, 1 mL) and Zn (40 mM, 1 mL) that were prepared with Milli-Q water to yield ZIF-8 in a 15 mm (2mL) vial with HmIm:Zn of ratio 35:1. Immediately after mixing, 20 μ L of the ZIF-8 solution was pipetted into a 1 mm quartz capillary and the solutions were left to react for 4 hours without stirring. After the reaction time, 20 μ L from the ZIF-8 solution from the 15 mm vial was pipetted into a 1 mm capillary, and the two capillaries were mounted for WAXS collection. Integration of the first crystalline peak ($q = 0.5\text{-}0.53 \text{ 1/\AA}$) was taken to determine the extent of crystallinity (Figure 2a). The reaction of ZIF-8 in the vial resulted in a greater extent of crystallization than the reaction that occurred in the more confined 1 mm capillary. To compare using direct observation, SEM was taken after 4 hours of reaction in a 1 mm capillary (Figure 3.2b) and 15 mm vial (Figure 3.2c) to determine the crystalline structure of these two systems. ZIF-8 collected from the 15 mm vial contains more defined facets but the crystals are smaller than the ZIF-8 collected from the 1 mm capillary.

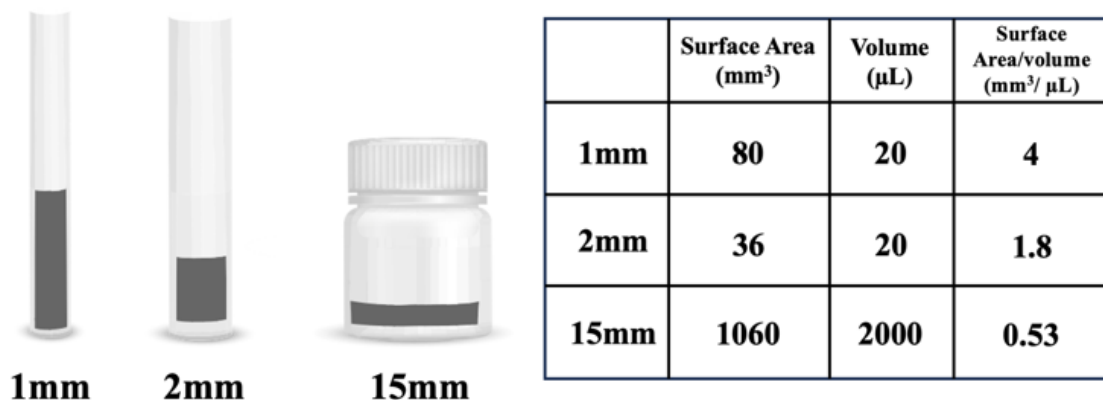


Figure 3.1 Summary of reaction volumes and container sizes with surface area to volume calculations.

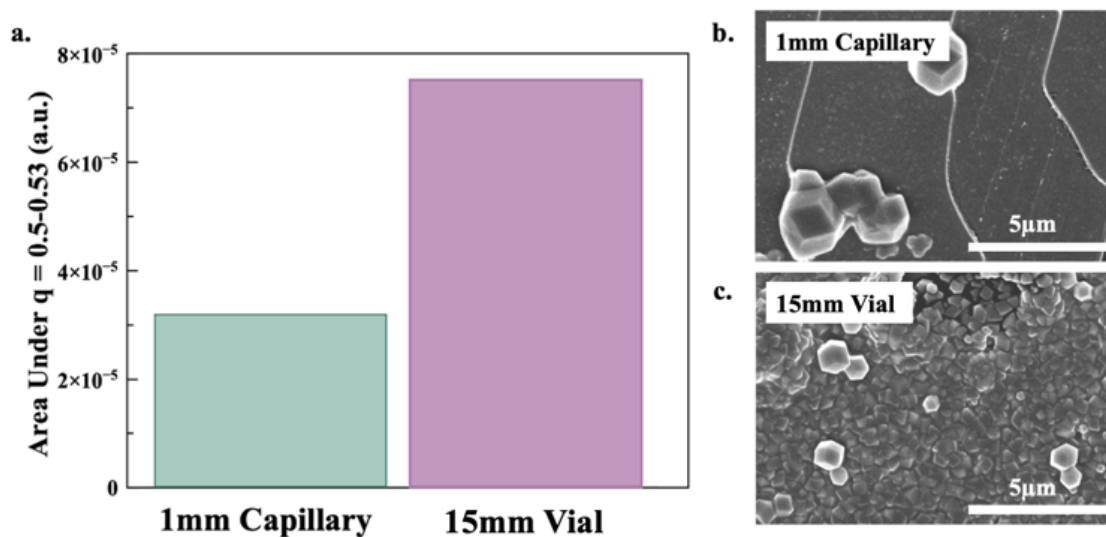


Figure 3.2 WAXS of ZIF-8 35:1. (a) Integration under the first crystalline peaks ($q = 0.5-0.53$ $1/\text{\AA}$) after 4 hours of reaction in a 1 mm glass capillary and 15 mm vial. SEM was collected after 4 hours of reaction in (b) 1 mm glass capillary and (c) 15 mm vial.

To determine if the confinement effects that slow crystallization between a 15 mm vial and a 1 mm capillary are observed at smaller scales, in-situ WAXS of ZIF-8 was collected and monitored through the reaction in 1 mm and 2 mm capillaries. The ZIF-8 reaction was initiated by mixing precursor solutions of HmIm (700 mM and 1400 mM 1 mL) and Zn (40 mM, 1 mL) that were prepared with Milli-Q water to yield ZIF-8 with HmIm: Zn ratios of 17.5:1 and 35:1 respectively. 20 μ L of the solutions were immediately added to a quartz capillary (1, 2 mm). The capillary was then mounted into the instrument over a 5 min period. The data collection began once the sample was mounted. We define $t = 0$ as the time of mixing, and the first data was collected at $t = 10$ minutes. Following measurements, the data was normalized against the background, and the integrated intensity under the 0.49-0.55 and 0.68-0.80 ($1/\text{\AA}$) peaks were plotted to determine the crystallization rate. Figures 3a and 3b show the WAXS plots of HmIm: Zn ratios of 17.5 and 35:1, respectively, over the reaction time of 350 min. Figure 3b shows that for the 35:1 system, there is an exponential increase in crystallization that results in reaching the full extent of crystallinity at around 3 hours, which is consistent with the data that has been previously reported for 35:1.¹² In the smaller capillary size of 1 mm it is clear that the time to full extent of crystallinity is reached at a later time point and the total amount of crystallinity does not reach as high as is observed in the 2 mm capillary. Figure 3.3a shows that for the 17.5 system, there is an exponential increase in crystallinity, similar to that seen in the 35.1 system, but when the same reaction takes place in a smaller capillary, the rate of reaction changes, showing a slow increase in crystallinity with no observable plateau.

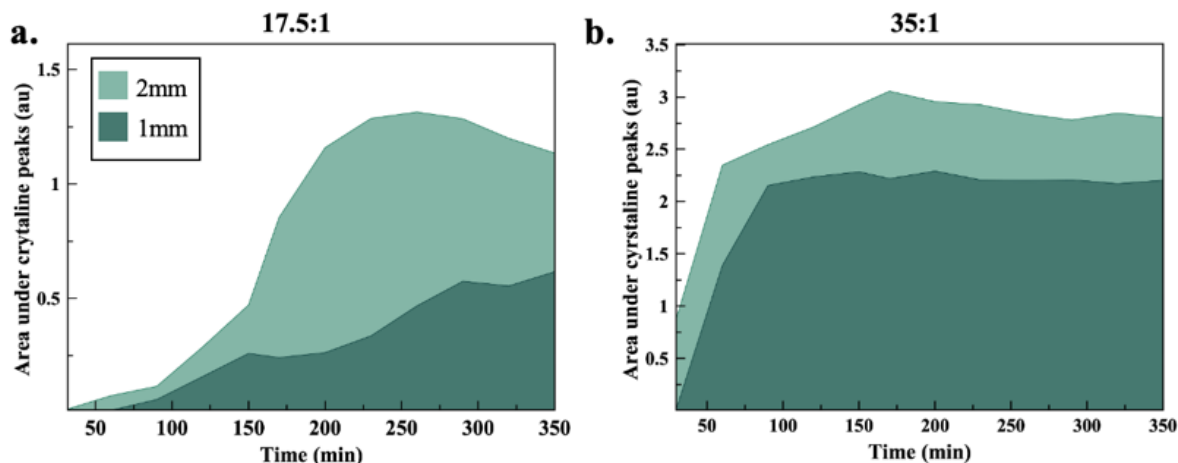


Figure 3.3 Integration under the first 3 crystalline peaks ($q = 0.49\text{-}0.55$ and $0.68\text{-}0.80$ $1/\text{\AA}$) of ZIF-8 with Hmim:Zn ratios of (a) 17.5:1 and (b) 35:1 in special glass capillaries of 1 mm and 2 mm. WAXS was collected every 30 min with a scan time of 10 min.

To understand the crystalline phases of each of these systems, SEM of 17.5:1 ZIF-8 was taken at time points in the nucleation and growth after 1, 3, and 4 hours of reaction time in 1 mm and 2 mm capillaries (Figure 3.4a-f). In the 2 mm capillary, it is seen that shortly after the reaction initiates, amorphous precursors, are observed after one hour (Figure 3.4d) and form into crystalline domains after 3 hours (Figure 3.4e), which correlates to the sharp increase in crystallinity observed in the rate of crystallization plotted in figure 3.3a. The reaction that occurs in the 1 mm capillary crystallizes at a much slower rate, and even after 3 hours, are mainly amorphous precursors observed after 3 hours of reaction time (Figure 3.4b). 35:1 ZIF-8 reached complete crystallization much faster than 17.5:1 ZIF-8, reaching a plateau before 1 hour for the reaction taking place in the 2 mm capillary and just after 2 hours for the reaction taking place in the 1 mm capillary (Figure 3.3b). The morphology can be tracked through SEM, where defined structure domains are observed after 2 hours for the 1 mm reaction, but after just 1 hour for the 2 mm reaction

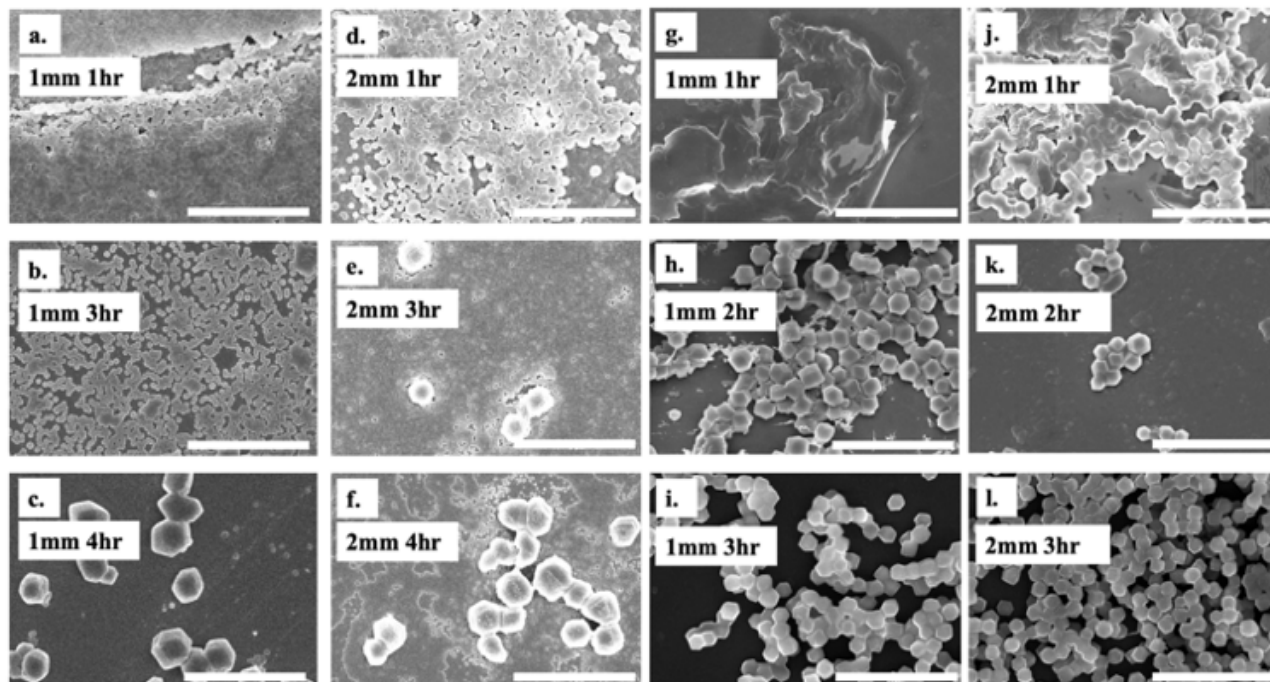


Figure 3.4 SEM ZIF-8 with Hmim:Zn ratio of 17.5 with reaction in (a-c) 1 mm capillaries and (d-f) 2 mm capillaries at reaction times of 1,3 and 4 hours. SEM of 35:1 (g-i) 1 mm capillaries and (j-l) 2 mm capillaries at reaction times of 1,2 and 3 hours.

The surface area to volume ratio increases $\sim 2x$ as the confinement increases from 2 mm to 1 mm and $\sim 8x$ as the confinement increases from 15 mm vial in bulk reaction to a 1 mm capillary. When the confinement increases, metastable or amorphous intermediates are stabilized, as demonstrated by the slower rates of nucleation and growth presented in the in-situ WAXS data. To further understand the effect of stabilizing these metastable intermediates, the average sizes at the final SEM collection time of 4 hours for 17.5:1 and 3 hours for 35:1 (Table 3.1). The average size for the more confined conditions was larger by around 100 nm. The size distribution of ZIF-8 formed in the smaller capillary with more confinement led to a more significant standard deviation in the sizes, which is consistent with a stabilization of metastable and amorphous intermediates and slow growth conditions seen in zeolitic species.^{4,6,15,16}

HmIm:Zn	Reaction Time (h)	Capillary Size (mm)	Average (nm)
17.5:1	4	1	1320±275
		2	1237±192
35:1	3	1	710±73
		2	663±56

Table 3.1 Summary of crystal sizes (nm) for ZIF-8 at two different HmIm/Zn Ratios (17.5:1, 35:1) with capillary sizes of 1 and 2 mm.

3.3 Conclusion

In conclusion, this work has shown that the environment in which ZIF-8 crystallizes can have a significant effect on the degree of crystallinity and the rate of growth. As the degree of confinement increases, the crystallization slows and the degree of crystallinity decreases as well. This was demonstrated with ZIF-8 and the comparison between 15 mm vial solutions and the reaction in 1 mm and 2 mm capillaries. Consideration of this effect is an important factor to consider when designing experimental procedures where the kinetics of nucleation and growth are measured with techniques that require different synthesis volumes such as in-situ WAXS, SAXS, or other spectroscopy methods.

3.4 Methods

Materials

All chemical reagents used for ZIF-8 were obtained from Sigma Aldrich and were used without further purification unless stated otherwise. Stock solutions of bovine serum albumin, β -cyclodextrin, 2-methylimidazole (HmIm), and zinc acetate (Zn) were made using Milli-Q water (18MW). Glass capillaries were obtained from Hampton Research.

ZIF-8 Synthesis

Stock solutions of 2-methylimidazole (HmIm) (1400 mM and 700 mM, 1 mL) and zinc acetate (Zn) (40 mM, 1 mL) were prepared in water ($\rho > 18 \text{ M}\Omega \text{ cm}$). Stock solutions were then used to prepare a series of crystallization experiments with variation in the HmIm:Zn ratio (35:1, 17.5:1). Zinc acetate solution was added to 2-methylimidazole solutions, and crystallization was initiated. The solutions were aged for 24 h at room temperature without stirring.

SEM

Samples were prepared by pipetting 10 μL of MOF sample onto 1 mm thick glass slides, then coated with 5 nm Iridium (Quorum Q150T) to reduce charging. Samples were imaged with a Magellan 400 XRH system with secondary electron images taken at an accelerating current ranging from 2-3 keV.

In-situ WAXS (BioPacific MIP)

WAXS samples were prepared in 2 mL quantities as described in the ZIF-8 synthesis, and immediately after mixing, 20 μL of each solution was added to 1 and 2 mm in diameter special glass capillaries (10-micron wall thickness) and mounted onto custom-built sample holder. The solutions were mounted vertically with the bottom of the capillary in the viewing window to ensure

the entire width of the capillary was being sampled. In-situ wide X-ray scattering (WAXS) measurements were performed on the WAXS platform instrument in the BioPACIFIC MIP (Materials Innovation Platform) at the University of California, Santa Barbara. The SAXS instrument was custom-built using a high-brightness liquid metal jet X-ray source (Excillum MetalJet D2+ 70 keV) and a 4-megapixel hybrid photon-counting X-ray area detector (Dectris Eiger2 R 4M). Measurements took place in ambient temperatures. A silver behenate standard was used as a calibrant. Data was analyzed using the Nika package for Igor Pro. Background subtraction was performed via an in-house MATLAB script.

WAXS Analysis

A MATLAB script was developed to track the ratio of crystalline material to amorphous material captured in the time-resolved WAXS spectra. Crystallinity was tracked by integrating the area under the curve for the first two crystalline peaks. A local background was estimated for each peak to account for variation in the background between scans. This was done by sitting 5 points to the left of the left peak edge and the 5 points to the right of the right peak edge with a line. Then, the area under the curve was calculated between the WAXS peak as the upper boundary scans which would otherwise dominate the integrated signal. Next, the amorphous peak area was estimated. Again, a line was fit in the amorphous region of the WAXS spectra, and the signal was integrated with the WAXS signal as the upper boundary and the fitted line as the lower boundary. Finally, the crystallinity ratio was calculated as the ratio of the integrated crystalline peak area to the integrated amorphous peak area. This was done for each time point, and the results are plotted in Figure B2.

3.5 Acknowledgements

This work was primarily supported by the National Science Foundation CBET Award #2102033. The authors acknowledge the use of facilities and instrumentation at the UC Irvine Materials Research Institute (IMRI), which was supported in part by the National Science Foundation through the UC Irvine Materials Research Science and Engineering Center (DMR-2011967).

The use of the BioPACIFIC WAXS/SAXS instrument was supported by the BioPACIFIC Materials Innovation Platform of the National Science Foundation under Award No. DMR-1933487.

3.6 References

- (1) Confinement of Ultrasmall Cu/ZnOx Nanoparticles in Metal–Organic Frameworks for Selective Methanol Synthesis from Catalytic Hydrogenation of CO₂ | Journal of the American Chemical Society. <https://pubs.acs.org/doi/10.1021/jacs.7b00058> (accessed 2024-04-23).
- (2) Carpenter, B. P.; Talosig, A. R.; Mulvey, J. T.; Merham, J.; Patterson, J. P. The Role of Molecular Modification and Protein Folding in the Nucleation and Growth of Protein-Metal-Organic Frameworks. *Chem. Mater.* **2022**.
- (3) Zhou, Z.; Yu, F.; Ma, J. Nanoconfinement Engineering for Enhanced Adsorption of Carbon Materials, Metal–Organic Frameworks, Mesoporous Silica, MXenes and Porous Organic Polymers: A Review. *Environ. Chem. Lett.* **2022**, 20 (1), 563–595. <https://doi.org/10.1007/s10311-021-01355-z>.
- (4) Wang, Y.-W.; Christenson, H. K.; Meldrum, F. C. Confinement Leads to Control over Calcium Sulfate Polymorph. *Adv. Funct. Mater.* **2013**, 23 (45), 5615–5623. <https://doi.org/10.1002/adfm.201300861>.
- (5) Grommet, A.B., Feller, M. & Klajn, R. Chemical reactivity under nanoconfinement. *Nat. Nanotechnol.* **15**, 256–271 (2020). <https://doi.org/10.1038/s41565-020-0652-2>
- (6) Beato, C.; Fernández, M. S.; Fermani, S.; Reggi, M.; Neira-Carrillo, A.; Rao, A.; Falini, G.; Arias, J. L. Calcium Carbonate Crystallization in Tailored Constrained Environments. *CrystEngComm* **2015**, 17 (31), 5953–5961. <https://doi.org/10.1039/C5CE00783F>.
- (7) Borrero-López, A. M.; Greca, L. G.; Rojas, O. J.; Tardy, B. L. Controlling Superstructure Formation and Macro-Scale Adhesion via Confined Evaporation of Cellulose Nanocrystals. *Cellulose* **2023**, 30 (2), 741–751. <https://doi.org/10.1007/s10570-022-04937-4>.

- (8) Pang, M.; Cairns, A. J.; Liu, Y.; Belmabkhout, Y.; Zeng, H. C.; Eddaoudi, M. Synthesis and Integration of Fe-Soc-MOF Cubes into Colloidosomes via a Single-Step Emulsion-Based Approach. *J. Am. Chem. Soc.* **2013**, 135 (28), 10234–10237. <https://doi.org/10.1021/ja403994u>.
- (9) Cui, J.; Gao, N.; Yin, X.; Zhang, W.; Liang, Y.; Tian, L.; Zhou, K.; Wang, S.; Li, G. Microfluidic Synthesis of Uniform Single-Crystalline MOF Microcubes with a Hierarchical Porous Structure. *Nanoscale* **2018**, 10 (19), 9192–9198. <https://doi.org/10.1039/C8NR01219A>.
- (10) Łuczak, J.; Kroczevska, M.; Baluk, M.; Sowik, J.; Mazierski, P.; Zaleska-Medynska, A. Morphology Control through the Synthesis of Metal–Organic Frameworks. *Adv. Colloid Interface Sci.* **2023**, 314, 102864. <https://doi.org/10.1016/j.cis.2023.102864>.
- (11) Huang, X.; Lin, D.; Duan, P.; Chen, H.; Zhao, Y.; Yang, W.; Pan, Q.; Tian, X. Space-Confinement Growth of Nanoscale Metal–Organic Frameworks/Pd in Hollow Mesoporous Silica for Highly Efficient Catalytic Reduction of 4-Nitrophenol. *J. Colloid Interface Sci.* **2023**, 629, 55–64. <https://doi.org/10.1016/j.jcis.2022.09.075>.
- (12) Cravillon, J.; Schröder, C.A.; Nayuk, R.; Gummel, J.; Huber, K.; Wiebcke, M. Fast Nucleation and Growth of ZIF-8 Nanocrystals Monitored by Time-Resolved In Situ Small Angle and Wide-Angle X-ray Scattering. *Angew. Chem., Int. Ed.*, 2001, **50**, 8067–8071 <https://onlinelibrary.wiley.com/doi/10.1002/anie.20110207>.
- (13) Liu, X.; Chee, S. W.; Raj, S.; Sawczyk, M.; Král, P.; Mirsaidov, U. Three-Step Nucleation of Metal–Organic Framework Nanocrystals. *Proc. Natl. Acad. Sci.* **2021**, 118 (10), e2008880118. <https://doi.org/10.1073/pnas.2008880118>.
- (14) Carpenter, B. P.; Talosig, A. R.; Rose, B.; Palma, G. D.; Patterson, J. P. Understanding and Controlling the Nucleation and Growth of Metal–Organic Frameworks. *Chem. Soc. Rev.* **2023**, 52 (20), 6918–6937. <https://doi.org/10.1039/D3CS00312D>.
- (15) Meldrum, F. C.; O’Shaughnessy, C. Crystallization in Confinement. *Adv. Mater.* **2020**, 32 (31), 2001068. <https://doi.org/10.1002/adma.202001068>.
- (16) Cantaert, B.; Beniash, E.; Meldrum, F. C. Nanoscale Confinement Controls the Crystallization of Calcium Phosphate: Relevance to Bone Formation. *Chem. – Eur. J.* **2013**, 19 (44), 14918–14924. <https://doi.org/10.1002/chem.201302835>.
- (17) Stephens, C. J.; Ladden, S. F.; Meldrum, F. C.; Christenson, H. K. Amorphous Calcium Carbonate Is Stabilized in Confinement. *Adv. Funct. Mater.* **2010**, 20 (13), 2108–2115. <https://doi.org/10.1002/adfm.201000248>.
- (18) Jin, B.; Li, H.-R.; Wei, Z.; Yan, M.; Yuan, C.; Wu, Y.-B.; Li, S.-D. Prediction of Heptagonal Bipyramidal Nonacoordination in Highly Viable [OB-M©B7O7-BO]– (M = Fe, Ru, Os) Complexes. *Commun. Chem.* **2022**, 5 (1), 1–7. <https://doi.org/10.1038/s42004-021-00620-0>.

Appendix B:
Supplementary Information for Chapter 3

Appendix B: Supplementary Information for Chapter 3

B.1 WAXS Analysis

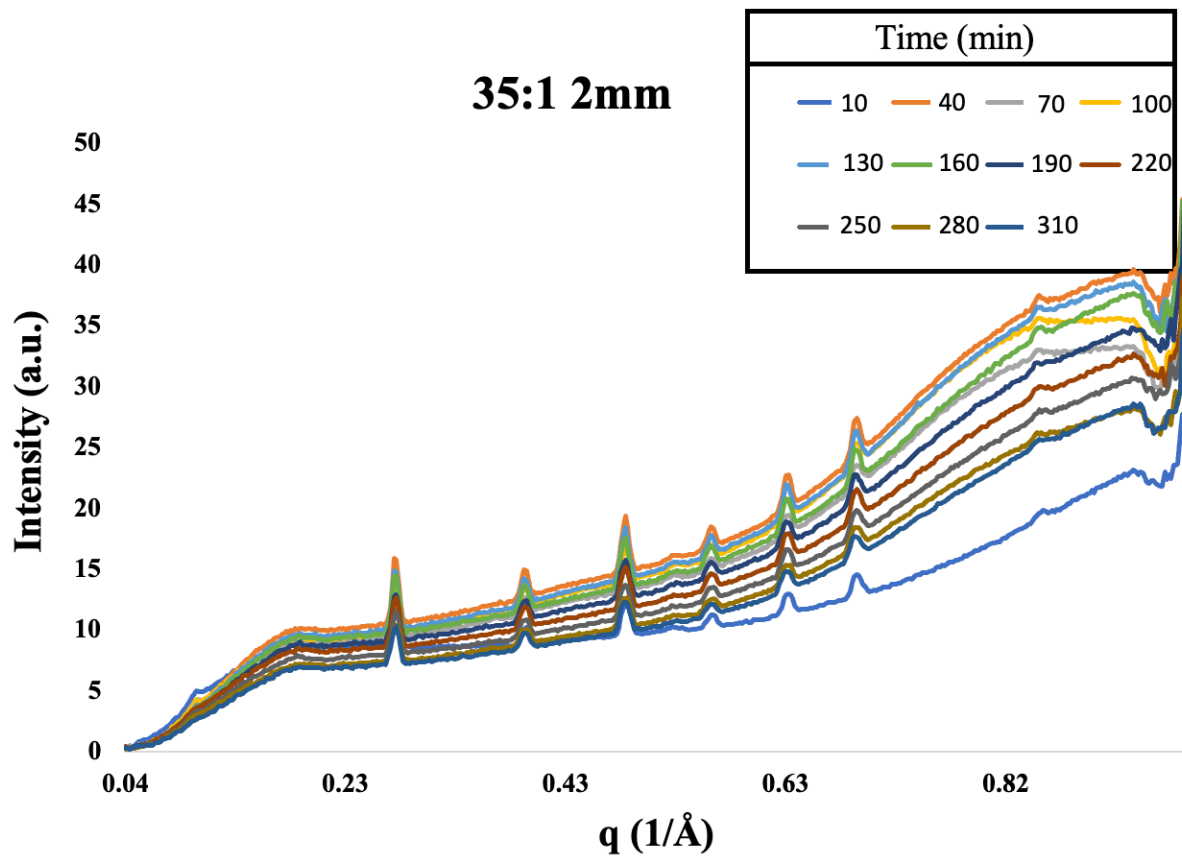


Figure B1 Time-resolved WAXS of 35:1 ZIF-8 over 310 min with scans every 30 min.

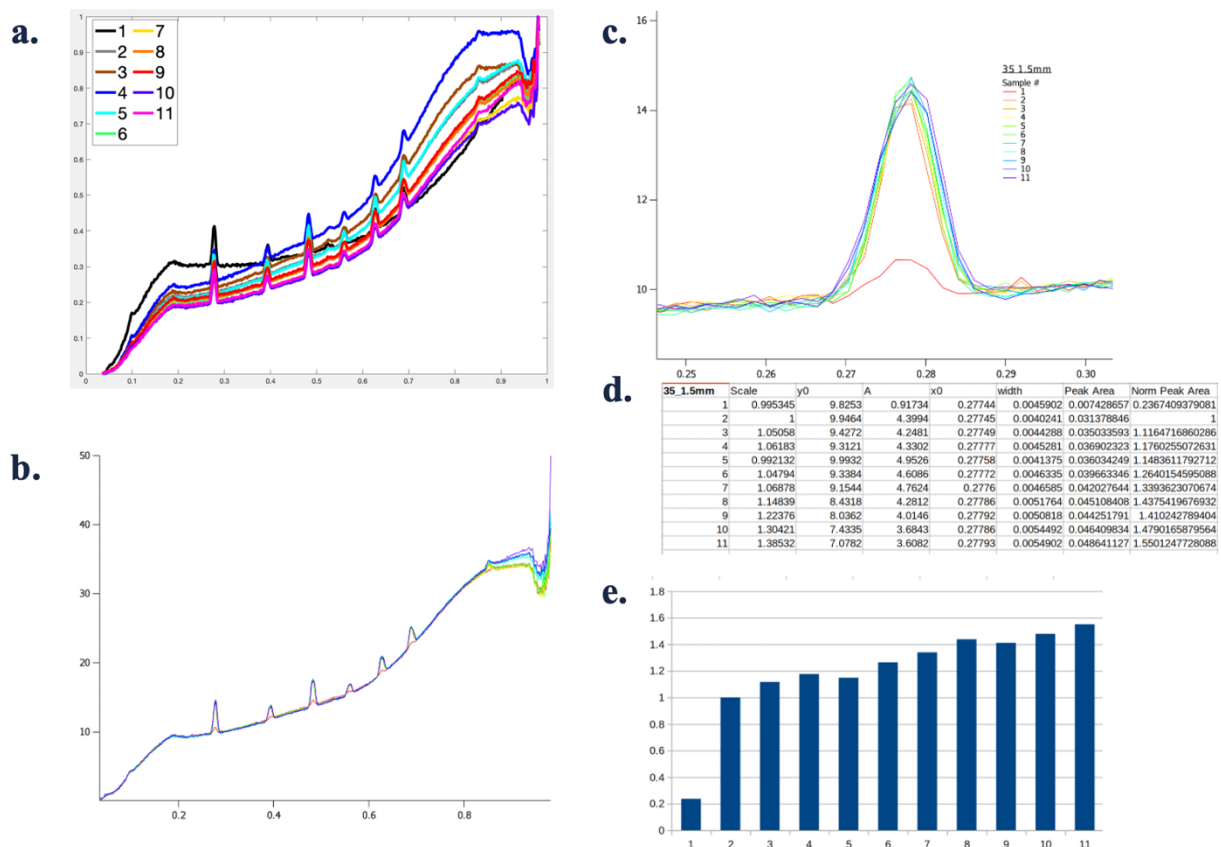


Figure B2 WAXS analysis (a) time-resolved WAXS of 35:1 ZIF-8 over 310 min with scans every 30 min (b) normalized WAXS 35:1 ZIF-8 (c) normalized area of peak with $q = 0.27-0.29$ $1/\text{\AA}$ (d) peak analysis table showing the scaling and the peak area and normalized peak area (e) sum of normalized peak area.

B.2 Crystal Size Analysis

SEM was used to determine crystal diameter by averaging the length of ~50-100 crystals per sample using Fiji, ImageJ (Figure B.3).

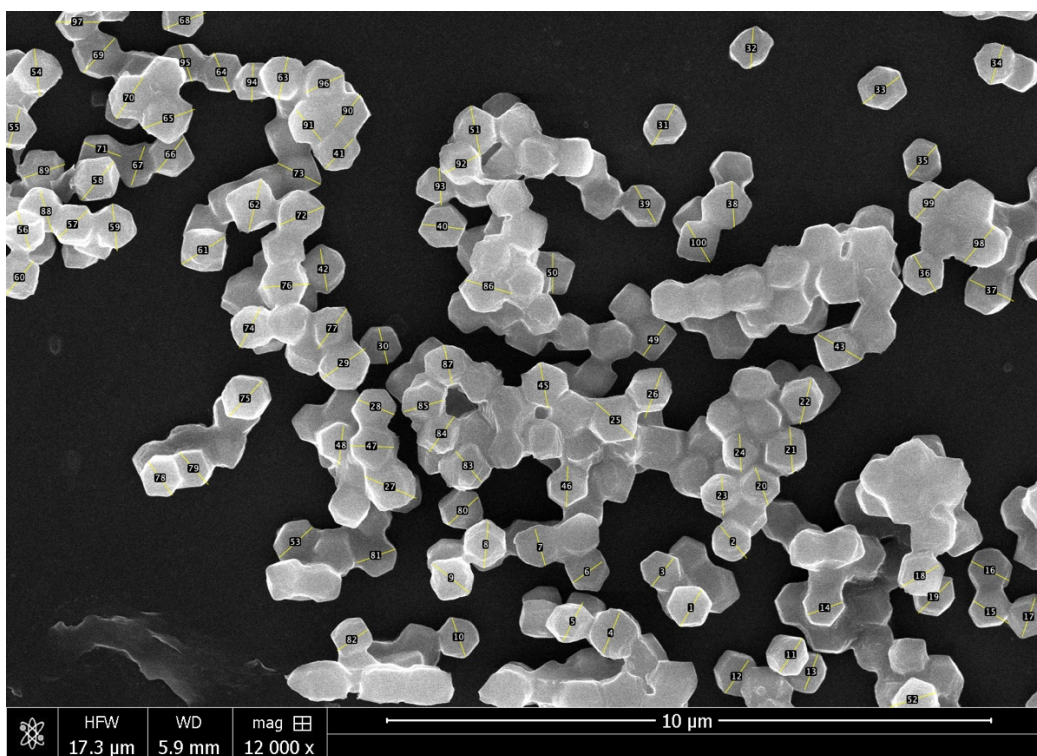


Figure B.3 SEM image (scale bar 10 μm) of ZIF-8 at 35:1 (HmIm:Zn) after 3 hours of reaction in 1 mm capillary. Numbered yellow lines indicate the diameter of the crystal measured using Fiji, ImageJ.

Chapter 4:
Supramolecular Modification of BSA

Chapter 4: Supramolecular Modification of BSA

4.1 Introduction

Metal-organic frameworks (MOFs), also known as porous coordination polymers (PCPs), are a class of nanoporous materials defined by a lattice built of inorganic nodes bridged by organic linkers. MOFs have a wide range of applications due to their ultra-high surface area, fixed porosity, and high thermal stability.¹ Properties such as pore size, volume, geometry, and molecular functionality can be designed for a specific application, such as crystal engineering. Further applications of MOFs include gas and energy storage,² targeted drug delivery, chemical and biological sensing,³ and gas separation. The fixed porosity of MOFs can be designed to encapsulate molecules based on their size and shape. Encapsulation of biomolecules within MOFs has been investigated for application in drug delivery, catalysis, and sensors.⁴⁻⁶ It has been shown that encapsulating biomolecules within the framework can increase the activity and stability of the biomolecule.^{5,7} Biomolecules can be incorporated by *in-situ* approaches in which the crystal forms in the presence of a protein, or post-synthetic approaches like surface attachment, pore entrapment,⁸ or covalent linkage.^{9,10} *In-situ* approaches are advantageous because of the mild synthetic conditions and simple synthetic parameters that can protect the enzyme or biomolecule.

To understand the factors that contribute to biomolecule encapsulation and its function in MOF formation, it is crucial to understand the nucleation and growth mechanisms. Comprehension of the potentially non-classical routes of crystal growth and amorphous precursors in protein-MOF (p-MOF) systems facilitates the streamlined development of p-MOFs for specific purposes by utilizing the structure-function relationship.¹¹ Polymorph control is a

foundation of crystal engineering but has been largely unexplored in p-MOF systems. Synthetic conditions such as ligand-to-metal ratio, precursor concentrations, and choice of biomolecule are known to affect the final crystal morphology.⁷ Particle morphology and crystal size are important factors for optimizing the performance of MOFs, influencing surface area, pore size and diffusion resistance.^{12,13}

Extensive research has been done to understand the encapsulation of larger biomolecules,^{3,14} driven by high interest in utilizing MOFs for targeted drug delivery systems.^{9,15,16} Large biomolecules, like proteins, face challenges with encapsulation due to their size, in comparison to smaller biomolecules.¹⁷ Efforts to encapsulate proteins into MOFs have included protein conjugation with MOF linkers,¹⁸ protein diffusion into MOFs by matching the pore sizes of the MOF to the protein,¹⁹ and protein adsorption on the outside of MOFs for proteins with more rigid conformations.²⁰ Researchers face many obstacles in the encapsulation of larger biomolecules, such as biomolecule preservation and loading optimization. To aid in this effort, we aimed to explore the modification of larger biomolecules for facile loading without functional change.²¹

Molecular modification of biomolecules shows that a biomolecule with a low charge would not typically induce crystallization but can be surface functionalized with a charged group and lead to p-MOF formation.²² Although surface modification of uncharged biomolecules can aid in the encapsulation, with larger biomolecules it would not always be of interest to charge the surface or change the functionality. To modify these biomolecules, supramolecular modification is of interest to add a charged group that can be removed easily upon release of the biomolecule without changing the intrinsic functionality.

Cyclodextrins (CDs) are made up of glucopyranose units bound together in a ring forming a cone-shaped structure. The most common structures are α -, β -, and γ -CDs that contain 6, 7, and 8 sugar units. Due to their cone-like structure, CDs contain a hydrophilic exterior and semi-polar interior cavity.²³ CDs complexed with proteins have shown reduced protein aggregation and higher structural stability to physical changes.^{24,25} If the CD complexed biomolecules can aid in higher encapsulation or modification to the MOF framework, there is an opportunity for utilizing common MOF traits to aid in biomolecule storage, activity,²⁶ and controlled delivery.²⁷

Zeolitic imidazolate frameworks (ZIFs) are a subclass of MOFs that are topologically similar to zeolites.²⁸ ZIFs are composed of tetrahedrally coordinated transition metal ions that are connected by imidazolate linkers. In the case of zeolitic imidazolate framework-8 (ZIF-8), the structure is formed by the coordination of Zn^{2+} ions and 2-methylimidazolate. ZIF-8 has been thoroughly investigated, in part, because it can be synthesized in water at room temperature. This feature makes ZIF-8 ideal for encapsulating biomolecules during the synthesis in a process analogous to biomineralization. Our group has previously studied the encapsulation of biomolecules such as bovine serum albumin (BSA) and Fluorescein isothiocyanate (FITC) tagged BSA into ZIF-8. This research provided a better understanding of the ideal biomolecule for encapsulation in terms of isoelectric point, charge, and biomolecule size.²¹ However, the origin of polymorph control in ZIF-8 is still unknown, and there is a need to develop new methods to control p-MOF nucleation and growth.

In the following chapter, we explore the effect of biomolecule supramolecular modification on the ZIF-8 nucleation and growth mechanisms. A combination of scanning

electron microscopy (SEM), powder X-ray diffraction (PXRD), and fluorescence spectroscopy are used to uncover crystal morphology, crystallinity, and encapsulation efficiency.

4.2 Results

Supramolecular modification of p-MOFs

To characterize the formation of a CD:BSA complex, we performed fluorescence spectroscopy and zeta potential measurements on BSA and CD:BSA with molar ratios of 4:1, 3:1, 2:1, 1:1 with an overall molar concentration of 2.5 mg/ml BSA. These solutions were prepared as described in the experimental section. Fluorescence intensity was measured for all CD:BSA ratios and BSA solutions (Figure 4.1). The results show that the fluorescence of BSA is suppressed with the addition of CD. This fluorescence quenching upon the addition of CD shows that there is an interaction between the protein and CD forming a CD:BSA complex.²⁹ In addition, the zeta potential of the CD:BSA solutions was measured (Figure 4.1). It is shown that the BSA solution without the addition of CD has the highest charge. As increasing molar ratios of CD are added to BSA the zeta potential decreases.

The CD-BSA-ZIF-8 solutions were prepared as described in the experimental section to produce HmIm:Zn ratios of (70:1, 35:1, 17.5:1, 4:1), and CD:BSA ratio (4:1, 3:1, 2:1, 1:1, 0:1); all of which had protein concentrations of 2.5 mg/ml. The isolated CD-BSA-ZIF-8 crystals were analyzed by SEM, PXRD, and fluorescent spectroscopy to measure encapsulation efficiency.

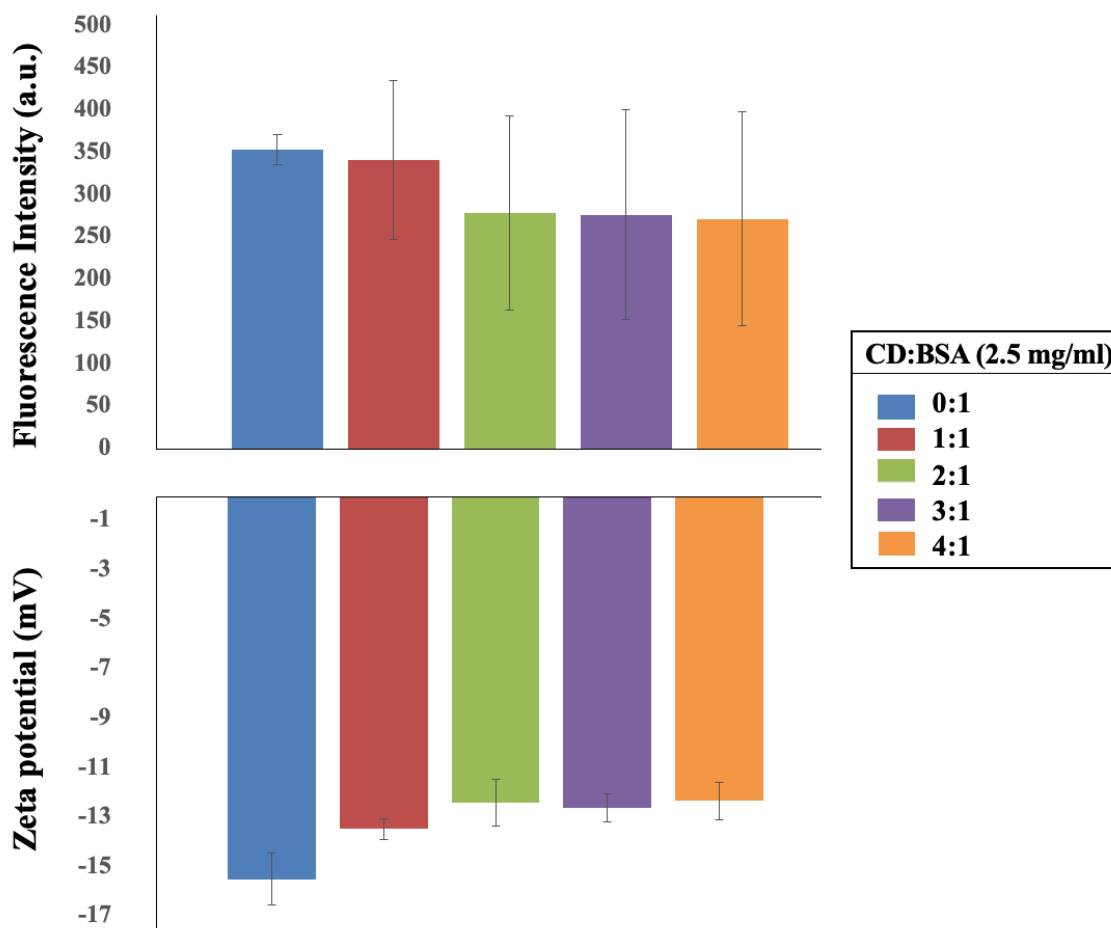


Figure 4.1 Fluorescence intensity and zeta potential of CD:BSA complex with final BSA concentration of 2.5 mg/mL (blue), and CD BSA molar ratios of 1:1 (red), 2:1 (green), 3:1 (purple), and 4:1 (orange). Triplicate measurements were made for all fluorescence and zeta potential measurements and averaged. Error bars denote the standard deviation for triplicate averaged experiments.

The BSA encapsulation efficiency (EE%) for BSA-CD- ZIF-8 was determined by measuring the concentration of the protein in the supernatant. EE% is calculated by quantifying the remaining protein concentration in the supernatant to back-calculate the protein concentration that was encapsulated in the MOF precipitate. EE% was measured using fluorescent spectroscopy where the emission intensity of tryptophan (~340 nm) was measured for BSA-ZIF-

8 and BSA-CD-ZIF- 8. Tryptophan fluorescence intensity is sensitive to the pH of the solution and the metal binding, so the supernatants for each solution were diluted in a phosphate buffer (pH 6.7) containing excess tetrasodium ethylenediaminetetraacetic acid (EDTA) to chelate zinc and ensure consistent protein conformation. EE% of BSA in CD-BSA-ZIF-8 was measured by fluorescence with ratios of CD:BSA of 4:1, 3:1, 2:1 and 1:1 and compared to a BSA-ZIF-8 system that contains no CD (Figure 4.2). At low HmIm ratios of 4:1 and 17.5:1, there is ~ 100% encapsulation for all ratios of CD:BSA. For CD-BSA- ZIF-8 at 35:1, the EE% is ~ 40% with no CD. With the addition of CD, the encapsulation increases slightly as the amount of CD increases but not as significantly as previous encapsulation studies with other modifications on BSA. CD-BSA-ZIF-8 at 70:1, which is typically the lowest BSA encapsulation without CD, is lowered slightly upon the addition of CD.

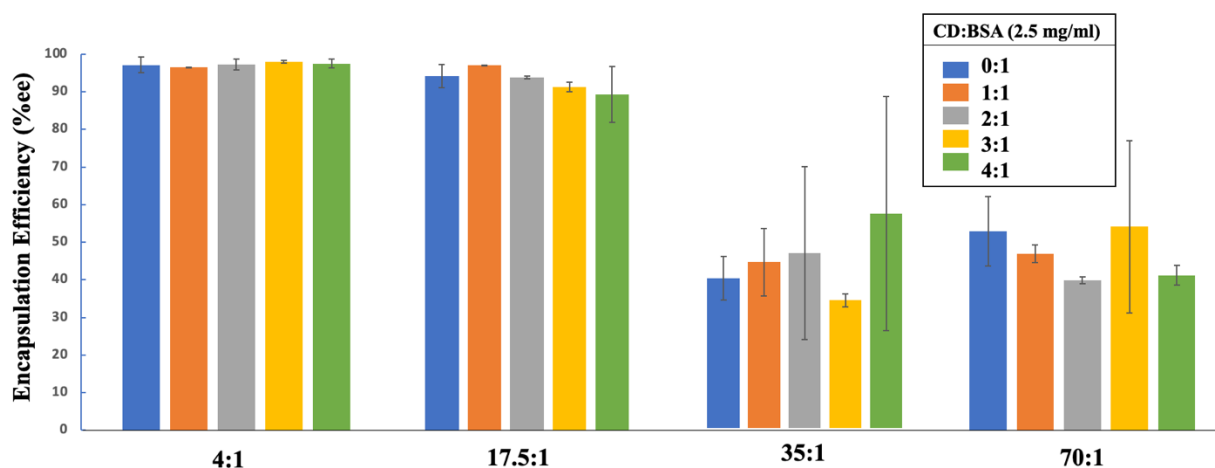


Figure 4.2 Encapsulation efficiency (EE%) of CD-BSA-ZIF-8 with final protein concentration 2.5 mg/mL and CD:BSA ratio of 0:1 (blue), 1:1 (orange), 2:1 (gray) 3:1 (yellow), 4:1 (green). Triplicate measurements were made for each system and averaged. Error bars denote the standard deviation of the triplicate averaged experiments.

To determine if the introduction of CD to CD-BSA-ZIF-8 affects the surface topology and polymorph formation, SEM and PXRD measurements were made with the various CD:BSA ratios. The crystals showed similar morphology (sod) in all HmIm:Zn ratios including 70:1, 35:1, 17.5:1, 4:1, and all CD:BSA ratios. There was no presence of the dia polymorph in the SEM or PXRD (Figure 4.3).

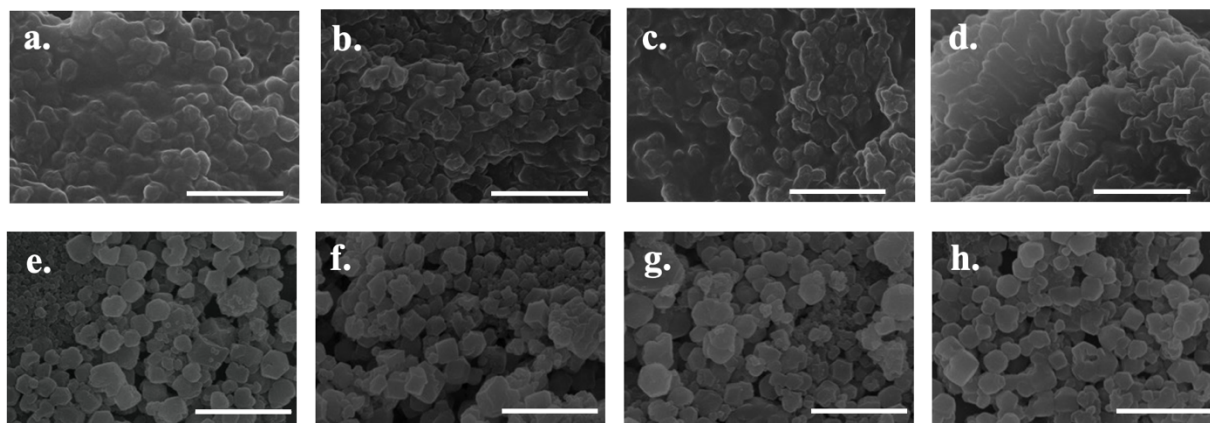


Figure 4.3 SEM of CD:BSA-ZIF-8 4:1 (a-d) and 70:1 (e-h) at final BSA concentration of 2.5 mg/mL at the following CD:BSA ratios: 1:1 (a,e), 2:1 (b,f), 3:1 (c,g), and 4:1 (d,h). The scale bar in each SEM image is 1 μm .

4.3 Discussion

Upon addition of CD to BSA, the fluorescence intensity of BSA decreases (Figure 4.1). The quenching of the BSA fluorescence intensity upon the addition of CD shows that a CD:BSA complex is formed. The fluorescence intensity of tryptophan is known to decrease with an increase in solvent polarity. This shows that the CD is introducing an increase in polarity of the microenvironment around the tryptophan sites on BSA. Previous studies have shown that CD binds to different areas of the BSA and aids in loosening the structure of BSA. This results in

more tryptophan exposure to the polar aqueous phase. To determine the effect that the addition of CD had on the overall charge of BSA, the zeta potential for each solution was measured (Figure 4.1). The solution that only contained BSA had the highest charge while the CD:BSA solution had a lower charge. This could be due to the lack of a charge on CD and due to this lack of charge it is believed that the biomolecule will have less influence on the crystallization.

The encapsulation studies performed over all studied HmIm:Zn ratios and CD:BSA ratios did not result in a significant change in encapsulation (Figure 4.2). This shows that although there is a CD:BSA complex forming and that it is modifying the conformation of BSA, this does not play a significant impact in influencing encapsulation. The morphology of the crystals does not change upon the addition of cyclodextrin. The crystal morphologies appeared to be small sod crystals of an even size distribution (Figure 4.3). This data shows that BSA has an impact on polymorph formation, but this does not point to any major influence of CD in polymorph formation.

4.4 Conclusions

This work showcases the ability to modify BSA with the addition of CD to affect the encapsulation of BSA in ZIF-8 frameworks. Through a study of the zeta potential, it is clear that the zeta potential is lowered, which would allow for lower encapsulation rates of CD:BSA complexes in comparison to BSA alone. CD:BSA complexes did not have a large effect on the overall polymorph formation of ZIF-8, producing only SOD polymorphs independent of HmIm:Zn ratio or CD:BSA ratio. This work shows that we can modify biomolecules and direct the encapsulation based on charge with only supramolecular modification.

4.5 Methods

Materials.

All chemical reagents used for ZIF-8 and BSA- ZIF-8 and CD-BSA-ZIF-8 were obtained from Sigma Aldrich unless stated otherwise. Stock solutions of bovine serum albumin, β -cyclodextrin, 2-methylimidazole (HmIm), and zinc acetate (Zn) were made using Milli-Q water ($r > 18\text{MW cm}$).

ZIF-8 and BSA-ZIF-8 Synthesis.

Stock solutions of 2-mthylimidazole (HmIm) (400 mM, 300 mM, 250 mM, and 200 mM, 0.5 mL), zinc acetate (Zn) (40 mM, 1 mL) and bovine serum albumin (BSA) (10 mg/mL and 2.5 mg/mL, 0.5 mL) were prepared in water (18 MW). Stock solutions were then used to prepare a series of crystallization experiments with variations in the HmIm:Zn ratio (20:1, 15:1, 12.5:1, 10:1), and protein concentration (2.5 mg/mL, 0.625 mg/mL). Protein stock solutions were added to 2-methylimidazole solutions and crystallization was initiated by the introduction of the zinc acetate solution. The so- solutions were aged for 24 hours at room temperature without stirring and the precipitate was obtained via centrifugation at 10,000 rpm for 10 min. The precipitate was washed with water and centrifuged twice more and a final rinse with methanol.

Supramolecular modification CD-BSA-ZIF-8 synthesis

Stock solutions of 0.0075 mM BSA (20 mg/mL, 0.25mL) and methyl- β -cyclodextrin (CD) (0.0075 mM, 0.015 mM, 0.0225, and 0.03 mM, 0.25mL) were prepared in water (18 MW). The solutions were then used to prepare CD:BSA ratios of 1:1, 2:1, 3:1 4:1 (0.5mL) solutions. Stock solutions of HmIm (5600 mM, 2800 mM, 1400 mM, and 320 mM, 0.5 mL) and Zn (40 mM, 1 mL) in water (18 MW). Solutions were then mixed with CD:BSA solutions and used to prepare a

series of crystallization experiments with variations in the HmIm:Zn ratio (20:1, 15:1, 12.5:1, 10:1), and protein concentration of 2.5 mg/mL. CD:BSA stock solutions were added to 2-methylimidazole solutions and crystallization was initiated by the introduction of the zinc acetate solution. The solutions were aged for 24 hours without stirring and the precipitate was obtained via centrifugation at 10,000 rpm for 10 min. The precipitate was washed with water and centrifuged twice more and a final rinse with methanol.

SEM

Samples were prepared by pipetting 10 μ L of sample onto 1mm thick glass slides which were then coated with 5nm Iridium (Quorum Q150T) to reduce charging. Samples were imaged with a Magellan 400 XRH system with secondary electron images taken at an accelerating current ranging from 2-3 keV.

PXRD

After removing all liquid from the top of centrifuged crystal precipitates and allowing samples to air dry, a Rigaku SmartLab X-ray diffractometer was used to obtain PXRD patterns at 40 kV and 30 mA. Results were plotted with background subtraction using IGOR software.

Fluorescence Spectroscopy

The supernatant of the solutions was diluted times 10 in phosphate buffer solution, pH 6.7, with 25 mg/mL tetrasodium ethylenediaminetetraacetic acid (EDTA). Emission spectra were recorded on a Cary Eclipse fluorimeter (Varian) in a 3 mL quartz cuvette. Samples were excited at 280 and measured from 300 to 400 nm. All samples were measured in triplicate and averaged.

Zeta Potential

Measurements were taken with a Malvern Zetasizer ZS Nano dynamic light scattering instrument. Zeta potential samples were measured in a disposable capillary cell from Malvern

Panalytical. For each sample measurement, the instrument was set to automatic runs (ranging from 10 to 100) to ensure the instrument achieved sufficient signal, and averages of three measurements were taken.

4.6 Acknowledgements

Part of the research was funded by the University of California, Cancer Research Coordinating Committee, Award Number C21CR2080. The authors acknowledge the use of facilities and instrumentation at the UC Irvine Materials Research Institute (IMRI), which was supported in part by the National Science Foundation through the UC Irvine Materials Research Science and Engineering Center (DMR-2011967).

4.7 References

- (1) Furukawa, H.; Cordova, K. E.; O’Keeffe, M.; Yaghi, O. M. The Chemistry and Applications of Metal-Organic Frameworks. *Science* **2013**, *341* (6149). <https://doi.org/10.1126/science.1230444>.
- (2) Eddaoudi, M.; Kim, J.; Rosi, N. Systematic Design of Pore Size and Functionality in Isoreticular MOFs and Their Application in Methane Storage. *Science* **2002**, *295* (5554), 469-472. <https://www.science.org/doi/10.1126/science.1067208>
- (3) Xu, J.; Shimakoshi, H.; Hisaeda, Y. Development of Metal-Organic Framework (MOF)-B12 System as New Bio-Inspired Heterogeneous Catalyst. *J. Organomet. Chem.* **2015**, *782*, 89–95. <https://doi.org/10.1016/j.jorganchem.2014.11.015>.
- (4) Li, P.; Moon, S.-Y.; Guelta, M. A.; Lin, L.; Gómez-Gualdrón, D. A.; Snurr, R. Q.; Harvey, S. P.; Hupp, J. T.; Farha, O. K. Nanosizing a Metal–Organic Framework Enzyme Carrier for Accelerating Nerve Agent Hydrolysis. *ACS Nano* **2016**, *10* (10), 9174–9182. <https://doi.org/10.1021/acsnano.6b04996>.

- (5) Lyu, F.; Zhang, Y.; Zare, R. N.; Ge, J.; Liu, Z. One-Pot Synthesis of Protein-Embedded Metal–Organic Frameworks with Enhanced Biological Activities. *Nano Lett.* **2014**, *14* (10), 5761–5765. <https://doi.org/10.1021/nl5026419>.
- (6) Sun, C.-Y.; Qin, C.; Wang, X.-L.; Yang, G.-S.; Shao, K.-Z.; Lan, Y.-Q.; Su, Z.-M.; Huang, P.; Wang, C.-G.; Wang, E.-B. Zeolitic Imidazolate Framework-8 as Efficient pH-Sensitive Drug Delivery Vehicle. *Dalton Trans.* **2012**, *41* (23), 6906–6909. <https://doi.org/10.1039/C2DT30357D>.
- (7) Liang, K.; Ricco, R.; Doherty, C. M.; Styles, M. J.; Bell, S.; Kirby, N.; Mudie, S.; Haylock, D.; Hill, A. J.; Doonan, C. J.; Falcaro, P. Biomimetic Mineralization of Metal–Organic Frameworks as Protective Coatings for Biomacromolecules. *Nat. Commun.* **2015**, *6* (1), 7240. <https://doi.org/10.1038/ncomms8240>.
- (8) Pisklak, T. J.; Macías, M.; Coutinho, D. H.; Huang, R. S.; Balkus, K. J. Hybrid Materials for Immobilization of MP-11 Catalyst. *Top. Catal.* **2006**, *38* (4), 269–278. <https://doi.org/10.1007/s11244-006-0025-6>.
- (9) Jung, S.; Kim, Y.; Kim, S.-J.; Kwon, T.-H.; Huh, S.; Park, S. Bio-Functionalization of Metal–Organic Frameworks by Covalent Protein Conjugation. *Chem. Commun.* **2011**, *47* (10), 2904–2906. <https://doi.org/10.1039/C0CC03288C>.
- (10) Shih, Y.-H.; Lo, S.-H.; Yang, N.-S.; Singco, B.; Cheng, Y.-J.; Wu, C.-Y.; Chang, I.-H.; Huang, H.-Y.; Lin, C.-H. Trypsin-Immobilized Metal–Organic Framework as a Biocatalyst In Proteomics Analysis. *ChemPlusChem* **2012**, *77* (11), 982–986. <https://doi.org/10.1002/cplu.201200186>.
- (11) Yoreo, J. J. D.; Gilbert, P. U. P. A.; Sommerdijk, N. A. J. M.; Penn, R. L.; Whitelam, S.; Joester, D.; Zhang, H.; Rimer, J. D.; Navrotsky, A.; Banfield, J. F.; Wallace, A. F.; Michel, F. M.; Meldrum, F. C.; Cölfen, H.; Dove, P. M. Crystallization by Particle Attachment in Synthetic, Biogenic, and Geologic Environments. *Science* **2015**, *349* (6247). <https://doi.org/10.1126/science.aaa6760>.
- (12) Stock, N.; Biswas, S. Synthesis of Metal–Organic Frameworks (MOFs): Routes to Various MOF Topologies, Morphologies, and Composites. *Chem. Rev.* **2012**, *112* (2), 933–969. <https://doi.org/10.1021/cr200304e>.
- (13) Li, P.; Klet, R. C.; Moon, S.-Y.; Wang, T. C.; Deria, P.; Peters, A. W.; Klahr, B. M.; Park, H.-J.; Al-Juaid, S. S.; Hupp, J. T.; Farha, O. K. Synthesis of Nanocrystals of Zr-Based Metal–Organic Frameworks with Csq-Net: Significant Enhancement in the Degradation of a Nerve Agent Simulant. *Chem. Commun.* **2015**, *51* (54), 10925–10928. <https://doi.org/10.1039/C5CC03398E>.
- (14) Morris, R. E. How Does Your MOF Grow? *ChemPhysChem* **2009**, *10* (2), 327–329. <https://doi.org/10.1002/cphc.200800642>.
- (15) Taylor-Pashow, K. M. L.; Della Rocca, J.; Xie, Z.; Tran, S.; Lin, W. Postsynthetic Modifications of Iron-Carboxylate Nanoscale Metal–Organic Frameworks for Imaging and Drug Delivery. *J. Am. Chem. Soc.* **2009**, *131* (40), 14261–14263. <https://doi.org/10.1021/ja906198y>.
- (16) Liédana, N.; Galve, A.; Rubio, C.; Téllez, C.; Coronas, J. CAF@ZIF-8: One-Step Encapsulation of Caffeine in MOF. *ACS Appl. Mater. Interfaces* **2012**, *4* (9), 5016–5021. <https://doi.org/10.1021/am301365h>.
- (17) Zhuang, J.; Young, A. P.; Tsung, C.-K. Integration of Biomolecules with Metal–Organic Frameworks. *Small* **2017**, *13* (32), 1700880. <https://doi.org/10.1002/smll.201700880>.

- (18) Fujita, D.; Suzuki, K.; Sato, S.; Yagi-Utsumi, M.; Yamaguchi, Y.; Mizuno, N.; Kumasaka, T.; Takata, M.; Noda, M.; Uchiyama, S.; Kato, K.; Fujita, M. Protein Encapsulation within Synthetic Molecular Hosts. *Nat. Commun.* **2012**, *3* (1), 1093. <https://doi.org/10.1038/ncomms2093>.
- (19) Deng, H.; Grunder, S.; Cordova, K. E.; Valente, C.; Furukawa, H.; Hmadeh, M.; Gándara, F.; Whalley, A. C.; Liu, Z.; Asahina, S.; Kazumori, H.; O’Keeffe, M.; Terasaki, O.; Stoddart, J. F.; Yaghi, O. M. Large-Pore Apertures in a Series of Metal-Organic Frameworks. *Science* **2012**, *336* (6084), 1018–1023. <https://doi.org/10.1126/science.1220131>.
- (20) Ma, W.; Jiang, Q.; Yu, Pi. Zeolitic Imidazolate Framework-Based Electrochemical Biosensor for in Vivo Electrochemical Measurements. *Anal. Chem.* **2013**, *85* (15), 7550–7557. <https://pubs.acs.org/doi/10.1021/ac401576u>
- (21) Ogata, A.; Rakowski, A.; Carpenter, B.; Fishman, D. Direct Observation of Amorphous Precursor Phases in the Nucleation of Protein–Metal–Organic Frameworks *J. Am. Chem. Soc.* **2020**, *142* (3), 1433–1442. <https://pubs.acs.org/doi/abs/10.1021/jacs.9b11371>
- (22) Maddigan, N. K.; Tarzia, A.; Huang, D. M.; Sumbly, C. J.; Bell, S. G.; Falcaro, P.; Doonan, C. J. Protein Surface Functionalisation as a General Strategy for Facilitating Biomimetic Mineralisation of ZIF-8. *Chem. Sci.* **2018**, *9* (18), 4217–4223. <https://doi.org/10.1039/C8SC00825F>.
- (23) Connors, K. A. The Stability of Cyclodextrin Complexes in Solution. *Chem. Rev.* **1997**, *97* (5), 1325–1358. <https://doi.org/10.1021/cr960371r>.
- (24) Jóhannsdóttir, S.; Saokham, P.; Magnúsdóttir, A.; Loftsson, T. Cyclodextrin Complexes of a Globular Protein and a Lipophilic Oligopeptide: The Effect of Structure and Physicochemical Properties. *Pharm.* **2017**, *72* (10), 575–580. <https://doi.org/10.1691/ph.2017.7061>.
- (25) Goszczyński, T. M.; Gawłowski, M.; Girek, B.; Kowalski, K.; Boratyński, J.; Girek, T. Synthesis of β -Cyclodextrin-Lysozyme Conjugates and Their Physicochemical and Biochemical Properties. *J. Incl. Phenom. Macrocycl. Chem.* **2017**, *87* (3), 341–348. <https://doi.org/10.1007/s10847-017-0706-8>.
- (26) Lian, X.; Fang, Y.; Joseph, E.; Wang, Q.; Li, J.; Banerjee, S.; Lollar, C.; Wang, X.; Zhou, H.-C. Enzyme–MOF (Metal–Organic Framework) Composites. *Chem. Soc. Rev.* **2017**, *46* (11), 3386–3401. <https://doi.org/10.1039/C7CS00058H>.
- (27) Wu, M.-X.; Yang, Y.-W. Metal-Organic Framework (MOF)-Based Drug/Cargo Delivery and Cancer Therapy. *Adv. Mater. Deerfield Beach Fla* **2017**, *29* (23). <https://doi.org/10.1002/adma.201606134>.
- (28) Chen, B.; Yang, Z.; Zhu, Y.; Xia, Y. Zeolitic Imidazolate Framework Materials: Recent Progress in Synthesis and Applications. *J. Mater. Chem. A* **2014**, *2* (40), 16811–16831. <https://doi.org/10.1039/C4TA02984D>.
- (29) Ghosh, S.; Paul, B.; Chattopadhyay, N. Interaction of Cyclodextrins with Human and Bovine Serum Albumins: A Combined Spectroscopic and Computational Investigation. *J. Chem. Sci.* **2014**, *126*, 931–944. <https://doi.org/10.1007/s12039-014-0652-6>.

Chapter 5:

Cyclodextrin Metal-Organic Framework-Based Protein Biocomposites

This work appears in the following publication and has been re-formatted for this thesis:

Di Palma, G.; Geels, S.; Carpenter, B. P.; Talosig, A. R.; Chen, C.; Marangoni, F.; Patterson, J.P. Cyclodextrin Metal-Organic Framework-Based Protein Biocomposites. 2022. *Biomater. Sci.*, **10**, 6749-6754.

Chapter 5: Cyclodextrin Metal-Organic Framework-Based Protein Biocomposites

5.1 Introduction

Metal–organic framework-based protein biocomposites (p@MOFs) are extended crystalline materials where the protein is encapsulated within the ordered lattice of metal nodes and organic linkers.^{1–3} This material is in contrast to protein-metal–organic frameworks where the biomolecule is a part of the lattice.^{4,5} P@MOFs present an exciting opportunity for next-generation materials in biosensing,⁶ drug delivery,^{7–9} imaging,^{10,11} and cancer therapy^{12–16} due to the increased stability and activity of the encapsulated proteins.^{17–19} In general, MOFs have been widely studied as drug delivery materials due to their high drug loading,²⁰ and controllable drug release properties.^{21–23} A key factor when designing MOFs for drug delivery is the toxicity of the individual metal and ligand components.^{24,25} In 2010, Stoddart and coworkers created an “edible” MOF using gamma-cyclodextrin (γ -CD) and potassium or rubidium to form CD-MOF1 and CD-MOF2, respectively.²⁶ More recently CD-MOFs have been formed using α -CD²⁷ and β -CD.²⁸ These CD-MOFs have been investigated for applications in gas sensing,²⁹ enantiomeric separation,³⁰ catalysis,³¹ and small molecule drug delivery.³² CD-MOFs are especially attractive for drug delivery systems as they display low toxicity compared to other MOF linkers.³³ CD-MOFs should be ideal for the storage and delivery of therapeutic proteins as cyclodextrin-protein complexes display sustained drug delivery,^{34,35} reduced protein aggregation, and higher structural stability to physical perturbation.³⁶ In addition, cyclodextrins can induce the refolding of denatured proteins.³⁷

Furthermore, the importance of proteins being integrated with sugars is already represented in nature, where carbohydrates are incorporated into >50% of human proteins.³⁸ For this reason

there has been great interest in the development of new carbohydrate based drug delivery systems.^{39–41} However, to the best of our knowledge, biomolecule encapsulation inside CD-MOFs has not been demonstrated.^{32,42} The reason for this is likely because the original synthesis for CD-MOF1 requires a high pH environment (~ 13) and extended crystallization times (\sim several days);⁴² the combination of which would likely denature proteins. Another challenge when developing CD-MOFs for drug delivery is controlling their release profile.⁴³

Here, we develop a quick (several hours) and biofriendly (pH ~ 8.5) synthesis for CD-MOF1 and β -CD-MOF using potassium as the metal node. Protein encapsulation is demonstrated using bovine serum albumin (BSA), catalase, myoglobin, and interleukin-2.

5.2 Results and Discussion

CD-MOFs were synthesized by dissolving the precursors in pure water and inducing crystallization through the addition of a non-solvent. Methanol or acetonitrile were used as the non-solvent for γ - and β -CD-MOFs respectively. Encapsulation efficiency (EE%) for the protein@CD-MOFs was determined using the Bradford assay, which found the EE% for all proteins studied to be ~ 80 – 98% (Figure 5.1 and Table C1). During the last step of the synthesis, the CD-MOFs are centrifuged, separated from supernatant, and dried under a constant airflow inside 2 ml centrifugation tubes to form a compact pellet of approximately 1 cm in diameter (Figure 5.2g and 5.3g). Powder X-Ray Diffraction (PXRD) of the γ -CD-MOFs and protein@ γ -CD-MOFs showed peaks consistent with literature (Figure 5.2a),^{26,44} with a maximum d -spacing of ~ 2.2 nm (ESI Table D2). SEM images of BSA, myoglobin, and catalase γ -CD-MOFs showed

truncated cuboid crystals (Figure 5.2c-e). SEM images of interleukin-2@ γ -CD-MOFs showed rough spheroid crystals (Figure 5.2f).

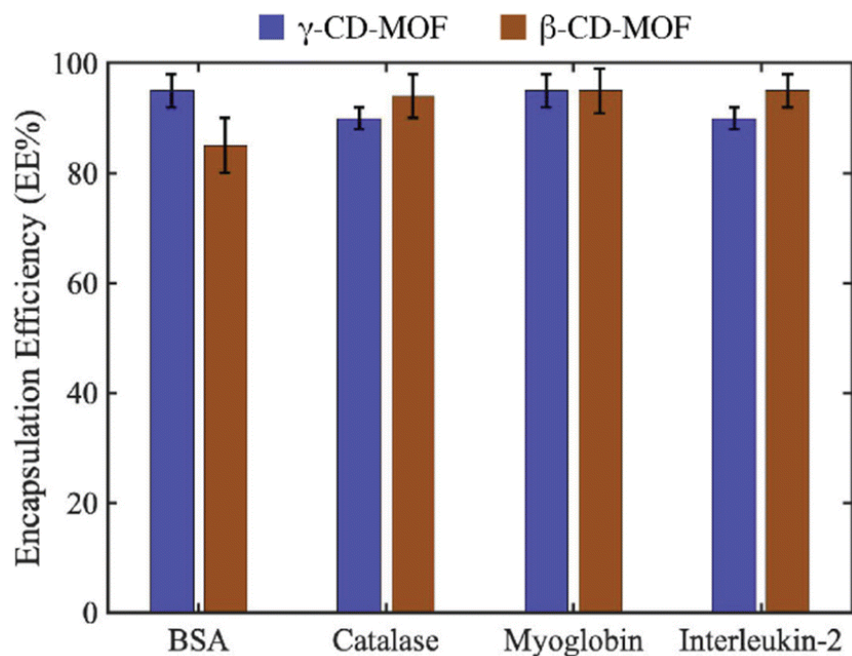


Figure 5.1 Encapsulation efficiency of BSA, catalase, myoglobin, and interleukin-2 for γ -CD-MOFs (blue) and β -CD-MOFs (brown). Error determined by triplicates.

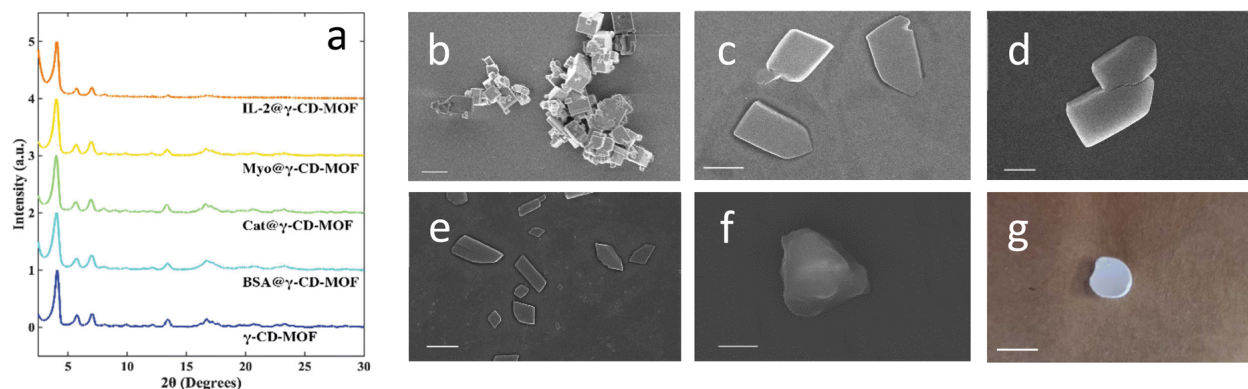


Figure 5.2 (a) PXRD of γ -CD-MOFs and SEM of (b) γ -CD-MOFs (c) BSA@ γ -CD-MOFs (d) catalase@ γ -CD-MOFs (e) myoglobin@ γ -CD-MOFs (f) interleukin-2@ γ -CD-MOFs. Scale bar: 2 μ m. (g) Pellet of protein@ γ -CD-MOFs. Scale bar: 1 cm.

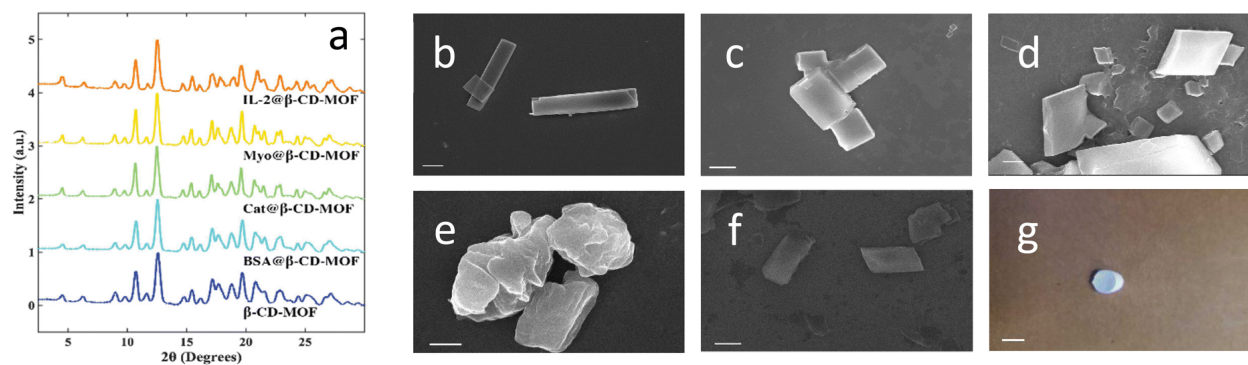


Figure 5.3 (a) PXRD of β -CD-MOFs and SEMs of (b) β -CD-MOFs (c) BSA@ β -CD-MOFs (d) catalase@ β -CD-MOF (e) myoglobin@ β -CD-MOFs (f) interleukin-2@ β -CD-MOFs. Scale bar: 2 μ m (g) pellet of protein@ β -CD-MOFs. Scale Bar: 1 cm.

PXRD of the protein- β -CD-MOFs showed peaks consistent with literature,⁴⁴ and a maximum d -spacing of ~ 2.0 nm (Figure 5.3a and Table C2). It is important to note that the XRD patterns are consistent regardless of the biomolecule used. This consistency occurs because proteins are entrapped into defects of the crystal lattice rather than altering the crystal lattice.^{17,45-48} SEM images of β -CD-MOFs and BSA@ β -CD-MOFs show cuboid crystals; SEM images of catalase and interleukin-2 β -CD-MOFs showed rhomboid crystals; and myoglobin β -CD-MOFs showed rough spheroid structures (Figure 5.3b-f). The collective SEM data reveals that incorporation of biomolecules into the CD-MOF synthesis affects the nucleation and growth mechanism resulting in different crystal morphologies, consistent with previous protein@MOFs studies.^{17,49} The solid pellets (Figure 5.2g and 5.3g) were considered optimal for a release profile study without further post-synthesis modification. The release profile was obtained for the BSA@ γ -CD-MOFs, BSA@ β -CD-MOFs, and a hybrid of BSA@ γ - β -CD-MOFs (γ : β 1 : 1) system (Figure 5.4). The hybrid BSA@ γ - β -CD-MOF was designed to examine the tunability of the protein release profile. SEM images of the hybrid of γ - β -CD-MOF showed a mixture of γ -

β -CD-MOF crystals and aggregates with irregular shapes (Figures C1 and C2). PXRD of the hybrid CD-MOF showed a low crystallinity compared to the CD-MOFs with only one type of organic linker. This indicates that mixing with more than one type of cyclodextrin could interfere with the extensivity of the crystal lattice. γ -CD-MOFs displayed the fastest release with full release being achieved within 10 minutes. β -CD-MOF displayed the slowest release profile with full release being achieved over \sim 24 hours. We hypothesize that the lower solubility of β -CD in water compared to γ -CD is the main factor between the difference in release profile.⁵⁰ The hybrid γ -/ β -CD-MOF pellet displayed an intermediate release profile indicating that the release profile can be tuned. Since it was possible to tune the release profile using the hybrid CD-MOF, we believe that the release profile is determined by the solvation of the outermost organic linkers. When solvated, the crystal structure breaks down which then liberates the encapsulated protein. To evaluate the protein@CD-MOFs as delivery systems, we tested the activity of the catalase@CD-MOFs and interleukin-2@CD-MOFs after dissolution. The activity of catalase@CD-MOFs was evaluated by comparing the catalytic activity with free catalase using the FOX assay (Figure 5.5).⁵¹ The data shows that after release, the catalase from the γ -CD-MOFs shows no activity; however, the catalase from the β -CD-MOFs has comparable activity to the free catalase. We hypothesize that the difference in activity is due to methanol weakening the hydrophobic interactions that form the tertiary structure of a protein. This deterioration of tertiary structure results in a loss of activity in the enzyme.^{52,53}

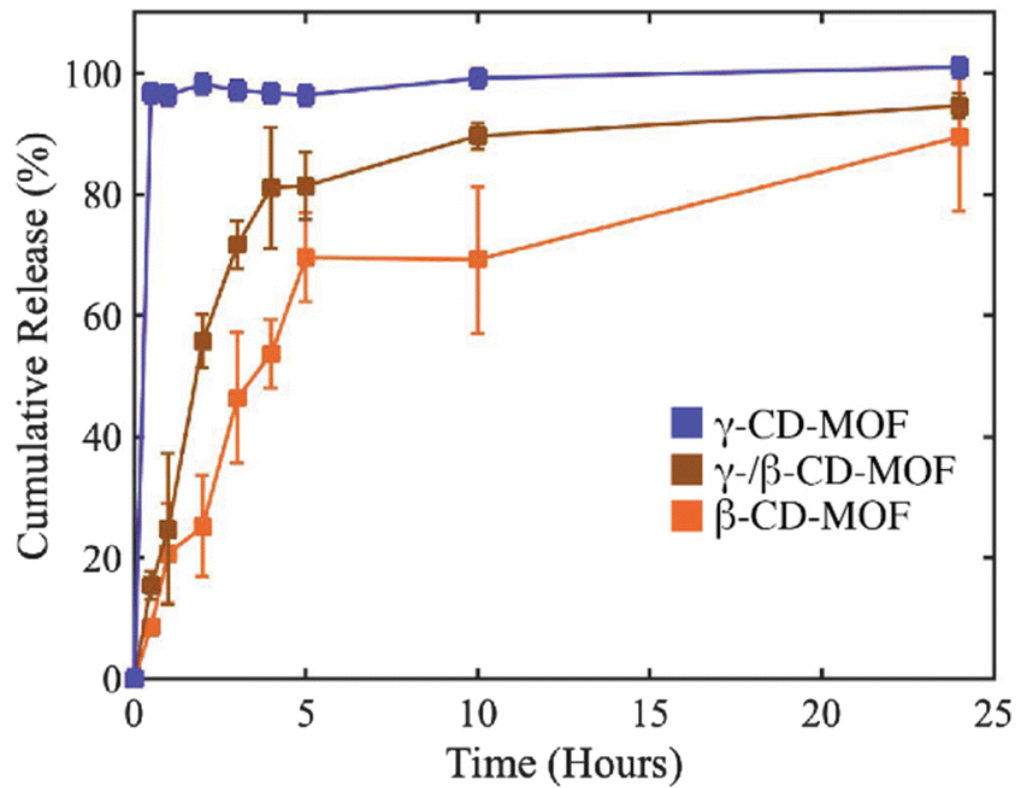


Figure 5.4 Release profiles of BSA encapsulated in β -CD-MOFs (blue), γ -/ β -CD-MOFs (brown), and γ -CD-MOFs (orange).

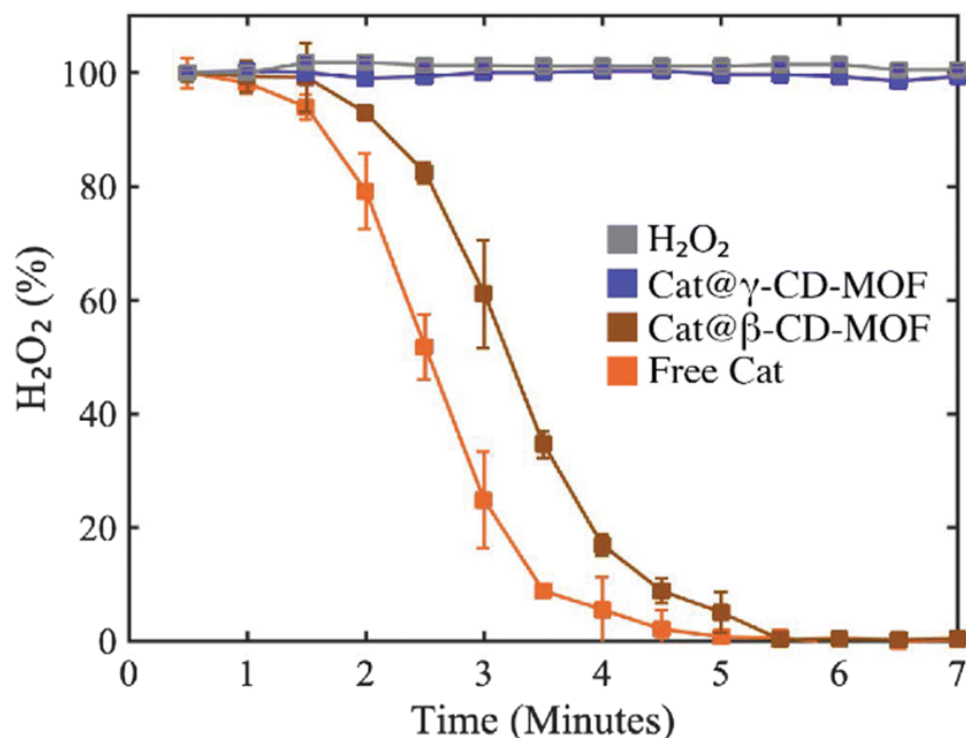


Figure 5.5 Catalytic assay of free catalase (orange), catalase encapsulated into β -CD-MOF (brown), catalase encapsulated into γ -CD-MOF (blue), and no catalase (gray). Stirring at 300 rpm was used in all solutions during the experiment.

5.3 Conclusions

In summary, we demonstrated the synthesis of cyclodextrin metal–organic framework-based protein biocomposites. Using different type of cyclodextrins, we have shown that the release profile can be tuned and the encapsulated proteins remain active after release from these materials. Encapsulation of catalase and interleukin-2 in γ -CD-MOF decreases their biological activity, while encapsulation in β -CD-MOF preserves it. We hypothesize that, during the synthesis of γ -CD-MOFs, methanol interferes and weakens hydrophobic interactions of the tertiary protein structures. Future p@CD-MOFs synthesis will focus on non-protic solvents as

non-solvents for crystallization. These results demonstrate the importance of developing a biofriendly method for encapsulating biomolecules within MOFs. Considering that during release, the proteins will be in a cyclodextrin-rich environment, we believe these materials are promising for the delivery of therapeutic proteins.

5.4 Methods

Materials

Chemical reagents for γ -CD-MOF and β -CD-MOF syntheses were obtained from several suppliers and used as received unless specifically indicated. γ -Cyclodextrin was bought from Fischer Scientific. β -Cyclodextrin, Potassium acetate, Bovine Serum Albumin, Catalase, Myoglobin from Sigma Aldrich. Interleukin-2 from Med Chem Express. Milli-Q water ($\rho > 18 \text{ M}\Omega \text{ cm}$) was used as the solvent for all aqueous solutions.

Synthesis of γ -CD-MOFs

γ -CD-MOFs were synthesized by mixing γ -Cyclodextrin (γ -CD) (283 mg, 0.22 mmol) with potassium acetate (170 mg 1.73 mmol) in 2 ml of Milli-Q water. Samples were then heated for 1 minute in an oven at 80 degrees and vortexed for 20 seconds or until complete dissolution was reached. The solutions were cooled down in a water bath at room temperature, put in a 15 ml centrifuge tube. 6 ml of methanol were added rapidly from a glass cylinder, and vortexed for 3 seconds. The solution was centrifuged at 10000 rpm for 10 minutes. The precipitate was separated from the solvent, washed with methanol, and centrifuged. For the drying process, the crystals were dried inside the centrifuge tube under airflow for 1-hour without using the vacuum. Synthesis resulted in a pellet of $\sim 1 \text{ cm}$ in diameter.

Synthesis of protein @ γ -CD-MOFs

Protein @ γ -CD-MOFs were synthesized by mixing γ -Cyclodextrin (γ -CD) (283 mg, 0.22 mmol) with potassium acetate (170 mg 1.73 mmol) in 2 ml of Milli-Q water. Samples were then heated for 1 minute in an oven at 80 degrees and vortexed for 20 seconds or until complete dissolution was reached. The solutions were cooled down in a water bath at room temperature, put in a 15 ml centrifuge tube. 4 mg of Bovine Serum Albumin was dissolved in 200 μ L Milli-Q water and added to the 15ml centrifuge tube. 6 ml of methanol were added rapidly from a glass cylinder, and vortexed for 3 seconds. The precipitate was then transferred to 2 ml centrifuge tube; the solution was then centrifuged at 10,000 rpm for 10 minutes; The precipitate was separated from the solvent, washed with fresh methanol, and centrifuged again under the same conditions. The crystals were dried inside the centrifuge tube under airflow for 1-hour, forming a pellet of 1 cm in diameter. The same synthesis was also repeated for Catalase and Myoglobin. Electronic Supplementary Material (ESI) for Biomaterials Science.

Synthesis of β -CD-MOFs

To synthesize β -CD-MOFs, β -cyclodextrin (β -CD) (100 mg, 0.08 mmol) and potassium acetate 60 mg (0.611 mmol) were added to 2 ml of Milli-Q water. The solution was left in the oven at 80 degrees until complete dissolution. The solution was cooled down in a bath at room temperature and transferred to a 15ml centrifuge tube. 6ml of acetonitrile was added, the solution was let to rest for several minutes and then vortexed. The solution was then centrifuged at 10,000 rpm for 10 minutes to obtain a precipitate. The precipitate was washed with fresh acetonitrile and centrifuged again under the same conditions. The crystals were dried inside the centrifuge tube under airflow for 1-hour, giving a pellet of 1 cm of diameter.

Synthesis of protein @ β -CD-MOFs

β -CD (100mg, 0.089 mmol) was added with potassium acetate (60 mg, 0.61 mmol) in 2 ml of Milli-Q water. The solution was left in the oven at 80 degrees until complete dissolution. The solution was cooled down in a bath at room temperature and transferred to a 15ml centrifuge tube. 4 mg of Bovine Serum Albumin was dissolved in 200 μ L of Milli-Q water and added to the β -CD/acetate mixture. After one hour, 6 ml of acetonitrile was added, let it rest for 5 minutes, and vortexed for 3 seconds following the addition. The solution was centrifuged at 10,000 rpm for 10 minutes to obtain a precipitate. The precipitate was washed with fresh acetonitrile and centrifuged again under the same conditions. The crystals were dried inside the centrifuge tube under airflow for 1-hour, giving a pellet of 1 cm of diameter. The same synthesis was also repeated for 4 mg Catalase and 4 mg Myoglobin.

Synthesis of BSA @ γ - / β -CD-MOF

β -CD (100mg, 0.09 mmol) and γ -CD (110mg, 0.09 mmol) were added with potassium acetate (130 mg, 1.4 mmol) in 2 ml of Milli-Q water. The solution was left in the oven at 80 degrees until complete dissolution. The solution was cooled down in a bath at room temperature and transferred to a 15ml centrifuge tube. 4 mg of Bovine Serum Albumin was dissolved in 200 μ L of Milli-Q water and added to the γ - / β -CD/acetate mixture. 6 ml of acetonitrile was added, and the solution was let to rest for several minutes and then vortexed. The solution was then centrifuged at 10,000 rpm for 10 minutes to obtain a precipitate. The precipitate was washed with fresh acetonitrile and centrifuged again under the same conditions. The crystals were dried inside the centrifuge tube under airflow for 1-hour.

Encapsulation Efficiency

Encapsulation Efficiency was determined for BSA, Catalase, Myoglobin, and Interleukin-2 in each MOF by measuring the concentration of protein in the supernatants. For BSA, Catalase and Myoglobin MOFs, supernatants were separated from the solids and concentrated using a rotavap. An aliquot of 20 μL was taken from the concentrated supernatant and mixed into a solution of 980 μL Bradford reagent 1x (standard assay). Absorbance measurements were obtained from each sample at 595nm using a NanoDrop™ 2000. Concentrations were calculated using calibration curves for each protein. For myoglobin, the encapsulation efficiency was determined directly by measuring the absorbance of the supernatant at 408 nm. For interleukin2, the supernatant was concentrated with a centrifugal filter (Amicon Ultra 0.5 ml, MWCO 30K) and diluted to 150 μL . The 150 μL of supernatant was mixed with 150 μL of Bradford reagent (Microassay), and the absorbance at 595nm was analyzed with a NanoDrop™ 2000 using myoglobin as the standard.

SEM

Samples were prepared by pipetting 10 μL of sample onto 1mm thick glass slides which were then coated with 5nm Iridium (Quorum Q150T) to reduce charging. Samples were imaged with a Magellan 400 XRH system with secondary electron images taken at an accelerating current ranging from 2-3 keV.

5.5 Acknowledgements

This research was supported by the University of California Cancer Research Coordinating Committee Grant C21CR2080 (to J. P) and C22CR4114 (to F. M.).

The authors acknowledge the use of facilities and instrumentation at the UC Irvine Materials Research Institute (IMRI), which is supported in part by the National Science Foundation through the UC Irvine Materials Research Science and Engineering Center (DMR-2011967) as well as the UCI laser spectroscopy lab (chem.uci.edu/~dmitryf/index.html). The authors wish to acknowledge the support of the Chao Family Comprehensive Cancer Center/UCI Institute for Immunology Flow Cytometry Facility (<https://sites.uci.edu/ififlowcore/>), supported by the NCI/NIH under award number P30CA062203.

5.6 References

- (1) Liang, W.; Wied, P.; Carraro, F.; Sumbly, C. J.; Nidetzky, B.; Tsung, C.-K.; Falcaro, P.; Doonan, C. J. Metal–Organic Framework-Based Enzyme Biocomposites. *Chem. Rev.* **2021**, *121* (3), 1077–1129. <https://doi.org/10.1021/acs.chemrev.0c01029>.
- (2) Doonan, C.; Riccò, R.; Liang, K.; Bradshaw, D.; Falcaro, P. Metal–Organic Frameworks at the Biointerface: Synthetic Strategies and Applications. *Acc. Chem. Res.* **2017**, *50* (6), 1423–1432. <https://doi.org/10.1021/acs.accounts.7b00090>.
- (3) Zou, D.; Yu, L.; Sun, Q.; Hui, Y.; Tengjisi; Liu, Y.; Yang, G.; Wibowo, D.; Zhao, C.-X. A General Approach for Biomimetic Mineralization of MOF Particles Using Biomolecules. *Colloids Surf. B Biointerfaces* **2020**, *193*, 111108. <https://doi.org/10.1016/j.colsurfb.2020.111108>.
- (4) Bailey, J. B.; Tezcan, F. A. Tunable and Cooperative Thermomechanical Properties of Protein–Metal–Organic Frameworks. *J. Am. Chem. Soc.* **2020**, *142* (41), 17265–17270. <https://doi.org/10.1021/jacs.0c07835>.
- (5) Sontz, P. A.; Bailey, J. B.; Ahn, S.; Tezcan, F. A. A Metal Organic Framework with Spherical Protein Nodes: Rational Chemical Design of 3D Protein Crystals. *J. Am. Chem. Soc.* **2015**, *137* (36), 11598–11601. <https://doi.org/10.1021/jacs.5b07463>.

- (6) Cui, J.; Gao, N.; Yin, X.; Zhang, W.; Liang, Y.; Tian, L.; Zhou, K.; Wang, S.; Li, G. Microfluidic Synthesis of Uniform Single-Crystalline MOF Microcubes with a Hierarchical Porous Structure. *Nanoscale* **2018**, *10* (19), 9192–9198. <https://doi.org/10.1039/C8NR01219A>.
- (7) Chen, T.-T.; Yi, J.-T.; Zhao, Y.-Y.; Chu, X. Biomaterialized Metal–Organic Framework Nanoparticles Enable Intracellular Delivery and Endo-Lysosomal Release of Native Active Proteins. *J. Am. Chem. Soc.* **2018**, *140* (31), 9912–9920. <https://doi.org/10.1021/jacs.8b04457>.
- (8) Simon-Yarza, T.; Mielcarek, A.; Couvreur, P.; Serre, C. Nanoparticles of Metal–Organic Frameworks: On the Road to In Vivo Efficacy in Biomedicine. *Adv. Mater.* **2018**, *30* (37), 1707365. <https://doi.org/10.1002/adma.201707365>.
- (9) Cases Díaz, J.; Lozano-Torres, B.; Giménez-Marqués, M. Boosting Protein Encapsulation through Lewis-Acid-Mediated Metal–Organic Framework Mineralization: Toward Effective Intracellular Delivery. *Chem. Mater.* **2022**, *34* (17), 7817–7827. <https://doi.org/10.1021/acs.chemmater.2c01338>.
- (10) Zhang, J.; He, M.; Nie, C.; He, M.; Pan, Q.; Liu, C.; Hu, Y.; Yi, J.; Chen, T.; Chu, X. Biomaterialized Metal–Organic Framework Nanoparticles Enable Enzymatic Rolling Circle Amplification in Living Cells for Ultrasensitive MicroRNA Imaging. *Anal. Chem.* **2019**, *91* (14), 9049–9057. <https://doi.org/10.1021/acs.analchem.9b01343>.
- (11) Horcajada, P.; Chalati, T.; Serre, C.; Gillet, B.; Sebrie, C.; Baati, T.; Eubank, J. F.; Heurtaux, D.; Clayette, P.; Kreuz, C.; Chang, J.-S.; Hwang, Y. K.; Marsaud, V.; Bories, P.-N.; Cynober, L.; Gil, S.; Férey, G.; Couvreur, P.; Gref, R. Porous Metal–Organic-Framework Nanoscale Carriers as a Potential Platform for Drug Delivery and Imaging. *Nat. Mater.* **2010**, *9* (2), 172–178. <https://doi.org/10.1038/nmat2608>.
- (12) Zhao, Q.; Gong, Z.; Li, Z.; Wang, J.; Zhang, J.; Zhao, Z.; Zhang, P.; Zheng, S.; Miron, R. J.; Yuan, Q.; Zhang, Y. Target Reprogramming Lysosomes of CD8⁺ T Cells by a Mineralized Metal–Organic Framework for Cancer Immunotherapy. *Adv. Mater.* **2021**, *33* (17), 2100616. <https://doi.org/10.1002/adma.202100616>.
- (13) Ni, K.; Luo, T.; Nash, G. T.; Lin, W. Nanoscale Metal–Organic Frameworks for Cancer Immunotherapy. *Acc. Chem. Res.* **2020**, *53* (9), 1739–1748. <https://doi.org/10.1021/acs.accounts.0c00313>.
- (14) Lu, K.; He, C.; Guo, N.; Chan, C.; Ni, K.; Weichselbaum, R. R.; Lin, W. Chlorin-Based Nanoscale Metal–Organic Framework Systemically Rejects Colorectal Cancers via Synergistic Photodynamic Therapy and Checkpoint Blockade Immunotherapy. *J. Am. Chem. Soc.* **2016**, *138* (38), 12502–12510. <https://doi.org/10.1021/jacs.6b06663>.
- (15) Li, Q.; Liu, Y.; Zhang, Y.; Jiang, W. Immunogenicity-Boosted Cancer Immunotherapy Based on Nanoscale Metal–Organic Frameworks. *J. Controlled Release* **2022**, *347*, 183–198. <https://doi.org/10.1016/j.jconrel.2022.05.003>.
- (16) Jin, S.; Weng, L.; Li, Z.; Yang, Z.; Zhu, L.; Shi, J.; Tang, W.; Ma, W.; Zong, H.; Jiang, W. Nanoscale Dual-Enzyme Cascade Metal–Organic Frameworks through Biomimetic Mineralization as ROS Generators for Synergistic Cancer Therapy. *J. Mater. Chem. B* **2020**, *8* (21), 4620–4626. <https://doi.org/10.1039/D0TB00357C>.
- (17) Liang, K.; Ricco, R.; Doherty, C. M.; Styles, M. J.; Bell, S.; Kirby, N.; Mudie, S.; Haylock, D.; Hill, A. J.; Doonan, C. J.; Falcaro, P. Biomimetic Mineralization of Metal–Organic Frameworks as Protective Coatings for Biomacromolecules. *Nat. Commun.* **2015**, *6* (1), 7240. <https://doi.org/10.1038/ncomms8240>.

- (18) Wei, T.-H.; Wu, S.-H.; Huang, Y.-D.; Lo, W.-S.; Williams, B. P.; Chen, S.-Y.; Yang, H.-C.; Hsu, Y.-S.; Lin, Z.-Y.; Chen, X.-H.; Kuo, P.-E.; Chou, L.-Y.; Tsung, C.-K.; Shieh, F.-K. Rapid Mechanochemical Encapsulation of Biocatalysts into Robust Metal–Organic Frameworks. *Nat. Commun.* **2019**, *10* (1), 5002. <https://doi.org/10.1038/s41467-019-12966-0>.
- (19) Majewski, M. B.; Howarth, A. J.; Li, P. Enzyme encapsulation in metal–organic frameworks for applications in catalysis, *CrystEngComm.* **2017**, *19*, 4082–4091. <https://pubs.rsc.org/en/content/articlelanding/2017/ce/c7ce00022g>
- (20) Wuttke, S.; Lismont, M.; Escudero, A.; Rungtaweeworanit, B.; Parak, W. J. Positioning Metal–Organic Framework Nanoparticles within the Context of Drug Delivery – A Comparison with Mesoporous Silica Nanoparticles and Dendrimers. *Biomaterials* **2017**, *123*, 172–183. <https://doi.org/10.1016/j.biomaterials.2017.01.025>.
- (21) Sindoro, M.; Yanai, N.; Jee, A.-Y.; Granick, S. Colloidal-Sized Metal–Organic Frameworks: Synthesis and Applications. *Acc. Chem. Res.* **2014**, *47* (2), 459–469. <https://doi.org/10.1021/ar400151n>.
- (22) Horcajada, P.; Gref, R.; Baati, T.; Allan, P. K.; Maurin, G.; Couvreur, P.; Férey, G.; Morris, R. E.; Serre, C. Metal–Organic Frameworks in Biomedicine. *Chem. Rev.* **2012**, *112* (2), 1232–1268. <https://doi.org/10.1021/cr200256v>.
- (23) Cai, W.; Gao, H.; Chu, C.; Wang, X.; Wang, J.; Zhang, P.; Lin, G.; Li, W.; Liu, G.; Chen, X. Engineering Phototheranostic Nanoscale Metal–Organic Frameworks for Multimodal Imaging-Guided Cancer Therapy. *ACS Appl. Mater. Interfaces* **2017**, *9* (3), 2040–2051. <https://doi.org/10.1021/acsami.6b11579>.
- (24) Tamames-Tabar, C.; Cunha, D.; Imbuluzqueta, E.; Ragon, F.; Serre, C.; Blanco-Prieto, M. J.; Horcajada, P. Cytotoxicity of Nanoscaled Metal–Organic Frameworks. *J. Mater. Chem. B* **2013**, *2* (3), 262–271. <https://doi.org/10.1039/C3TB20832J>.
- (25) Ettlinger, R.; Lächelt, U.; Gref, R.; Horcajada, P.; Lammers, T.; Serre, C.; Couvreur, P.; Morris, R. E.; Wuttke, S. Toxicity of Metal–Organic Framework Nanoparticles: From Essential Analyses to Potential Applications. *Chem. Soc. Rev.* **2022**, *51* (2), 464–484. <https://doi.org/10.1039/D1CS00918D>.
- (26) Smaldone, R. A.; Forgan, R. S.; Furukawa, H. Metal–Organic Frameworks from Edible Natural Products *Angew. Chem. Int. Ed.* **2010**, *49*, 8630–8634 <https://doi.org/10.1002/anie.201002343>
- (27) Sha, J.; Yang, X.; Sun, L.; Zhang, X.; Li, S.; Li, J.; Sheng, N. Unprecedented α -Cyclodextrin Metal–Organic Frameworks with Chirality: Structure and Drug Adsorptions. *Polyhedron* **2017**, *127*, 396–402. <https://doi.org/10.1016/j.poly.2016.10.012>.
- (28) Liu, J.; Bao, T.-Y.; Yang, X.-Y.; Zhu, P.-P.; Wu, L.-H.; Sha, J.-Q.; Zhang, L.; Dong, L.-Z.; Cao, X.-L.; Lan, Y.-Q. Controllable Porosity Conversion of Metal–Organic Frameworks Composed of Natural Ingredients for Drug Delivery. *Chem. Commun.* **2017**, *53* (55), 7804–7807. <https://doi.org/10.1039/C7CC03673F>.
- (29) Gassensmith, J. J.; Kim, J. Y.; Holcroft, J. M.; Farha, O. K.; Stoddart, J. F.; Hupp, J. T.; Jeong, N. C. A Metal–Organic Framework-Based Material for Electrochemical Sensing of Carbon Dioxide. *J. Am. Chem. Soc.* **2014**, *136* (23), 8277–8282. <https://doi.org/10.1021/ja5006465>.

- (30) Xu, W.; Li, X.; Wang, L.; Li, S.; Chu, S.; Wang, J.; Li, Y.; Hou, J.; Luo, Q.; Liu, J. Design of Cyclodextrin-Based Functional Systems for Biomedical Applications. *Front. Chem.* **2021**, *9*. <https://doi.org/10.3389/fchem.2021.635507>.
- (31) Han, S.; Wei, Y.; Grzybowski, B. A. A Metal–Organic Framework Stabilizes an Occluded Photocatalyst. *Chem. – Eur. J.* **2013**, *19* (34), 11194–11198. <https://doi.org/10.1002/chem.201302141>.
- (32) Roy, I.; Stoddart, J. F. Cyclodextrin Metal–Organic Frameworks and Their Applications. *Acc. Chem. Res.* **2021**, *54* (6), 1440–1453. <https://doi.org/10.1021/acs.accounts.0c00695>.
- (33) Abuçafy, M. P.; Caetano, B. L.; Chiari-Andréo, B. G.; Fonseca-Santos, B.; do Santos, A. M.; Chorilli, M.; Chiavacci, L. A. Supramolecular Cyclodextrin-Based Metal–Organic Frameworks as Efficient Carrier for Anti-Inflammatory Drugs. *Eur. J. Pharm. Biopharm.* **2018**, *127*, 112–119. <https://doi.org/10.1016/j.ejpb.2018.02.009>.
- (34) Sivasubramanian, M.; Thambi, T.; Park, J. H. Mineralized Cyclodextrin Nanoparticles for Sustained Protein Delivery. *Carbohydr. Polym.* **2013**, *97* (2), 643–649. <https://doi.org/10.1016/j.carbpol.2013.05.018>.
- (35) Chen, K.; He, S.; Wang, H.; Zhang, S.; Yu, L.; Zhang, Y.; Elshazly, E. H.; Ke, L.; Gong, R. Ionic Gelated β -Cyclodextrin-Biotin-Carboxymethyl Chitosan Nanoparticles Prepared as Carrier for Oral Delivery of Protein Drugs. *J. Polym. Eng.* **2020**, *40* (5), 440–447. <https://doi.org/10.1515/polyeng-2019-0137>.
- (36) Goszczyński, T. M.; Gawłowski, M.; Girek, B.; Kowalski, K.; Boratyński, J.; Girek, T. Synthesis of β -Cyclodextrin-Lysozyme Conjugates and Their Physicochemical and Biochemical Properties. *J. Incl. Phenom. Macrocycl. Chem.* **2017**, *87* (3), 341–348. <https://doi.org/10.1007/s10847-017-0706-8>.
- (37) Zhang, L.; Zhang, Q.; Wang, C. Refolding of Detergent-Denatured Lysozyme Using β -Cyclodextrin-Assisted Ion Exchange Chromatography. *Biomed. Chromatogr.* **2013**, *27* (3), 365–370. <https://doi.org/10.1002/bmc.2800>.
- (38) An, H. J.; Froehlich, J. W.; Lebrilla, C. B. Determination of Glycosylation Sites and Site-Specific Heterogeneity in Glycoproteins. *Curr. Opin. Chem. Biol.* **2009**, *13* (4), 421–426. <https://doi.org/10.1016/j.cbpa.2009.07.022>.
- (39) Di, X.; Liang, X.; Shen, C.; Pei, Y.; Wu, B.; He, Z. Carbohydrates Used in Polymeric Systems for Drug Delivery: From Structures to Applications. *Pharmaceutics* **2022**, *14* (4), 739. <https://doi.org/10.3390/pharmaceutics14040739>.
- (40) Liu, K.; Jiang, X.; Hunziker, P. Carbohydrate-based amphiphilic nano delivery systems for cancer therapy. *Nanoscale*, **2016**, *8*, 16091–1615. <https://doi.org/10.1039/C6NR04489A>.
- (41) Fathi, M.; Martín, Á.; McClements, D. J. Nanoencapsulation of Food Ingredients Using Carbohydrate Based Delivery Systems. *Trends Food Sci. Technol.* **2014**, *39* (1), 18–39. <https://doi.org/10.1016/j.tifs.2014.06.007>.
- (42) Rajkumar, T.; Kukkar, D.; Kim, K.-H.; Sohn, J. R.; Deep, A. Cyclodextrin-Metal–Organic Framework (CD-MOF): From Synthesis to Applications. *J. Ind. Eng. Chem.* **2019**, *72*, 50–66. <https://doi.org/10.1016/j.jiec.2018.12.048>.
- (43) Li, H.; Lv, N.; Li, X.; Liu, B.; Feng, J.; Ren, X.; Guo, T.; Chen, D.; Stoddart, J. F.; Gref, R.; Zhang, J. Composite CD-MOF Nanocrystals-Containing Microspheres for Sustained Drug Delivery. *Nanoscale* **2017**, *9* (22), 7454–7463. <https://doi.org/10.1039/C6NR07593B>.

- (44) Xiong, Y.; Wu, L.; Guo, T.; Wang, C.; Wu, W.; Tang, Y.; Xiong, T.; Zhou, Y.; Zhu, W.; Zhang, J. Crystal Transformation of β -CD-MOF Facilitates Loading of Dimercaptosuccinic Acid. *AAPS PharmSciTech* **2019**, *20* (6), 224. <https://doi.org/10.1208/s12249-019-1422-z>.
- (45) Jia, Y.; Wei, B.; Duan, R.; Zhang, Y.; Wang, B.; Hakeem, A.; Liu, N.; Ou, X.; Xu, S.; Chen, Z.; Lou, X.; Xia, F. Imparting Biomolecules to a Metal-Organic Framework Material by Controlled DNA Tetrahedron Encapsulation. *Sci. Rep.* **2014**, *4* (1), 5929. <https://doi.org/10.1038/srep05929>.
- (46) Wang, D.; Chen, Y.; Wang, S. DNA-Functionalized Metal–Organic Framework Nanoparticles for Intracellular Delivery of Proteins *J. Am. Chem. Soc.* **2019**, *141*, 6, 2215–2219 <https://doi.org/10.1021/jacs.8b12705>
- (47) Chen, Y.; Li, P.; Modica, J. A.; Drout, R. J.; Farha, O. K. Acid-Resistant Mesoporous Metal–Organic Framework toward Oral Insulin Delivery: Protein Encapsulation, Protection, and Release. *J. Am. Chem. Soc.* **2018**, *140* (17), 5678–5681. <https://doi.org/10.1021/jacs.8b02089>.
- (48) Sun, Y.; Zheng, L.; Yang, Y.; Qian, X.; Fu, T.; Li, X.; Yang, Z.; Yan, H.; Cui, C.; Tan, W. Metal–Organic Framework Nanocarriers for Drug Delivery in Biomedical Applications. *Nano-Micro Lett.* **2020**, *12* (1), 103. <https://doi.org/10.1007/s40820-020-00423-3>.
- (49) Ogata, A.; Rakowski, A.; Carpenter, B.; Fishman, D. Direct Observation of Amorphous Precursor Phases in the Nucleation of Protein–Metal–Organic Frameworks *J. Am. Chem. Soc.*, 2020, **142**, 1433–1442 <https://pubs.acs.org/doi/abs/10.1021/jacs.9b11371>
- (50) Semalty, A. Cyclodextrin and Phospholipid Complexation in Solubility and Dissolution Enhancement: A Critical and Meta-Analysis. *Expert Opin. Drug Deliv.* **2014**, *11* (8), 1255–1272. <https://doi.org/10.1517/17425247.2014.916271>.

Appendix C:
Supplementary Information for Chapter 5

Appendix C: Supplementary Information for Chapter 5

C.1 Encapsulation Efficiency

	BSA	Catalase	Myoglobin	Interleukin-2
γ -CD-MOFs:	95% \pm 3%	90% \pm 2%	95% \pm 3%	90% \pm 2%
β -CD-MOFs:	85% \pm 5%	94% \pm 4%	95% \pm 4%	95% \pm 3%

Table C.1 Encapsulation Efficiency of BSA, Catalase, Myoglobin, and Interleukin-2 in γ -CD-MOFs and β -CD-MOFs.

C.2 Structural Characterization

Samples analyzed by SEM were sputter-coated with \sim 5 nm of iridium (Quorum Q150T) and imaged by an FEI Magellan 400 XHR system. Secondary electron images were acquired with an accelerating voltage of 10 kV, using a lens detector operating in immersion mode. Using an Ultima X-ray diffractometer, PXRD patterns were acquired using X-rays generated at 40 kV and 44 mA with Cu K α irradiation.

No.	2-theta γ -CD-MOF	d-spacing (ang.)	2-theta β -CD-MOFs	d-spacing (ang.)
1	4.040(7)	21.85(4)	4.469(13)	19.76(6)
2	5.680(5)	15.547(13)	6.123(4)	14.423(11)
3	6.970(5)	12.672(9)	8.865(12)	9.966(14)
4	8.020(9)	11.015(13)	9.718(16)	9.093(15)
5	8.960(10)	9.862(11)	10.622(4)	8.322(3)
6	9.86(3)	8.96(2)	11.462(8)	7.714(6)
7	11.430(14)	7.735(9)	12.396(13)	7.135(7)
8	12.030(12)	7.351(8)	12.561(4)	7.041(2)
9	13.370(5)	6.617(2)	14.622(10)	6.053(4)
10	16.240(18)	5.454(6)	15.308(7)	5.783(3)
11	16.640(11)	5.323(4)	16.040(18)	5.521(6)
12	17.040(19)	5.199(6)	16.77(3)	5.282(8)
13	17.51(4)	5.061(10)	17.009(8)	5.208(3)
14	18.360(19)	4.828(5)	17.416(12)	5.088(4)
15	19.62(2)	4.521(5)	17.710(17)	5.004(5)
16	20.600(12)	4.308(3)	18.022(13)	4.918(3)
17	21.030(17)	4.221(3)	18.562(12)	4.776(3)
18	22.530(12)	3.943(2)	18.92(2)	4.686(6)
19	23.180(18)	3.834(3)	19.552(11)	4.536(3)
20	23.950(17)	3.713(3)	20.544(17)	4.320(4)
21	26.13(4)	3.408(6)	20.99(6)	4.228(12)

Table C.2 d-spacing of γ -CD-MOF and β -CD-MOF, obtained from the PXRD analysis.

Chapter 6:
Risk Assessment and Mental Health Awareness
in Chemical Laboratory Settings

Chapter 6 Risk Assessment and Mental Health Awareness in Chemical Laboratories

Settings

6.1 Introduction

Ensuring laboratory safety is extremely important, requiring thorough management of potential risks. The risks associated with working in a chemical laboratory are numerous and can pose a significant threat to the safety of the researchers. Workplace accidents are one of the leading causes of both death and disabilities, and it is essential to continuously assess and mitigate the risks associated with lab work.¹ The most common hazards in chemistry labs include chemical exposure, fire risks, equipment malfunction, electrical hazards, and ergonomic strain.²

The University of California system has been a leader in laboratory safety regulations, partly driven by the tragic accident at UCLA involving Serri Sangji. In 2008, Sangji was fatally injured in a lab accident where she was using pyrophoric material that spontaneously ignited when exposed to air.³ This accident highlighted the need for improved safety protocols and a more robust safety culture in academic labs and higher education. As a result, the University of California system and the larger chemistry community have prioritized safety, leading efforts to prevent similar accidents and to ensure that researchers have safe working conditions.

The safety of graduate chemical labs can be challenging to monitor. This is primarily due to the underreported safety statistics compared to industrial chemistry labs.^{4,5} This lack of reporting leads to insufficient identification of common hazards, which makes it crucial to prioritize lab safety training and proactive risk management.⁶ Within a safe working environment, researchers can focus on their scientific advances and less on accidents, injuries, or

equipment damage.^{7,8} Safety training offers a standardized foundation for researchers to understand fundamental lab safety principles and learn how to minimize risk.

In this chapter, I will discuss the initiatives I led to enhance lab safety training within my research group, focusing on risk analysis. By recognizing the importance of a proactive approach to laboratory safety, I aimed to create a culture of safety awareness and accountability. I equipped researchers with the knowledge and skills to identify and mitigate potential hazards through risk assessments, training sessions, and open discussions. In addition, I will explore the critical role of mental health in researchers' overall well-being and its impact on the safety of an academic research environment. As the academic community advances, it is essential to acknowledge the emotional and psychological toll that graduate research can take on individuals. By examining the intersection of mental health awareness and lab safety, it can be better understood how a supportive and inclusive research culture can contribute to higher productivity and the well-being of researchers. I aim to share our experiences, successes, and challenges in enhancing lab safety training and promoting mental health awareness within our research group.

6.2 Risk Assessment

RAMP

RAMP stands for (R) recognize hazards, (A) assess risk, (M) minimize risk, and (P) prepare for emergencies. This system was introduced in 2010 and has been developed and improved by many safety communities, including the American Chemical Society (ACS).⁹ ACS describes RAMP as a tool that is "simple, structured, flexible, scalable, collaborative, and transferrable." This system can identify risks when starting a new experimental procedure or reevaluating a procedure that may be common and useful to researchers and safety professionals.

Implementing RAMP principles can help prevent accidents, reduce injuries, and promote an open and honest culture of safety in the lab. The steps are laid out below:

Recognize. The first step is recognizing hazards associated with an experiment. These hazards can come from chemicals, reaction conditions, or the use of equipment. For most chemicals, it is easy to identify their hazards through resources such as safety data sheets (SDS) and the Globally Harmonized System of Classification and Labeling of Chemicals (GHS).¹⁰ GHS labels are available on all chemical containers as pictograms and hazard statements. In addition, National Fire Protection Association (NFPA) fire diamonds are used to identify fire hazards.

Assessing Risk. Assessing the Risk of the hazards in an experimental setup can be difficult and requires careful consideration and judgment skills learned over time. This step can also be confusing because the definition of hazard and risk can be easily confused. A hazard can cause harm; the risk is the possibility of harm when exposed. Risk assessments are typically carried out using consequence value charts (CV) (Figure 6.1) and assess the risks to personal safety, resources, work performance, property damage, and reputation on a scale of low risk (1) to high risk (20). This results in a number value for risk exposure ranging from 5, almost no risk, to 100, very hazardous.

Consequence Value (CV)		Impact to...				
Rating	Value	Personnel Safety	Resources	Work Performance	Property Damage	Reputation
No Risk	1	No injuries	No impact	No delays	Minor	No impact
Minor	5	Minor injuries	Moderate impact	Modest delays	Moderate	Potential damage
Moderate	10	Moderate to life impacting injuries	Additional resources required	Significant delays	Substantial	Damaged
High	20	Life threatening injuries from single exposure	Institutional resources required	Major operational disruptions	Severe	Loss of confidence

Figure 6.1 The Consequence Value Chart is used to determine a hazard's impact on different aspects of an experiment, such as personal safety, resources, work performance, property damage, and reputation.

Minimizing Risk. When the hazards associated with an experiment and the risks are identified, the next step is to assess if any of the hazards can be minimized. Risk minimization can be performed by consulting with the Hierarchy of Controls¹¹, which shows the most effective steps for minimization at the top and the least effective at the bottom (Figure 6.2). The ideal way to deal with a hazard is to eliminate it, but that is not always an option. Another way to eliminate hazards is to lower the volume in which you are using the hazard so that if there is an accident, it will not be as severe. Substitution is another viable method of risk minimization where a less hazardous material can substitute the hazardous material.

Engineering controls ensure that the equipment used is in working order and is used properly. Administrative controls apply to many lab areas, including safety training before using a new hazard class or instrument and lab rules like not eating or drinking in lab areas. These are

often in the form of standard operating procedures (SOPs). PPE is the final defense against hazards and is listed at the bottom of the pyramid because it should be utilized whenever a lab procedure is implemented.

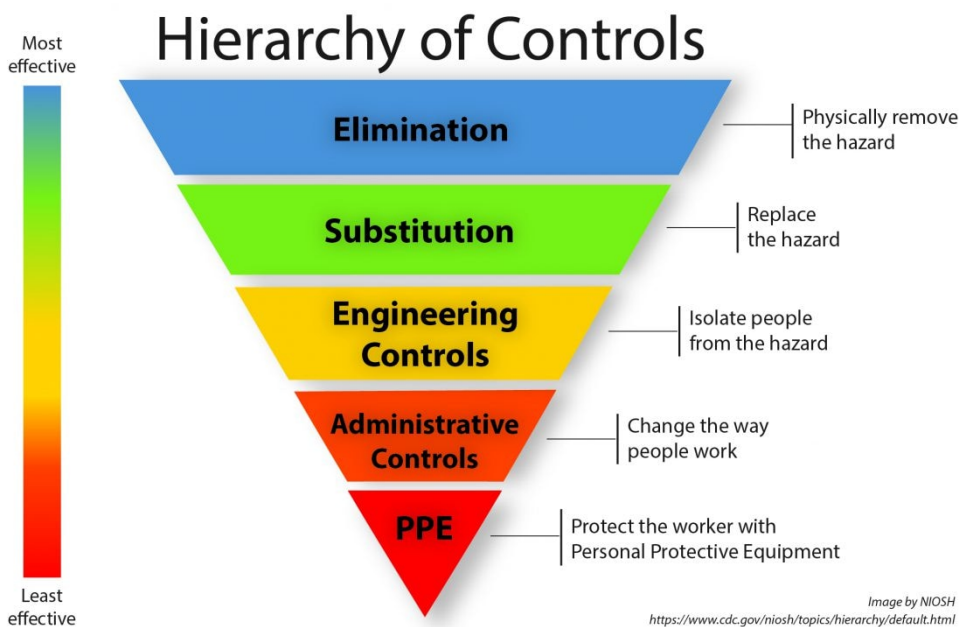


Figure 6.2 Hierarchy of Controls used to minimize risk in experimental procedures. Image from NIOSH.

Preparing for Emergencies. Although RAMP can minimize the chance of accidents, it cannot account for all possible accidents, so it is essential to be prepared for emergencies. This can include developing emergency response plans, practicing regular drills and training, and ensuring that all researchers know what to do in case of an emergency. Preparation for emergencies and this plan being well rehearsed can prevent minor incidents from becoming major disasters and can reduce the severity of injuries and damage. By prioritizing preparation for emergencies, labs can create a safer and more resilient work environment for all involved.

Implementing RAMP

To implement RAMP training in our lab, I shared the knowledge I gained from an ACS workshop and challenged each researcher to apply the assessment to an aspect of their project. When the time came for each researcher to present their findings, these RAMP presentations focused on common hazards such as cryogenics, peroxide formers, and standard synthetic setups (Figure 6.3). However, as we continued these presentations, our group members became increasingly creative, discussing less predictable topics. These topics included things such as internet safety and phishing (Figure 6.4).

One example of a researcher going beyond the typical RAMP framework was a presentation by Paul Hurst on glove box operation (Figure 6.5). In his presentation, he detailed multiple CV calculations and the risks associated with multiple types of hazards. These hazards included electrical issues, leaks from the glove box, and mechanical failures, and discussed how each one could impact researcher safety.

The RAMP presentations catalyzed our lab's safety culture, allowing open communication and sparking the revision of many of our standard operating procedures. The RAMP assessment allowed us to better understand how we use certain chemical classes and identified areas for improvement. This led to a rich safety culture and helped to ensure a more secure working environment. In addition, the implementation of weekly RAMP presentations has clearly impacted the rate at which accidents happen and are discussed. The amount of accidents in the Patterson lab has decreased, and we have taught new researchers who have joined the lab about the importance of reporting and discussing near misses to prevent more significant accidents.

RAMP: Recognize Hazards

The use of the Schlenk line can pose some serious risks, therefore, mandatory training and a prior knowledge is a must before operating the Schlenk line. The main risks are condensed liquid Oxygen, Explosion,

Implosion from Glassware fatigue or vacuum
Frostbite from liquid Nitrogen
Explosion from liquid oxygen condensation
Explosion due to inert gas over pressurization
Explosion due to heating closed diffusion pump

Explosions:
 Uncontrolled nitrogen pressure
 Chipping bypass tube
 Liquid oxygen condensation

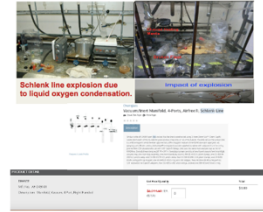
Implosions:
 Stress in glass manifold
 Fine crack in the glass and
 Bumping the glass

CV = 75

• Identify the most important physical hazards from equipment, conditions, and procedures. These include electrical and mechanical hazards and high or low temperature or pressure

RAMP: Assess the Risk

Consequence Value (CV)	Impact to...					
Rating	Value	Personnel Safety	Resources	Work Performance	Property Damage	Reputation
No Risk	1	No injuries	No impact	No delays	Minor	No Impact
Minor	5	Minor injuries	Moderate impact	Modest delays	Moderate	Potential Damage
Moderate	10	Moderate to life impacting injuries	Additional resources required	Significant delays	Substantial	Damaged
High	20	Life threatening injuries from single exposure	Institutional resources required	Major operational disruptions	Severe	Loss of confidence



• Assess the risks presented by the most important hazards.

RAMP: Minimize the Risk

Schlenk Line Turn on Process
Schlenk Line Shut Down Process

Pressurized gases (check over gas pressure carefully)
Condensed gases (check for removal traps in the system)

EXPLOSION
 Heating closed diffusion pump or reaction flask
 Manipulation specific
 Explosions of incoming reagents
 Liquid oxygen reaction pressure and amount exceeding tolerance and high reactivity chemicals

Cracks in glassware - Check for weakness in the glassware, such as a star crack. It can cause it to fail under vacuum. If you notice a crack in a vessel, **Do not use it.**

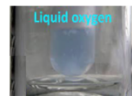
• Identify methods and safe practices to minimize the risks from exposures to chemicals and from physical hazards.
 • Understand the nature and limitations of personal protective equipment, chemical hoods, and other safety equipment

RAMP: Prepare for Emergency

Condensing Oxygen: Liquid oxygen is extremely reactive, and it is the most dangerous hazard associated with Schlenk line operation. Oxygen may react explosively with organic solvents that have been deposited into the trap. The expansion of the gas due to normal heating can build up pressure within the Schlenk line and cause an explosion in that manner.

If you suspect that you have condensed oxygen:

- Replace the Dewars immediately, turn off the vacuum, open the system to the atmosphere close the sash, and allow the system to warm slowly as the N₂ in the Dewars dissipates.
- Close the doors on your hood and warn any other lab personnel present of the explosion hazard.
- Evacuate the lab and notify PI and safety personnel.
- After the traps have come to room temp, consider them still dangerous as peroxides may have formed.
- Rinse the traps with water into a clean beaker and test the solution with the peroxide strips if peroxides are present, neutralize them with sodium thiosulfate or sodium sulfite before disposing of the waste.



• Know and practice the procedures for handling common emergencies such as spills, cuts, burns, exposures, and fire

Figure 6.3 RAMP presentation on Schlenk line safety by Nehal Idris.

Recognize

Get a pet sticker now!

Sender Address
 Attention-Grabbing Hooks
 Urgency
 Spelling and Grammatical Errors
 Unsolicited Messages
 Attachments
 Links
 Login Pages

Minimize

- Spam Filter
- Web Filter
- Malware Protection
- Anti-Phishing Protection

NEVER open attachments from unverified senders
 Write out URL in browser manually

Assess

Consequence Value (CV)	Impact to...					
Rating	Value	Personnel Safety	Resources	Work Performance	Property Damage	Reputation
No Risk	1	No injuries	No impact	No delays	Minor	No impact
Minor	5	Minor injuries	Moderate impact	Modest delays	Moderate	Potential damage
Moderate	10	Moderate to life impacting injuries	Additional resources required	Significant delays	Substantial	Damaged
High	20	Life threatening injuries from single exposure	Institutional resources required	Major operational disruptions	Severe	Loss of confidence

Prepare

Financial Details? Card On or Off Status: Off

Having a problem with this transaction? Dispute transaction

Login Credentials? Change a password

Downloaded Attachment? MALWARE

Figure 6.4 RAMP presentation on nontraditional safety issues of cyber security and fishing by Redford Hudson.



Assess the risks: Power Outage

Consequence Value (CV)		Impact to...				
Rating	Value	Personnel Safety	Resources	Work Performance	Property Damage	Reputation
No Risk	1	No injuries	No impact	No delays	Minor	No impact
Minor	5	Minor injuries	Moderate impact	Modest delays	Moderate	Potential damage
Moderate	10	Moderate to life impacting injuries	Additional resources required	Significant delays	Substantial	Damaged
High	20	Life threatening injuries from single exposure	Institutional resources required	Major operational disruptions	Severe	Loss of confidence

CV = 17

Assess the risks: Leak in Patterson Lab GB

Consequence Value (CV)		Impact to...				
Rating	Value	Personnel Safety	Resources	Work Performance	Property Damage	Reputation
No Risk	1	No injuries	No impact	No delays	Minor	No impact
Minor	5	Minor injuries	Moderate impact	Modest delays	Moderate	Potential damage
Moderate	10	Moderate to life impacting injuries	Additional resources required	Significant delays	Substantial	Damaged
High	20	Life threatening injuries from single exposure	Institutional resources required	Major operational disruptions	Severe	Loss of confidence

CV = 26

Assess the risks: Gas, Electrical or Mechanical Failure

Consequence Value (CV)		Impact to...				
Rating	Value	Personnel Safety	Resources	Work Performance	Property Damage	Reputation
No Risk	1	No injuries	No impact	No delays	Minor	No impact
Minor	5	Minor injuries	Moderate impact	Modest delays	Moderate	Potential damage
Moderate	10	Moderate to life impacting injuries	Additional resources required	Significant delays	Substantial	Damaged
High	20	Life threatening injuries from single exposure	Institutional resources required	Major operational disruptions	Severe	Loss of confidence

CV = 70-90

Figure 6.5 RAMP presentation on glove box safety with 3 different CV calculations based on possible hazards by Paul Hurst.

6.3 Mental Health and Lab Safety

In recent years, there has been an increase in the emphasis on safety culture within chemistry laboratories. As a result, mental health has become a more prominent topic in understanding root causes of lab accidents. This shift in focus was prompted by data indicating that graduate students experience growing levels of distress, identifying that 24% of Ph.D. students exhibit signs of sadness, and 17% display symptoms of anxiety.^{12,13} These rates are significantly higher than those observed in the general population but are similar to those in medical students and resident physicians.¹² However, with the onset of the COVID-19 pandemic, these numbers have skyrocketed, indicating a change in general laboratory culture. In a 2020

survey, it was found that anxiety symptoms in graduate students rose 50% compared to those seen in 2019.^{13,14}

It is important to note that graduate students struggling with mental health issues can experience a range of negative consequences, including physical health concerns, strained personal relationships¹⁶, and decreased academic performance.^{11,12} It has been found that the most common aspects of graduate school that can affect anxiety, stress, and depression amongst graduate students are the amount of structure in a research or teaching program, positive and negative reinforcement, success and failure in research progress, and social support and isolation.¹⁷

Mental health issues in the lab should be treated similarly to physical health concerns. Just as we conduct risk assessments and implement various controls to minimize physical hazards, we should also identify and assess mental health risks to create a comprehensive safety culture. One practical approach to tackle mental health issues in the lab is to apply a RAMP assessment to common mental health concerns like stress, burnout, and anxiety. This framework facilitates open conversations and proactive strategies to support mental well-being in the lab environment.

For example, Elisa Olivas' RAMP analysis on the impact of emotional intelligence on lab safety highlights the significance of self-awareness, empathy, and effective communication in preventing accidents and promoting a positive lab culture (Figure 6.6). By recognizing the mental health hazards associated with research activities, assessing their risk, minimizing their effects through stress management and support, and preparing for potential mental health emergencies, we can create a safer and more supportive environment for all lab members.

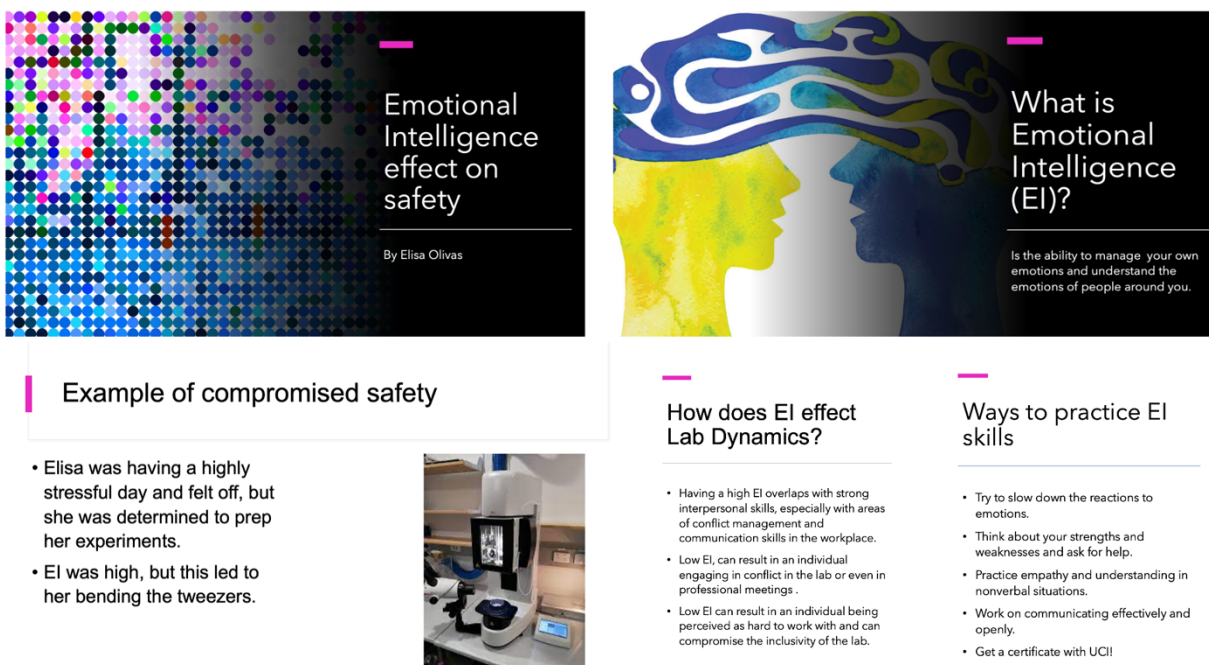


Figure 6.6 RAMP presentation on glove box safety with 3 different CV calculations based on possible hazards by Elisa Olivas.

To address mental health concerns in the larger community of the UCI Chemistry Department, the Graduate Safety Team (GST) has taken a proactive approach by launching several initiatives to create safe spaces for students to openly discuss their mental health concerns. One notable example is the Stress Management and Self-Care workshop (Figure 6.7), designed to provide students with practical tools and resources to manage stress and prioritize their well-being. In collaboration with the UCI campus's Student Wellness and Health Promotion Programs, this workshop leveraged free resources to educate students on effective stress management techniques, mindfulness practices, and self-care strategies.

Through interactive sessions and group discussions, participants learned how to recognize the signs of stress and anxiety, develop healthy coping mechanisms, and build resilience in the face of academic and personal challenges. The workshop also provided a safe

and supportive environment for students to share their experiences, connect with peers, and feel empowered to seek help when needed. By promoting a culture of openness and support, the GST aims to break down the stigma surrounding mental health in the Chemistry Department and foster a community prioritizing student well-being and success.

In addition to organizing workshops to create spaces for open dialogue around mental health issues, we aimed to ensure that all graduate and undergraduate students were aware of the resources provided to them through UCI and how to easily access them. We made these resources accessible through a mental health stall wall poster meant to be hung on bathroom stall walls to reach the widest audience (Figure 6.8). This stall wall poster highlighted resources such as free on campus therapy and how to facilitate long term care. It included a script that students could use if unsure how to open the conversation about seeking mental health resources. This stall wall increased awareness amongst graduate students of the available resources and directed them toward emergency care if necessary.

As students in the early stages of our careers, we must prioritize our mental well-being and create a supportive environment to discuss our concerns openly. For too long, mental health has been stigmatized in higher education, with a looming "grin and bear it" attitude that can lead to burnout. There is a growing recognition amongst academics that this culture needs to change, and we are shifting toward a more sustainable and inclusive approach where students and faculty alike can prioritize their mental health without fear of judgment or repercussions. By providing resources and safe spaces for open discussions, we can break down the stigma surrounding mental health in higher education. This can include access to counseling services and mental health professionals, community building, and workshops and training focusing on mindfulness,

self-care, and boundary setting. We can create a healthier and more productive academic environment by fostering a culture of openness and support.

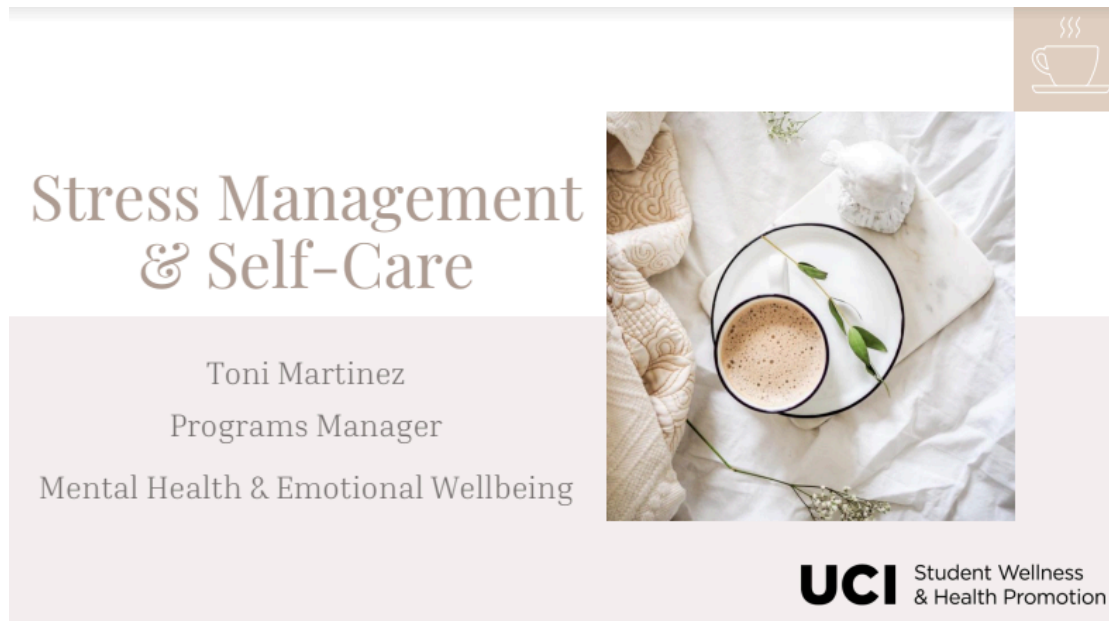


Figure 6.7 Poster advertising Stress Management and Self-Care sponsored by the UCI GST.

Long-term therapy with UC-SHIP

Mental health struggles amongst graduate students around the world occur at alarming rates. One study in 2017 found that 1/3 of PhD students are at risk of developing a mental health disorder while another 2020 of 13,000 junior researchers study found that 38% of respondents felt overwhelmed by their work situation. If you're struggling with mental health, you are not alone, and therapy can be one of many support strategies to navigate the challenges of graduate school.



Questions? Email safety@uci.edu or graduatesafetyteam@uci.edu

Do you have a hard copy of your SHIP card?

- Note: SHIP insurance is Anthem blue cross PPO
- From your mobile device: App store and download the "StudentHealth" app. Register and view your electronic insurance card

Find Therapy

- Option 1: Obtain list of referrals from Counseling Center Clinical Case Managers
- Option 2: visit uci.welltrackconnect-connect.com
- Option 3: Download ZocDoc and enter your information

Reach out to therapist

- Here's what to say: Hi, my name is _____. I would like to start therapy with you to work on _____. I am a student from UCI and have Anthem Blue Cross PPO insurance (your SHIP insurance). I am available _____ (Days/Times of day). My phone number is _____ [repeat number twice] and I will be awaiting your call back within the week

Confirm these things with your Therapist before your fist appointment

- A: They still accept Anthem Blue Cross PPO IN-NETWORK (If they speak of a 'superbill' or being 'out-of-network' this will cost a lot more money
- B: if they are providing teletherapy and/or in person services
- C: Their specialties and if they are a match for your needs
- D: their schedule and availability
- You can schedule with them directly or call back if you need more time to decide
- When you schedule the appointment obtain their address – including fax number if they have one

Getting a referral

- Contact student health center at 949-824-2388 one week prior to your appointment, copay with SHIP is \$10 per session

For urgent matters please call the counseling center at (949)824-6457, if it's after hours or on weekends press option 2 to reach the after-hours crisis line. For emergencies, call 911 or the UCI police at (949)824-5223

Figure 6.7 Stall wall poster detailing the information needed to access mental health resources for graduate and undergraduate researchers by UCI GST.

6.4 Conclusions

Prioritizing laboratory safety and mental health awareness is crucial for creating a safe and productive research environment in graduate chemical labs. We can foster a culture of safety awareness and accountability by recognizing the importance of proactive risk management and open discussions. Through initiatives such as risk assessments, training sessions, and mental health support, we can equip researchers with the knowledge and skills necessary to identify and minimize potential hazards. By acknowledging the emotional and psychological toll of graduate research, we can promote a supportive and inclusive research culture that prioritizes the well-being of all researchers. Securing lab safety and mental health awareness is a shared responsibility that requires the collective effort of researchers, educators, and institutions. By working together, we can create a safer and more productive research environment that allows researchers to thrive and make meaningful contributions to their fields. As we continue to push the boundaries of scientific discovery, it is important to prioritize the safety and well-being of those who make it possible.

6.5 References

- (1) Nasrallah, I. M.; El Kak, A. K.; Ismail, L. A.; Nasr, R. R.; Bawab, W. T. Prevalence of Accident Occurrence Among Scientific Laboratory Workers of the Public University in Lebanon and the Impact of Safety Measures. *Saf. Health Work* **2022**, *13* (2), 155–162. <https://doi.org/10.1016/j.shaw.2022.02.001>.
- (2) Palluzi, R. The Ten Most Common Laboratory Safety Issues. *ACS Chem. Health Saf.* **2022**, *29* (1), 19–26. <https://doi.org/10.1021/acs.chas.1c00063>.
- (3) Gibson, J. H.; Schröder, I.; Wayne, N. L. A Research University's Rapid Response to a Fatal Chemistry Accident: Safety Changes and Outcomes. *J. Chem. Health Saf.* **2014**, *21* (4), 18–26. <https://doi.org/10.1016/j.jchas.2014.01.003>.

- (4) Tanner, C. A student burned his eye in a University of Utah lab. The U. knew about dangers beforehand, an audit finds, but didn't take action. *The Salt Lake Tribune* **2019**. <https://www.sltrib.com/news/education/2019/05/14/student-burned-his-eye>
- (5) Ménard, A. D.; Trant, J. F. A Review and Critique of Academic Lab Safety Research. *Nat. Chem.* **2020**, *12* (1), 17–25. <https://doi.org/10.1038/s41557-019-0375-x>.
- (6) Basbug, G.; Cavicchi, A.; Silbey, S. S. Rank Has Its Privileges: Explaining Why Laboratory Safety Is a Persistent Challenge. *J. Bus. Ethics* **2023**, *184* (3), 571–587. <https://doi.org/10.1007/s10551-022-05169-z>.
- (7) Brendrly, B. The Burning Question of Laboratory Safety. *Science* **2009**. <https://www.science.org/content/article/burning-question-laboratory-safety>
- (8) Council, N. R.; Education, D. of B. and S. S. and; Integration, B. on H.-S.; Studies, D. on E. and L.; Technology, B. on C. S. and; Research, C. on E. and P. a C. of S. in A. L. Safe Science: Promoting a Culture of Safety in Academic Chemical Research, *National Academies Press*, 2014.
- (9) Stuart, R. B.; McEwen, L. R. The Safety “Use Case”: Co-Developing Chemical Information Management and Laboratory Safety Skills. *J. Chem. Educ.* **2016**, *93* (3), 516–526. <https://doi.org/10.1021/acs.jchemed.5b00511>.
- (10) *GHS (Rev.8) (2019) | UNECE*. <https://unece.org/ghs-rev8-2019>
- (11) Hierarchy of Controls. NIOSH. CDC. <https://www.cdc.gov/niosh/topics/hierarchy/default.html>
- (12) Evans, T. M.; Bira, L.; Gastelum, J. B.; Weiss, L. T.; Vanderford, N. L. Evidence for a Mental Health Crisis in Graduate Education. *Nat. Biotechnol.* **2018**, *36* (3), 282–284. <https://doi.org/10.1038/nbt.4089>.
- (13) Duffy, M. A.; Tronson, N. C.; Eisenberg, D. Supporting Mental Health and Productivity within Labs. *Neuron* **2021**, *109* (20), 3206–3210. <https://doi.org/10.1016/j.neuron.2021.08.021>.
- (14) Zarowski, B.; Giokaris, D.; Green, O.; Zarowski, B.; Giokaris, D.; Green, O. Effects of the COVID-19 Pandemic on University Students' Mental Health: A Literature Review. *Cureus* **2024**, *16* (2). <https://doi.org/10.7759/cureus.54032>.
- (15) Rummell, C. M. An Exploratory Study of Psychology Graduate Student Workload, Health, and Program Satisfaction. *Prof. Psychol. Res. Pract.* **2015**, *46* (6), 391–399. <https://doi.org/10.1037/pro0000056>.
- (16) Salzer, M. S. A Comparative Study of Campus Experiences of College Students With Mental Illnesses Versus a General College Sample. *J. Am. Coll. Health* **2012**, *60* (1), 1–7. <https://doi.org/10.1080/07448481.2011.552537>.
- (17) Gin, L. E.; Wiesenthal, N. J.; Ferreira, I.; Cooper, K. M. PhDepression: Examining How Graduate Research and Teaching Affect Depression in Life Sciences PhD Students. *CBE Life Sci. Educ.* **2021**, *20* (3), ar41. <https://doi.org/10.1187/cbe.21-03-0077>.
- (18) Hysenbegasi, A.; Hass, S. L.; Rowland, C. R. The Impact of Depression on the Academic Productivity of University Students. *J Ment Health Policy Econ* **2005**.
- (19) Harvey, S. B.; Glozier, N.; Henderson, M.; Allaway, S.; Litchfield, P.; Holland-Elliott, K.; Hotopf, M. Depression and Work Performance: An Ecological Study Using Web-Based Screening. *Occup. Med.* **2011**, *61* (3), 209–211. <https://doi.org/10.1093/occmed/kqr020>.

Chapter 7:

Conclusion

Chapter 7. Conclusion

7.1 Outlook and Future Directions

This thesis presents compelling progress in MOF crystallization, providing new mechanistic insights into how to observe and understand MOF nucleation and growth. By combining fundamental chemistry theories with combined bulk and local analytical techniques, this research has advanced our understanding of the prenucleation phases of MOF formation and how we can alter and observe these changes.

Chapter 1 introduces the theories and methods in which we can understand MOF nucleation and growth. Through an understanding of these analytical techniques and the phase regimes in which they are most useful, we can combine these concepts to gain a larger picture of MOF nucleation and growth. This chapter discusses polymorph formation in MOFs and how it is important to understand how to control polymorph formation to direct the growth of new MOFs without the need for high-throughput synthesis.

Chapter 2 discusses the polymorph formation of ZIF-8 and provides analytical insight into the nucleation and growth mechanisms. The main topic addressed is a molecular understanding of the PNC's and their role in the final polymorph formation. To study the early stages of nucleation and growth, a combination of advanced microscopy, scattering and spectroscopy methods were used with a large emphasis on WAXS and ESI-MS. These techniques allowed for a larger understanding of the prenucleation cluster influence on polymorph control in ZIF-8. This revealed that SOD nucleates rapidly via the formation and aggregation of amorphous particles which contain a significant amount of 3Zn clusters whereas

dia nucleates more slowly via the formation of stable amorphous particles which are composed of 2Zn clusters.

Chapter 3 details the importance of reaction volume and vessel size on the nucleation and growth rate and mechanism of ZIF-8. This work demonstrated with an increase in confinement, the crystallization of ZIF-8 slows, and the degree of crystallinity decreases as well. We were able to demonstrate this with a comparison between 15 mm vial solution and the reaction in 1 mm and 2 mm capillaries, which are typically used to measure reaction kinetics in WAXS measurements. This work is important to consider when designing experimental procedures where the kinetics of nucleation and growth are measured with techniques that require different synthesis volumes such as in-situ WAXS, SAXS and spectroscopy methods.

Chapter 4 This work showcases the ability to modify BSA with the addition of CD to affect the encapsulation of BSA in ZIF-8 frameworks. Through a study of the zeta potential, it is clear that the zeta potential is lowered, which would allow for lower encapsulation rates of CD:BSA complexes in comparison to BSA alone. CD:BSA complexes did not have a large effect on the overall polymorph formation of ZIF-8, producing only SOD polymorphs independent of HmIm:Zn ratio or CD:BSA ratio. This work shows that we can modify biomolecules and direct the encapsulation based on charge with only supramolecular modification.

Chapter 5 demonstrates the synthesis of cyclodextrin metal–organic framework-based protein biocomposites with the use of different cyclodextrin frameworks. Modification in the CD alters the release profile of encapsulated proteins. Using other types of cyclodextrins, we have shown that the release profile can be tuned and the encapsulated proteins remain active after release from these materials. Encapsulation of catalase and interleukin-2 in γ -CD-MOF decreases their biological activity, while encapsulation in β -CD-MOF preserves it. We hypothesize that,

during the synthesis of γ -CD-MOFs, methanol interferes and weakens hydrophobic interactions of the tertiary protein structures. Future p@CD-MOFs synthesis will focus on non-protic solvents as non-solvents for crystallization. These results demonstrate the importance of developing a bio-friendly method for encapsulating biomolecules within MOFs. Considering that during release, the proteins will be in a cyclodextrin-rich environment, we believe these materials are promising for the delivery of therapeutic proteins.

Chapter 6 highlights the importance of lab safety training and awareness. In this chapter, risk assessment using the RAMP assessment is discussed, detailing the ways in which the typical RAMP analysis of common safety hazards can be expanded to non-traditional topics and encourage open communication about safety concerns. In addition to physical safety concerns, I also discuss the role of mental health awareness on lab safety and how creating an open environment, free from mental health stigma, can encourage researcher well-being and productivity.

In the exciting future of MOF crystallization and development, this dissertation emphasizes the importance of relying heavily on nucleation and growth fundamentals to explore the fundamental design space and engineer new and exciting MOFs without the need for high throughput screening.